C/ORNL94-0319

CRADA Final Report
for
CRADA Number ORNL 94-0319

DESIGN AND PRODUCT OPTIMIZATION FOR CAST LIGHT METALS

S. Viswanathan, A. S. Sabau, Q. Han,
A. J. Duncan, W. D. Porter,
and R. B. Dinwiddie

Oak Ridge National Laboratory
Oak Ridge, Tennessee 37831

D. E. Penrod
U.S. Automotive Materials Partnership (USAMP)

Date Published: March 2001

Prepared by the
Oak Ridge National Laboratory
Oak Ridge, Tennessee 37831
managed by
UT-Battelle, LLC
for the
U.S. Department of Energy
under contract DE-AC05-00OR22725

APPROVED FOR PUBLIC RELEASE

UNLIMITED DISTRIBUTION

C/ORNL94-0319

CRADA Final Report
for
CRADA Number ORNL 94-0319

DESIGN AND PRODUCT OPTIMIZATION FOR CAST LIGHT METALS

S. Viswanathan, A. S. Sabau, Q. Han,
A. J. Duncan, W. D. Porter, and R. B. Dinwiddie

Oak Ridge National Laboratory
Oak Ridge, Tennessee 37831

D. E. Penrod
U.S. Automotive Materials Partnership (USAMP)

Date Published: March 2001

Prepared by
OAK RIDGE NATIONAL LABORATORY

managed by
UT-Battelle, LLC
for the
U.S. Department of Energy
under contract DE-AC05-00OR22725

CONTENTS

ABSTRACT 1

1.0 OBJECTIVE 2

2.0 ASSESSMENT OF CRADA RESULTS 2

3.0 BENEFITS TO DOE 2

4.0 TECHNICAL BACKGROUND 3

4.1 EXECUTIVE SUMMARY 3

4.2 MODELING OF A356 ALLOY CASTINGS . . . 3

4.3 MEASUREMENT OF LIQUID PERMEABILITY IN THE MUSHY ZONE 25

4.4 MODELING OF MICROPOROSITY IN A356 ALLOY CASTINGS . 37

4.5 MODELING OF MICROSTRUCTURE IN A356 ALLOY CASTINGS 58

4.6 MODELING OF LOWER CONTROL ARM CASTING . . 75

4.7 REFERENCES 82

5.0 REPORT OF INVENTIONS 88

6.0 COMMERCIALIZATION POSSIBILITIES 88

7.0 PLANS FOR FUTURE COLLABORATION 88

8.0 CONCLUSIONS 88

ACKNOWLEDGMENTS 88

DISTRIBUTION 91

ABSTRACT

The main phases that are present in A356 aluminum alloy castings are the primary aluminum and eutectic silicon phases. It is the morphology of these phases, together with the microporosity, that determines the mechanical properties, notably the fatigue life of structural aluminum alloy castings. As part of a program to develop optimized tooling for the design of the casting process for structural A356 aluminum alloy components, models have been developed and used for predicting phase fractions, microstructural length scales, and fraction microporosity. Thermophysical properties needed for the numerical simulation of fluid flow, heat transfer, solidification, and solidification shrinkage have been measured. The permeability of interdendritic liquid in the mushy zone has been evaluated experimentally.

This report documents all aspects of the development of the models for the prediction of microstructural length scales and fraction microporosity. The length scales are the primary dendrite size, secondary dendrite arm spacing and cell spacing for the primary aluminum phase, and the particle/rod length, diameter and spacing for the silicon phase. The microstructure models predict phase evolution during solidification and the final length scales after solidification, and consider the mechanisms governing the growth of the primary aluminum and silicon phases. A comprehensive methodology taking into account solidification, shrinkage-driven interdendritic fluid flow, hydrogen precipitation, and porosity evolution has been developed for the prediction of microporosity fraction. The predictions are validated by comparison with independent experimental measurements by other researchers and with data from the literature. The models are implemented in a computational framework consistent with those of commercial casting codes, allowing them to be easily incorporated in commercial casting simulation software.

1.0 Objective

The objective of this project is the development of numerical models for the prediction of microporosity and microstructural length scales for aluminum A356 alloy castings. The models will be general and apply to a variety of casting processes such as sand casting, gravity, low pressure, and tilt pour permanent mold casting, and squeeze casting. First, all existing commercial casting software tools will be identified and reviewed. In particular, the application of each commercial code for the modeling of mold filling, solidification, and porosity prediction in A356 alloy castings will be evaluated. New developments will be carried out to fill any gaps identified in current casting simulation software. Also, all thermophysical property measurements of A356 alloy needed for casting simulation will be measured or estimated.

2.0 Assessment of CRADA Results

All the objectives in the Statement of Work for this CRADA were substantially met. In particular, new and accurate numerical methodologies were developed for the modeling of shrinkage driven fluid flow during casting solidification, and the prediction of both hydrogen and shrinkage porosity. Approaches were also developed to predict microstructural length scales for aluminum A356 alloy. The models were implemented in the commercial casting code ProCAST and are currently available to industry users for the routine computer-aided-design and analysis of the casting process.

3.0 Benefits to DOE

This CRADA has enhanced the capabilities and skills at the Oak Ridge National Laboratory (ORNL) in the areas of casting process design, process modeling, and the development of numerical codes of heat transfer, fluid flow, and phase change. This will improve the prospects of future projects dealing with process modeling in general and casting and solidification processing in particular. The experience gained in this project could be applied to the development of near-net shape dies for the processing of advanced materials. It has also demonstrated that DOE programs can allow industry to access the technology available at DOE laboratories.

4. Technical Background

4.1 Executive Summary

The main phases that are present in aluminum A356 alloy castings are the primary aluminum and eutectic silicon phases. It is the morphology of these phases, together with the microporosity, that determines the mechanical properties, notably the fatigue life of structural aluminum alloy castings. As part of a program to develop optimized tooling for the design of the casting process for structural aluminum A356 alloy components, models have been developed and used for predicting phase fractions, microstructural length scales, and fraction microporosity. Thermophysical properties needed for the numerical simulation of fluid flow, heat transfer, solidification, and solidification shrinkage have been measured. The permeability of interdendritic liquid in the mushy zone has been evaluated experimentally.

The computer-aided-design and analysis of a robust casting process requires the optimization of both mold filling and solidification. Figure 4.1.1 illustrates the systematic approach that should be used.

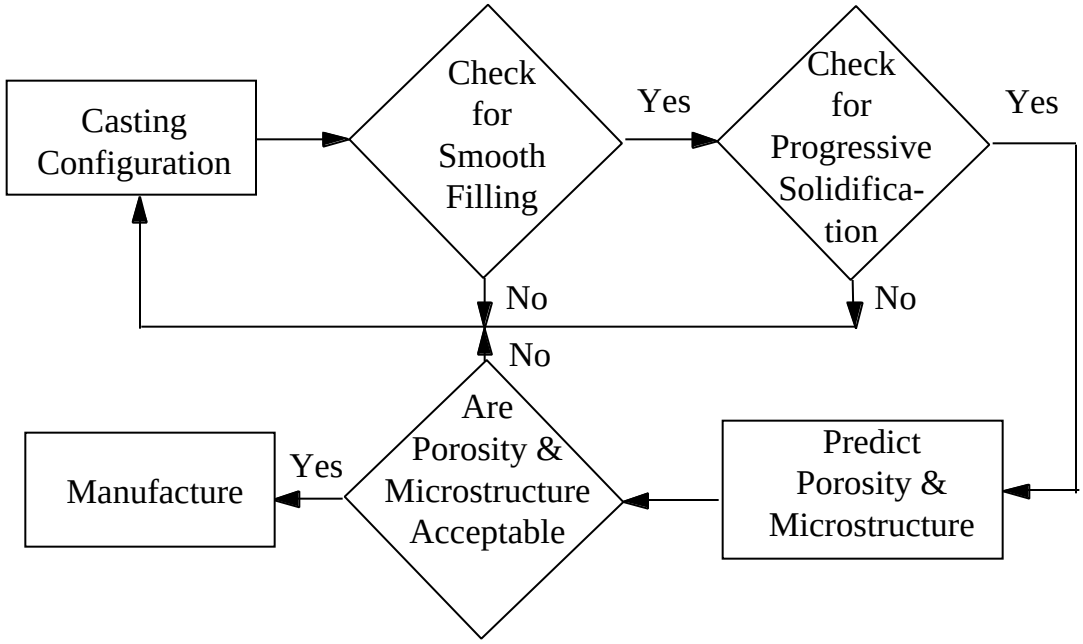

Fig. 4.1.1. Flow chart for the computer-aided-design and analysis of a casting process illustrating the steps leading to a robust casting process design.

In particular, codes that are suitable for use in the design and analyses of casting processes for structural safety-critical castings must allow the quantitative prediction of defects and microstructure. Microstructural features of interest for the prediction of casting performance and properties includes pore size, pore density, and pore distribution, and details of microstructure such as grain size and second phase particle size and distribution. In the case of aluminum alloys, this includes features such as silicon particles and intermetallics. Figure 4.1.2 provides a comparison of features of commercial codes at the start of this program and the scope of

development targeted in this program for applicability to the casting process design for structural safety-critical castings.

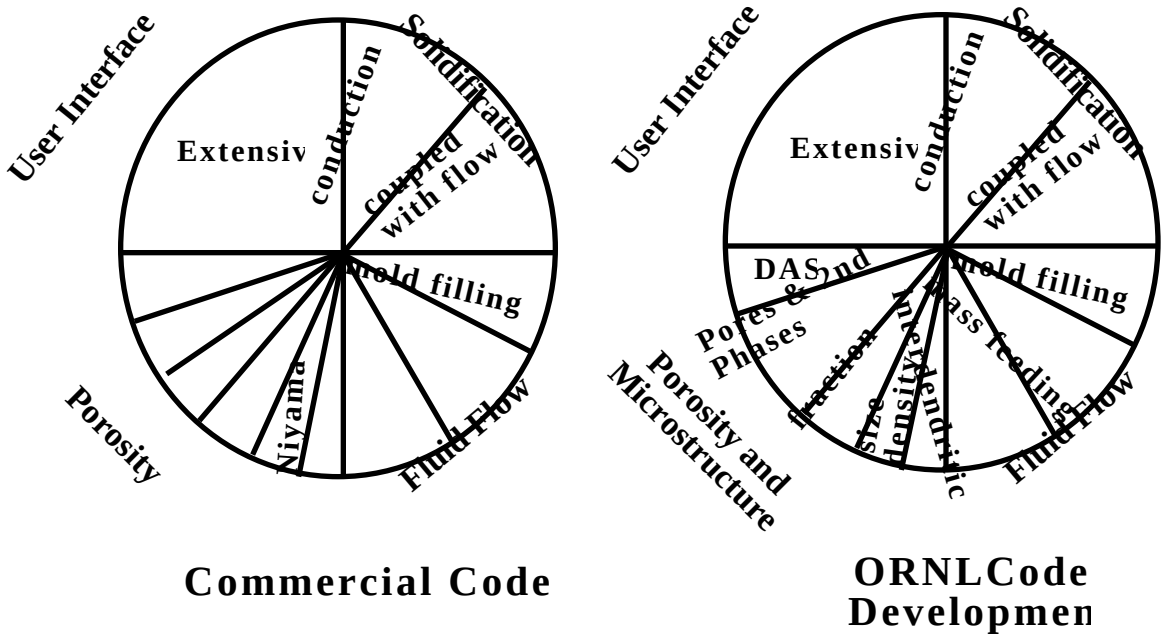

Fig. 4.1.2. Comparisons of features of commercial codes at the start of the program and the scope of development for applicability to the casting process design for structural and safety critical castings.

The following sections of this report document all aspects of the development of the models for the prediction of microstructural length scales and fraction microporosity. In the last section, the implementation of the microporosity and microstructure models in the commercial casting code ProCAST is discussed. Results are presented for the automotive lower control arm casting in Fig. 4.1.3.

The report is divided into the following six sections:

5. Executive Summary
6. Modeling of A356 Alloy Castings
7. Measurement of Liquid Permeability in the Mushy Zone
8. Modeling of Microporosity in A356 Alloy Castings
9. Modeling of Microstructure in A356 Alloy Castings
10. Modeling of Lower Control Arm Casting

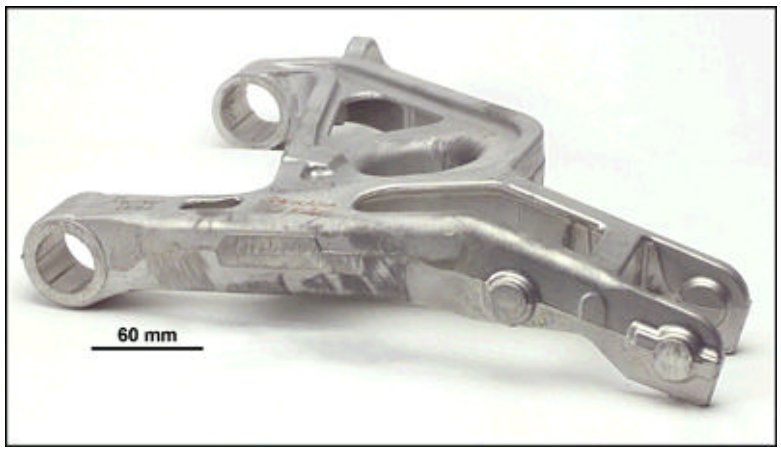

Fig. 4.1.3. Automotive lower control arm casting used for modeling demonstrations.

The various sections provide detailed information on the modeling and development of microporosity and microstructure models as follows:

4.1.1 Modeling of A356 Alloy Castings

This section addresses some of the issues involved in the use of commercial casting simulation packages for the design and analyses of casting processes for structural aluminum alloy castings for chassis components. In addition, it outlines some of the issues involved in the development and use of computer models of the casting process. The importance of the availability of accurate thermophysical properties is illustrated by comparing the sensitivity of the computed cooling curves to changes in thermophysical properties. The analysis indicates that if constant thermophysical properties must be used in solidification simulation, the values at the solidus temperature are likely to provide the greatest accuracy; in particular, the analysis indicates that significant errors may be incurred by the use of constant room temperature properties. Finally, the report compares key features in three popular commercial casting simulation codes and identifies the opportunities for development followed in this program.

4.1.2 Measurement of Liquid Permeability in the Mushy Zone

Measurements of liquid permeability in the mushy zones of Al-15.42% Cu and Al-8.68% Cu alloy samples were performed isothermally just above the eutectic temperature, using eutectic liquid as the fluid. A modified method was developed to determine the specific permeability, K_S, as a function of time during the test from the data collected on these alloys. Factors affecting permeability measurements are discussed. Permeabilties are observed to vary throughout the experiment. This is attributed to microstructural coarsening and channeling that occur in the sample during the experiment. Coarsening rates are determined for isothermal coarsening tests without fluid flow, and the results are observed to be less than rates indicated from permeability tests where fluid flow is present. Careful measurement of volume fraction liquid, g_L, shows that g_L decreases during the test. The permeability is then related to the microstructure of the sample using the Kozeny-Carman equation. The correlation between the measured K_S, g_L, and the

specific solid surface area, S_V, improves markedly when compared to previous studies when microstructural parameters at the initial stage of the test are used.

4.1.3 Modeling of Microporosity in A356 Alloy Castings

A comprehensive methodology taking into account solidification, shrinkage-driven interdendritic fluid flow, hydrogen precipitation, and porosity evolution has been developed for the prediction of microporosity fraction. The model has been implemented in a computational framework consistent with those of commercial casting codes, allowing them to be easily incorporated in the commercial software. The porosity model has been used to calculate the pressure drop associated with the resistance to interdendritic flow to feed shrinkage, hydrogen redistribution, and pore nucleation and growth. Porosity formation and growth due to both hydrogen precipitation and shrinkage is considered. The models have been validated on test castings designed to capture a variety of porosity formation conditions and porosity distributions. In particular, the models accurately capture feeding conditions that lead to hydrogen or shrinkage porosity (Fig. 4.1.4).

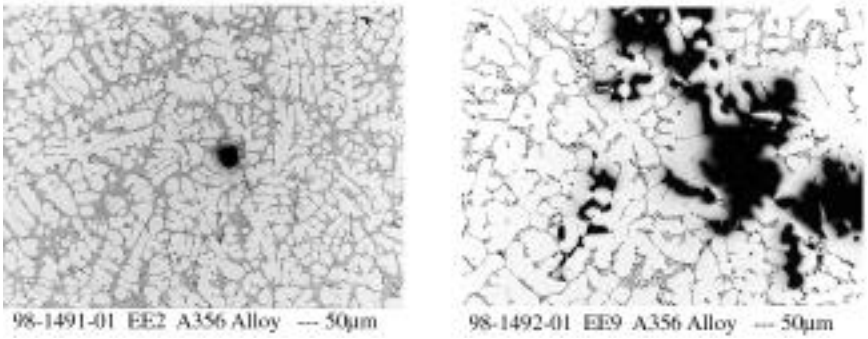

(*a*) (*b*)

Fig. 4.1.4. Pore morphologies along the centerline of the chill plate casting denoting *(a)* hydrogen porosity and *(b*) shrinkage porosity.

This section provides an overview of the physics involved in porosity formation, hydrogen and shrinkage porosity. Constitutive model developments are also presented for the numerical simulation of fluid flow, heat transfer, and solidification during casting. Finally, the solution algorithms and details of the implementation methodology are provided. Information is also provided on permeability data and thermophysical properties needed for the numerical simulation of A356 aluminum alloy castings.

4.1.4 Modeling of Microstructure in A356 Alloy Castings

The main phases that are present in aluminum A356 alloy castings are the primary aluminum and eutectic silicon phases. It is the morphology of these phases, together with the microporosity, that determines the mechanical properties, notably the fatigue life of structural alloy castings. This section describes the development of models for the prediction of microstructural length scales for these two phases (Fig. 4.1.5). These length scales are the primary dendrite size, secondary dendrite arm spacing and cell spacing for the primary aluminum phase and the

particle/rod length, diameter and spacing for the silicon phase. The models predict phase evolution during solidification and the final length scales after solidification. Mechanisms governing the growth of these phases are considered in the models. The predictions are compared with independent measurements by other researchers and with data from the literature. The results of the models are presented in the form of analytical equations for each of the length scales. The simple form of the equations allow them to be used in the post processing step of commercial solidification codes for the prediction of microstructure in shape castings. The models developed in this program and documented in this report represent a convenient and viable approach for determining microstructural length scales for A356 aluminum alloy castings needed in mechanical property and component life prediction models.

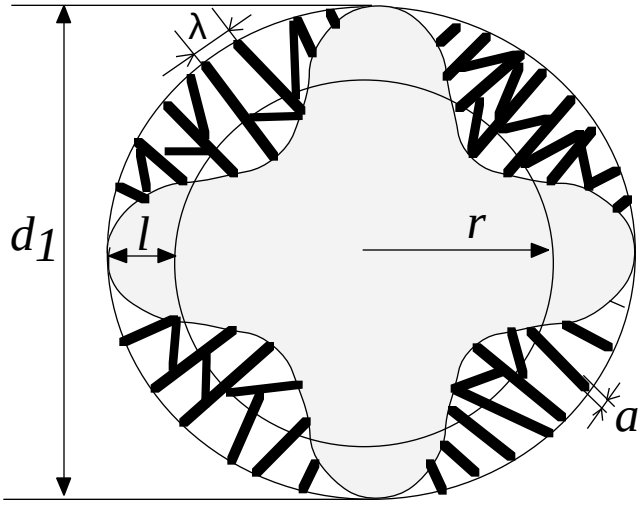

Fig. 4.1.5. Schematic diagram showing the various phase constituents (primary aluminum and eutectic phase) in aluminum A356 alloy and the geometric relationship between the various constituents.

4.1.5 Modeling of Lower Control Arm Casting

The microporosity and microstructure models developed in this program and implemented in the commercial casting code ProCAST have been used to model an automotive lower control arm casting. Two different configurations of the lower control arm casting have been modeled, viz., the production component, and a modified version that is approximately 25% lighter. The modeling of the two configurations included mold filling, solidification, microporosity distribution, and microstructural length scale distributions. Figure 4.1.6 illustrates the microporosity distribution in the production control arm as calculated in ProCAST.

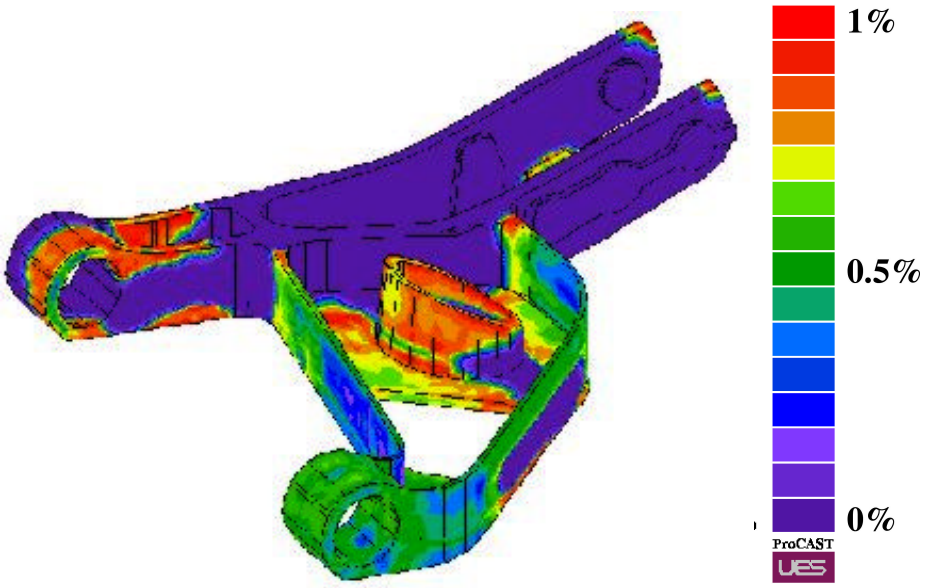

Fig. 4.1.6. Microporosity distribution in the modified control arm casting 75 seconds from the start of casting, calculated using the ProCAST implementation of the microporosity model.

4.2 MODELING OF A356 ALLOY CASTINGS

The development and availability of computer models for casting simulation in the last decade, coupled with the increasing power of workstations, has made it possible to incorporate computer modeling into the routine design of the casting process. However, even as the ease of use of the software as well as its applicability has steadily increased, the range of applicability of commercial software as well as guidelines for their use are less well known.

This report addresses some of the issues involved in the use of commercial casting simulation packages for the design and analyses of casting processes for structural aluminum alloy castings for chassis components. In addition, it outlines some of the issues involved in the development and use of computer models of the casting process. The importance of the availability of accurate thermophysical properties is illustrated by comparing the sensitivity of the computed cooling curves to changes in thermophysical properties. The analysis indicates that if constant thermophysical properties must be used in solidification simulation, the values at the solidus temperature are likely to provide the greatest accuracy; in particular, the analysis indicates that significant errors may be incurred by the use of constant room temperature properties. Finally, the report compares key features in three popular commercial casting simulation codes and identifies the opportunities for development followed in this program.

4.2.1 Casting Process Design and Analysis

The computer-aided-design and analysis of a robust casting process requires the optimization of both mold filling and solidification. Figure 4.2.1 illustrates the systematic approach that should be used. A number of commercial casting codes such as EKK-CAP/WRAFTS™, Flow-3D™, Magma™, Powercast™, and ProCAST™ are available that allow the modeling of mold filling and solidification during casting.

The validity of the results from a commercial code will depend on the accuracy of the code as well as the quality of input parameters (initial and boundary conditions) and thermophysical properties. If only qualitative results are required, constant or room temperature properties may be acceptable. However, when quantitative results are needed, temperature dependent properties may have to be used. Since commercial codes often vary in the range of input thermophysical properties they accept, it would be useful to carry out a study of the sensitivity of simulation results to the thermophysical properties used.

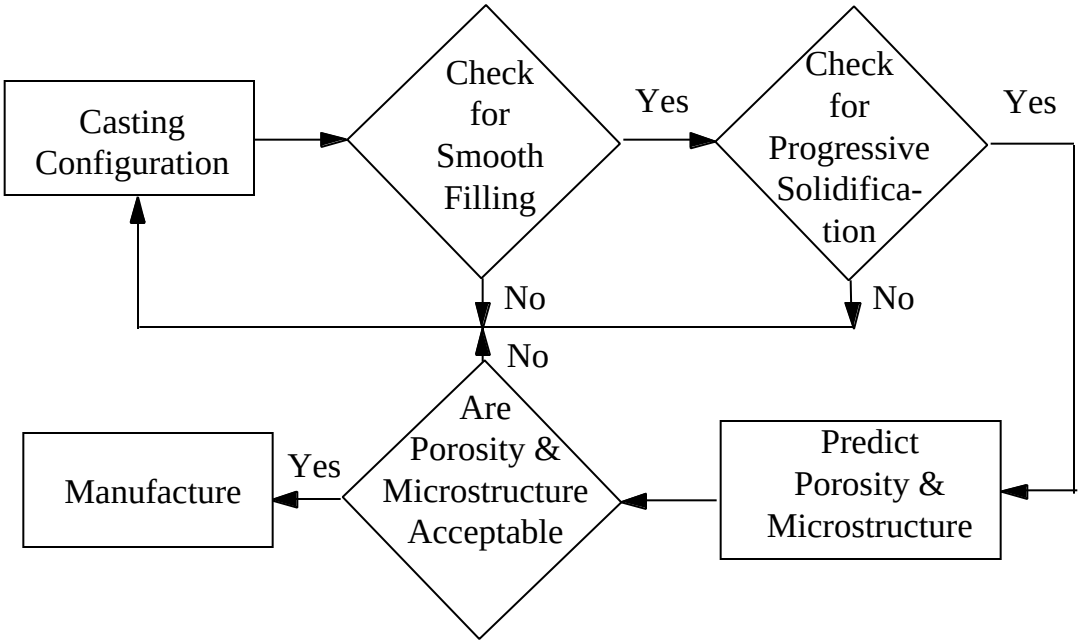

Fig. 4.2.1. Flow chart for the computer-aided-design and analysis of a casting process illustrating the steps leading to a robust casting process design.

4.2.2 Thermophysical Properties For Casting Simulation

Once a suitable casting code has been identified or developed, there is still the matter of obtaining the required thermophysical properties for the particular alloy. Often, properties available in the literature are not available as a function of temperature or at the temperature of interest; in this case, between the solidus and liquidus temperatures and in the liquid. Further, information such as the fractional evolution of latent heat as a function of temperature in the mushy zone, necessary for the modeling of solidification, is often unavailable. There is also very limited information on the sensitivity of simulation results to a variation in thermophysical property input data. This is important as it could have implications on the type of property data that need to be determined and input as a function of temperature, both from the point of view of the cost of thermophysical property measurement, and the computer time penalties involved in more detailed calculations. For this study, thermophysical properties were measured over a range of temperatures for aluminum alloy 356, at the facilities of the High Temperature Materials Laboratory (HTML) at the Oak Ridge National Laboratory (ORNL).

4.2.2.1 Thermophysical Property Measurement

For all cases, properties were determined as a function of temperature. Thermal conductivity (K) was determined by its relation to thermal diffusivity (D_T), bulk density (_), and specific heat (C_p), by $D_T = K/\_C_p$ Thermal diffusivity was determined using the laser flash thermal diffusivity

technique. Specific heat capacity was measured using differential scanning calorimetry (DSC). Linear thermal expansion and density were determined by high-temperature dilatometry. A dual push-rod differential dilatometer equipped with a thermally isolated linear variable displacement transducer (LVDT) was used to accurately measure displacement as a function of temperature. For density measurements, the dilatometer was operated in a single push-rod configuration outfitted with a special POCO graphite tube and end caps which contained the alloy sample during melting (see Fig. 4.2.2). The alloy specimen was then heated to 800°C and cooled to below its solidification temperature (500°C). The change in length was measured and multiplied by the cross sectional area of the specimen to determine the volume change during solidification, after compensating for the thermal expansion of the system. The density was calculated over this temperature range from the mass of the specimen. Tables 4.2.1 and 4.2.2 list the measured thermophysical properties for aluminum 356 alloy as a function of temperature.

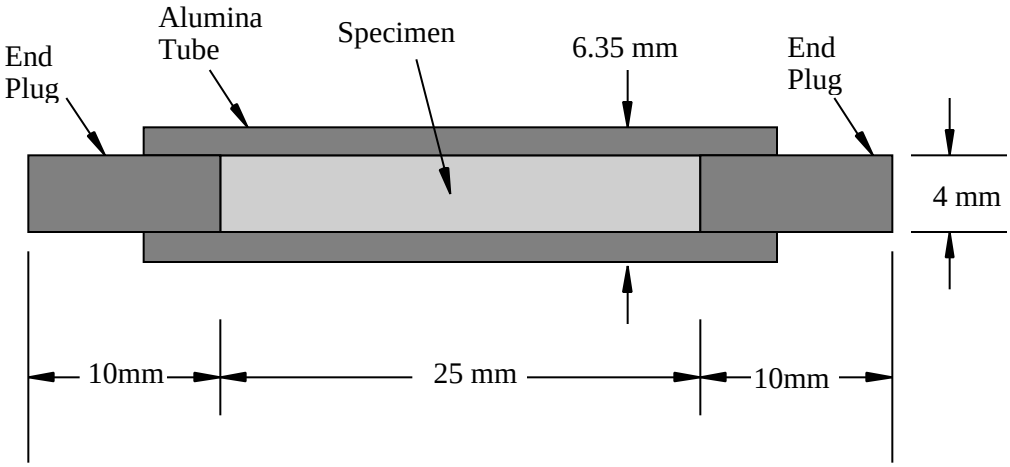

Fig. 4.2.2. Schematic of modified push-rod arrangement used for density measurement by dilatometry.

In order to estimate more accurately the solidification shrinkage for the numerical simulation of porosity, density of liquid and solid phases of A356 alloy was estimated based on measurements performed at ORNL. The evolution of solid volumetric fraction as a function of temperature was calculated using ThermoCalc. Tabular data for the evolution of solid volumetric fraction as a function of temperature, phase densities of A356, and evolution of magnesium and silicon concentrations in the liquid phase of A356 are given in Tables 4.2.3 and 4.2.4. The surface tension is taken to be 640 dynes/cm.

Table 4.2.1. Measured thermophysical properties for aluminum 356 alloy used in modeling.

Temperature (˚C)	Thermal Conductivity (W/m/K)	Density (g/cc)	Specific Heat (KJ/Kg/K)
25		2.67	
100	160.78		0.95718
125	163.08		0.9685
150	165.96		0.97982
175	169.23		0.99114
200	172.70		1.0025
225	176.14		1.0138
250	179.36		1.0251
275	182.18		1.0364
300	184.43		1.0477
325	186.00		1.0591
350	186.81		1.0704
375	186.87		1.0817
400	186.23		1.093
425	185.05		1.1043
450	183.59		1.1157
475	182.22		1.127
500	181.44		1.1383
560		2.56	
615		2.42	
800		2.37	

Latent heat of solidification = 109 cal/g.

Table 4.2.2. Fractional latent heat evolution for A356 aluminum alloy.

Temperature (˚C)	Fraction Latent Heat Evolved
560.0	1.00
564.0	0.84
564.8	0.63
567.0	0.60
583.3	0.50
596.3	0.40
605.6	0.30
612.0	0.20
614.0	0.10
615.0	0.00

Latent heat of solidification = 109 cal/g.

Table 4.2.3. Volumetric solid fraction, liquid phase density, solid phase density, and average phase density for A356 aluminum alloy used for numerical simulation of porosity.

T (^{o}C)	g_s	$\rho_l \left(g/cm^3\right)$	$\rho_s \left(g/cm^3\right)$	$\bar{\rho}_0 \left(g/cm^3\right)$
555.00	1.0	2.453	2.583	2.562
555.00	1.0	2.453	2.583	2.557
555.70	0.96	2.453	2.583	2.557
557.70	0.95	2.453	2.583	2.556
563.70	0.91	2.453	2.583	2.551
566.70	0.87	2.453	2.583	2.546
569.70	0.79	2.453	2.583	2.535
572.10	0.61	2.453	2.583	2.512
574.00	0.52	2.453	2.583	2.500
574.00	0.52	2.453	2.543	2.500
583.70	0.45	2.444	2.543	2.489
589.70	0.40	2.438	2.543	2.480
595.70	0.34	2.433	2.543	2.470
601.70	0.26	2.427	2.543	2.458
607.70	0.17	2.422	2.543	2.442
613.70	0.060	2.416	2.543	2.424
615.00	0.0	2.415	2.543	2.415

Table 4.2.4.Silicon and magnesium concentrations in the liquid phase of aluminum alloy A356 used for numerical simulation of porosity.

T (^{o}C)	C_{Si}^l(%)	C_{Mg}^l(%)
555.14	14.59	5.1
555.85	14.53	4.9
558.85	14.25	4.2
561.85	13.97	3.5
564.85	13.68	2.8
567.85	13.40	2.1
570.85	13.11	1.4
573.51	12.86	0.77
575.85	12.55	0.75
580.85	11.89	0.71
585.85	11.21	0.67
590.85	10.53	0.63
595.85	9.837	0.59
600.85	9.133	0.55
605.85	8.418	0.50
610.85	7.693	0.46
615.85	6.957	0.42

For A356 alloy, the solubility of hydrogen in the liquid phase of A356 aluminum alloy was determined from data available in the literature for the Al-Si system (Opie and Grant, 1950) as:

$$S_l = \exp\left(-A_0/T + B_0\right) \quad , \tag{4.2.1}$$

where A_0 and B_0 are determined based on concentration of Si, C_{Si}^l, in the liquid phase of the A356 alloy:

$$\begin{aligned} A_0 &= 5868.4 + 3700.6C_{Si}^l + 7217.3C_{Si}^l - 19601C_{Si}^l \\ B_0 &= 6.0289 + 2.8251C_{Si}^l + 3.7278C_{Si}^l - 13.324C_{Si}^l \end{aligned} \quad , \tag{4.2.2}$$

Magnesium segregates more during the eutectic reaction than during the primary solidification. For the aluminum-magnesium binary system, it is reported in the literature that magnesium increases the solubility of hydrogen (Anyalebechi, 1995). On the other hand, for aluminum-silicon system, the solubility decreases with the concentration of Si in the liquid. Thus, the effects of magnesium and silicon on solubility are quite opposite. Solubility of hydrogen in the liquid phase as a function of temperature for A356 and Al4.5Cu aluminum alloys is shown for comparison in Fig. 4.2.3. Because the existing models for predicting solubility in multicomponent alloys are not reliable, the solubility of hydrogen during the eutectic reaction is considered to be constant and equal to that at the onset of the eutectic reaction (Fig. 4.2.3).

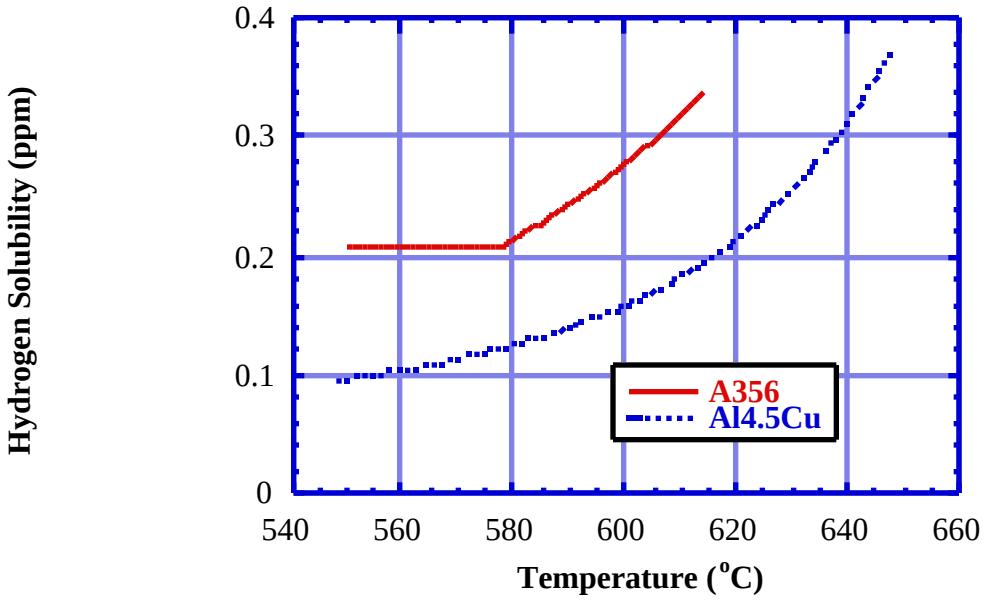

Fig. 4.2.3. Solubility of hydrogen in the liquid phase as a function of temperature for A356 and Al4.5Cu aluminum alloys.

4.2.2.2 Experimental Validation

The measured thermophysical properties were validated by comparing computed and experimentally measured cooling curves for a 0.14-m long bar casting poured in a green sand mold. Figure 4.2.4 shows a sketch of the bar casting and thermocouple locations at which temperatures were measured using type-K thermocouples connected to a PC-based data acquisition system. The filling and solidification of the bar casting were modeled using ProCAST™ software. The finite element mesh was constructed with eight-node brick elements using Patran™ and contained about 20,000 nodes. Figure 4.2.5 shows a comparison of experimental and calculated data. The experimental data is represented by symbols and the calculated data is represented by a series of dashed lines. The numbers in the legend refer

to thermocouple numbers and corresponding node numbers in the finite element model. The results indicate an excellent correlation between calculations and experiment, thereby validating the measured thermophysical properties. Properties for sand and mold-metal interface heat transfer coefficients were obtained from the literature or estimated based on past experience.

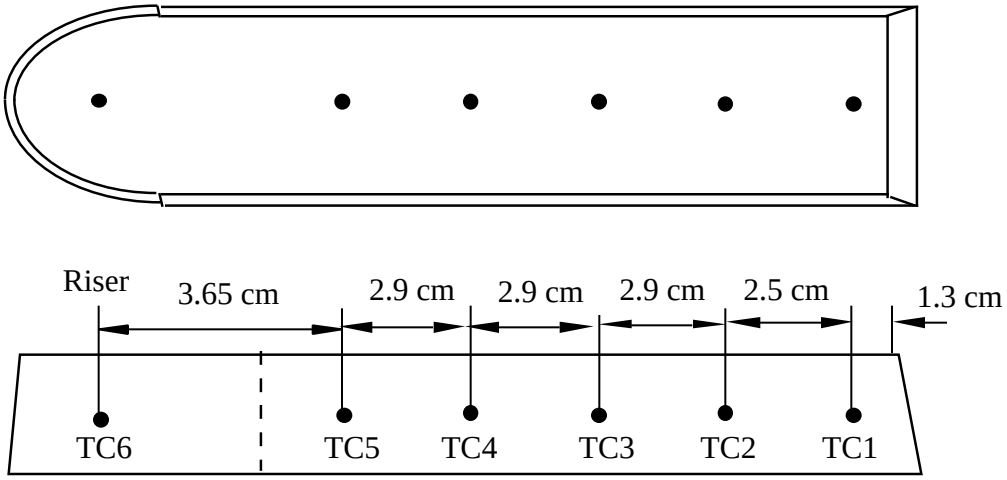

Fig. 4.2.4. Schematic illustration of test bar showing thermocouple locations. Only the riser pad is shown in the figure.

4.2.2.3 Sensitivity Analysis

Although accurate thermophysical properties are important for obtaining accurate results, the use of temperature dependent thermophysical properties imposes a penalty in terms of computing time, since additional computation or even nonlinearity is introduced into the problem. Consequently, it is useful to estimate the sensitivity of the calculated temperatures on the various thermophysical properties. Accordingly, results obtained using temperature dependent properties were compared to results obtained when constant properties were used. Table 4.2.5 lists the various conditions investigated. The column on the left lists the conditions for the control simulation using temperature dependent properties, comprising a single run. The column on the right lists the various conditions investigated for constant properties, comprising multiple runs. The effect of doubling the mesh size (coarse mesh spacing) on the calculated temperatures was also included, as there is often a tendency to use large mesh sizes in industry in an effort to limit the size of the problem. For each condition listed, all the other parameters were maintained the same as the control simulation. The difference in temperature in Thermocouple 1 between the control simulation and the variation is defined as the deviation for that condition and is plotted in Figs. 4.2.6*a* and *b*. A positive deviation indicates that the property variation results in a calculated temperature greater than that predicted by the control simulation, and consequently, by experiment. A negative deviation indicates that the property variation results in a temperature less than that predicted by the control simulation.

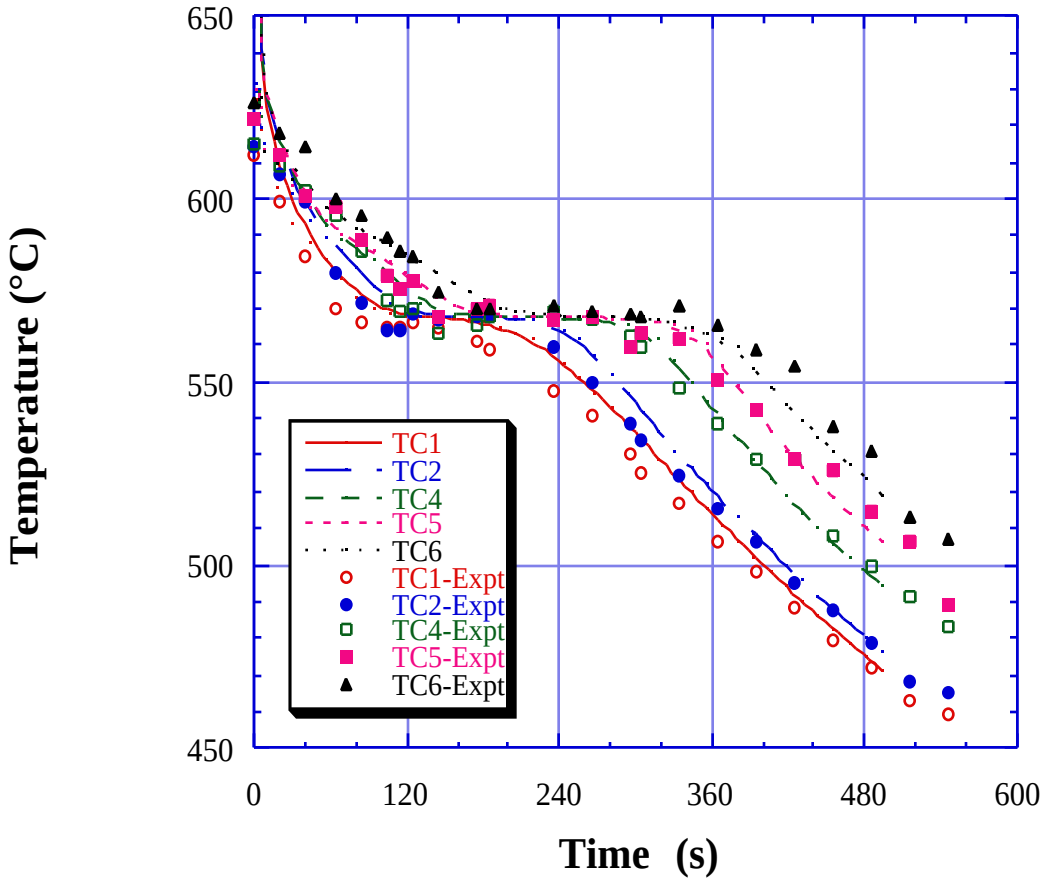

Fig. 4.2.5. Comparison of experimental cooling curves and those predicted by the control simulation for a test bar casting of 356 alloy.

It is clear from Fig. 4.2.6(*a* and *b)* that some thermophysical properties have a more drastic effect on the simulation than others. However, some general characteristics can be noted. First, a minimum deviation appears at the eutectic temperature T_S that is to be expected since there is a prolonged thermal arrest at this temperature, allowing these cooling curves to intersect. Second, the largest temperature deviation usually takes place immediately below the eutectic temperature, T_S, since the thermal gradient increases sharply at the end of solidification. Since gradients become fairly uniform across the length of the bar below the solidus, any deviation at the end of solidification remains relatively unchanged with time.

Table 4.2.5. Variations in thermophysical properties considered in sensitivity study.

Control Simulation	Sensitivity Study
$K = f(T)$	$K = K_{RT}$ or K_{TS}
$\rho = f(T)$	$\rho = \rho_{RT}$ or ρ_{TS}
$C_P = f(T)$	$C_P = C_{P,RT}$ or $C_{P,TS}$
$K_{SAND} = f(T)$	$K_{SAND} = K_{SAND,RT}$
$C_{P,SAND} = f(T)$	$C_{P,SAND} = C_{P,SAND,RT}$
Mesh Spacing Fine	Mesh Spacing Coarse
Non-Linear variation of Fraction Solid in Freezing Range	Linear variation of Fraction Solid in Freezing Range
Heat transfer Coefficient = 0.02 cal/s-cm^2-˚C	Heat Transfer Coefficient = ± 20%
Mold Filling	Instant Fill

K = Thermal conductivity, _ = density, C_P = specific heat.
RT = Room temperature value.
TS = Solidus temperature value.

In general, the use of constant properties introduces significant errors in the calculation, typically in the range of 5 to 10˚C. Although a 5˚C deviation does not seem very large, it could have a substantial difference on the calculated fraction solid of the alloy, and introduce significant errors in estimations of coherency and defects such microporosity and hot tears. The biggest surprise of the study was that the value of thermal conductivity used had a minimal effect on the results. This could be due to the fact that the thermal conductivity of aluminum alloys is already very high, and heat transfer is controlled by the resistance across the metal-mold interface and in the sand. However, even when a constant value of thermal conductivity was used, the deviation was noticeably smaller when the value of thermal conductivity at the solidus temperature was used. Thus, it is recommended that the thermal conductivity at the solidus temperature be used if a constant value is used in simulations.

The values used for the density and specific heat capacity of the alloy had a large impact on the calculated deviation. This may be expected since these values affect the sensible heat of the alloy. Again, the use of density or specific heat capacity values at the solidus temperature produced a lower deviation than the use of room temperature values. Consequently, in cases where a measured value of density at the solidus temperature is not available, it is recommended that the density at the solidus temperature be estimated by the use of the room temperature density and an adjustment for thermal expansion from room temperature to solidus temperature,

according to the relation _ = _RT / (1+_T)^3, where _ is the density at the solidus temperature, _RT is the room temperature value of the density, _ is the coefficient of thermal expansion, and T is the temperature difference between the solidus temperature and room temperature. Published values of the coefficient of thermal expansion for a wide range of alloys are available in many handbooks, and the values do not typically vary significantly within a class of alloys.

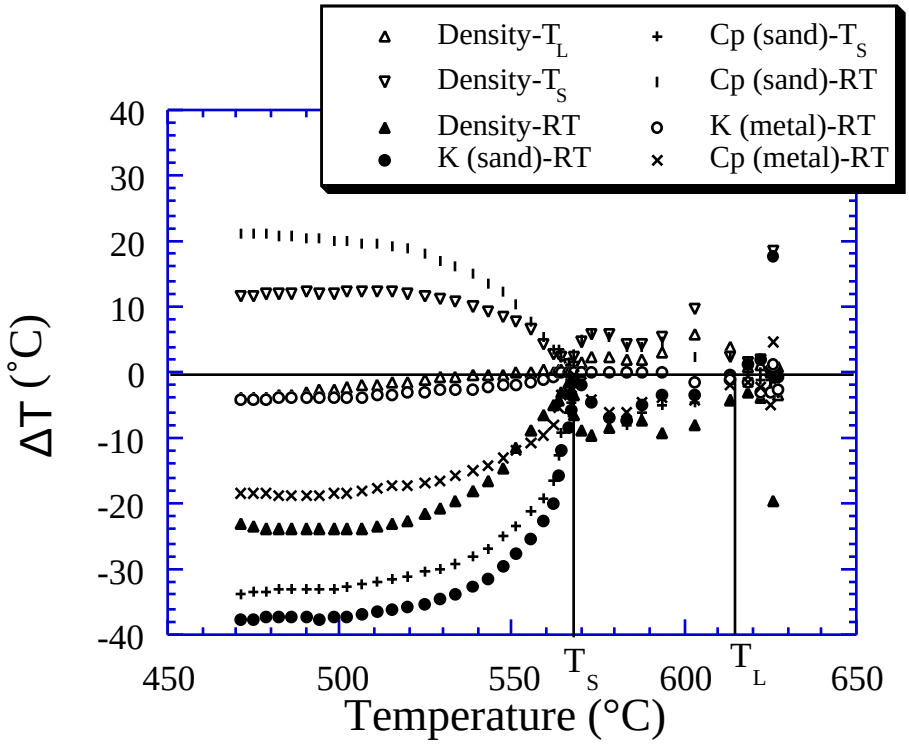

Fig. 4.2.6*a*. Deviation from control simulation for simulations using constant thermo-physical properties instead of properties varying with temperature.

In most cases, the thermophysical properties of the sand have a larger effect on the cooling curves than the thermophysical properties of the alloy. For example, all the changes in the conductivity of the metal had a relatively small effect on the cooling curves, while changes in the conductivity of the sand affected them significantly. This is again probably due to the fact that in the case of aluminum alloys, heat transfer is controlled more by the resistance to heat flow in the sand than in the metal. The results strongly reinforce the importance of the use of accurate, temperature dependent thermophysical properties. More importantly, the results suggest that more attention should be paid to the determination of thermophysical properties of the sand and alloy properties such as density.

Many other parameters such as the heat transfer coefficient, the assumption of an instantaneous filling of the mold, a doubling of the mesh spacing, i.e., mesh spacing of

0.5 to 2 cm rather than 0.25 to 1 cm, and the assumption of a linear evolution of latent heat in the freezing range, also had a strong effect on the calculated deviation from the control simulation, as shown in Fig. 4.2.6*b*. In fact, these parameters often exhibited a stronger effect on the simulation results than those due to the assumption of constant thermophysical property values shown in Fig. 4.2.6*a*. For example, the mold-metal interface heat transfer coefficient has a significant effect when changed by 25% from its default value of 0.020 cal/ sec-cm^2-˚C. Using a coarse mesh for simulations also results in a large deviation. A linear variation of the fraction solid vs. temperature, that leads to a linear variation of latent heat evolution, results in increasingly large deviations at during solidification with a maximum close to the solidus temperature. The results further emphasize that close attention must be paid to all simulation parameters, especially in cases in which quantitative estimates of temperature and fraction solid are needed.

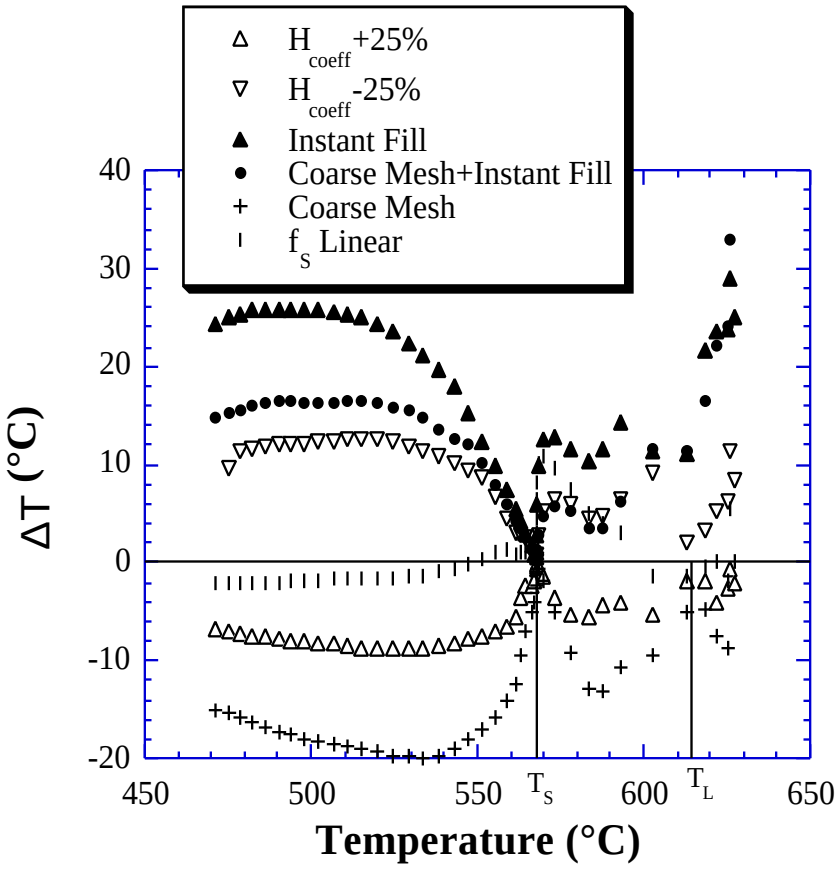

Fig. 4.2.6*b*. Deviation from control simulation for simulations using varying interface heat transfer coefficients, assumption of instant filling, a coarse mesh, and a linear variation of latent heat with temperature in the freezing range.

4.2.3 Comparison of Commercial Codes

In the following sections the commercial casting simulation packages EKK-CAP/ WRAFTS™, Flow-3D™, and ProCAST™ are compared with respect to their utility in the design and analyses of casting processes for the manufacture of structural aluminum alloy castings for chassis components. In addition, some of the issues involved in the development and use of computer models of the casting process are outlined. The actual casting modeling code that will be most suited to a particular foundry may be a function of user preference, since most of the commercial casting codes that are available today have very similar capabilities. However, this report will attempt to compare three of the most popular casting simulation packages available based on some important characteristics such as the user interface, mold filling simulation, heat flow/solidification simulation, and defect prediction. Finally, the comparisons are made on the best available information and the versions of the codes provided for evaluation. It is likely that newer versions of the above mentioned casting simulation packages will have features that are different and better than those listed. Consequently, a potential user is requested to update the information provided in this report with literature provided by the vendor.

4.2.3.1 Finite Difference vs. Finite Element Methods

An important difference in the implementation of a casting code results from the discretization approach used, viz., whether it is based on the finite difference method (FDM) or finite element method (FEM). Of the commercial casting modeling codes listed earlier, Flow-3D™ and Magma™ are finite difference-based codes, while EKK-CAP/WRAFTS™, Powercast™, and ProCAST™ are finite element-based codes.

Codes that use the finite difference technique normally use a structured grid, i.e., they divide up the geometry into regular blocks and specify temperatures, velocities, and properties at the center of each element. This allows them to discretize the geometry more rapidly but also means that curved surfaces have to be represented by a large number of linear segments. FDM approaches that use unstructured grids, i.e. elements that do not have to be regular solids, are under development but are not widely used in casting modeling.

FEM Codes, on the other hand, use unstructured grids. This allows improved representation of the geometry, but means that more time must be spent on its generation, since typically a greater amount of user interaction is required for the creation of complex surfaces. However, the tools available for generating the geometry, i.e., mesh generation, are improving rapidly and are also being automated, resulting in the increasing popularity and utility of finite element codes. Other benefits of FEM codes are that the more general nature of their implementation allows easier transfer of information across multiple codes, and that they are more suitable for the calculation of stress.

4.2.3.2 Mesh Generation

The first step in generating a mesh for use with either FDM or FEM codes is the creation of a solid model of the casting configuration, typically including the part, mold, and rigging. Commonly available 3D-CAD solid modeling packages include CATIA™, IDEAS™, ProEngineer™, and Unigraphics™. FDM codes typically input CAD geometry through an .STL file, which contains triangulated 3D surface data used as input for stereolithography or other rapid prototyping techniques, and create code-specific meshes for use with particular codes. FEM codes on the other hand, typically use input files directly from most commonly available mesh generation packages. Mesh generation packages available for use with FEM codes include AMESH™, IDEAS™, MeshCAST™, Patran™, ProEngineer™, and Unigraphics™.

4.2.3.3 Key Features

This section will attempt to compare three of the most popular casting simulation packages available based on some important characteristics such as the user interface, thermophysical property input, mold filling simulation, heat flow/solidification simulation, stress simulation, and microstructure and defect prediction. Table 4.2.6 lists a comparison of the key features for the three casting simulation packages EKK-CAP/WRAFTS™, Flow-3D™, and ProCAST™, at the start of the program.

4.2.4 Discussion

Most of the commercial casting codes that are available today have very similar capabilities. The majority of casting process developments will be greatly assisted by the use of any of the commercially available casting simulation codes, as opposed to the use of rule of thumb or trial and error approaches, although experience will continue to be an important factor for some time to come. In particular, the simulation of fluid flow during mold filling should be used to identify areas of jetting or recirculation, air entrapment, and resulting defects such as oxide films and inclusions, and the simulation of heat flow during solidification should be used to identify the last regions to freeze that are potential areas of solidification shrinkage. In addition, modeling heat flow and mold filling can identify the potential for laps and cold shuts, i.e., the incomplete fusion of metal streams during filling or the incomplete filling of molds due to the loss of superheat in the liquid.

Typically, existing commercial casting codes do not directly predict casting defects such as oxide films, laps, or solidification shrinkage; rather, the propensity for such defects is either be inferred from the calculated filling and solidification patterns or are determined by a subsequent analysis during the post-processing of the results. Unfortunately, such an approach cannot provide quantitative measures of defect size and distribution, and consequently cannot be used to predict casting properties or performance. Similarly, microstructure modeling is less commonly available

and less useful in the present form available in commercial codes, since the techniques and the knowledge base for predicting microstructure are still being developed. However, both the modeling of microstructure and the ability to predict defects quantitatively and accurately represent important areas for future development.

Table 4.2.6. Comparison of key features of popular casting simulation packages at the start of the program.

Features	EKK CAP/WRAFTS	Flow-3D	ProCAST
Mesh Input	· Good · Any FEM mesh	· Fair · Creates mesh from .STL file	· Good · Any FEM mesh
User Interface	· Good	· Poor	· Good
Thermophysical Properties Input	· Fair - ASCII input · Some constant properties · Limits on ranges	· Poor-Namelist format · Some limits	· Good · Very flexible
Mold Filling/ Fluid Flow	· Good · Navier-Stokes	· Very good · Navier-Stokes	· Good · Darcy-Modified Navier-Stokes
Solidification/ Heat Transfer	· Conduction only	· Coupled with fluid flow	· Very good, coupled with fluid flow
Defect Prediction	· Niyama	· Niyama	· Niyama
Microstructure	· Not available · Cell spacing possible from cooling rate	· Not available · Cell spacing possible from cooling rate	· Module available · Needs further development
Stress	· Can Be Developed	· Not Suitable	· Module Available · Needs Validation
Comments	· FEM code · Code has some limitations · Separate codes for filling and solidification · Good potential for future development	· FDM code · Excellent flow capabilities but hampered by poor user interface and unsuitability for modeling stress · Geometry representation may be unsatisfactory for thin sections	· FEM code · Feature rich · Very flexible code · Good potential for future development

In particular, codes that are suitable for use in the design and analyses of casting processes for structural safety-critical castings must allow the quantitative prediction of defects and microstructure. Microstructural features of interest for the prediction of casting performance and properties includes pore size, pore density, and pore distribution, and details of microstructure such as grain size and second phase particle size and distribution. In the case of aluminum alloys, this includes features such as silicon particles and intermetallics. Figure 4.2.7 provides a comparison of features of commercial codes at the start of this program and the scope of development for applicability to the design of structural safety-critical castings.

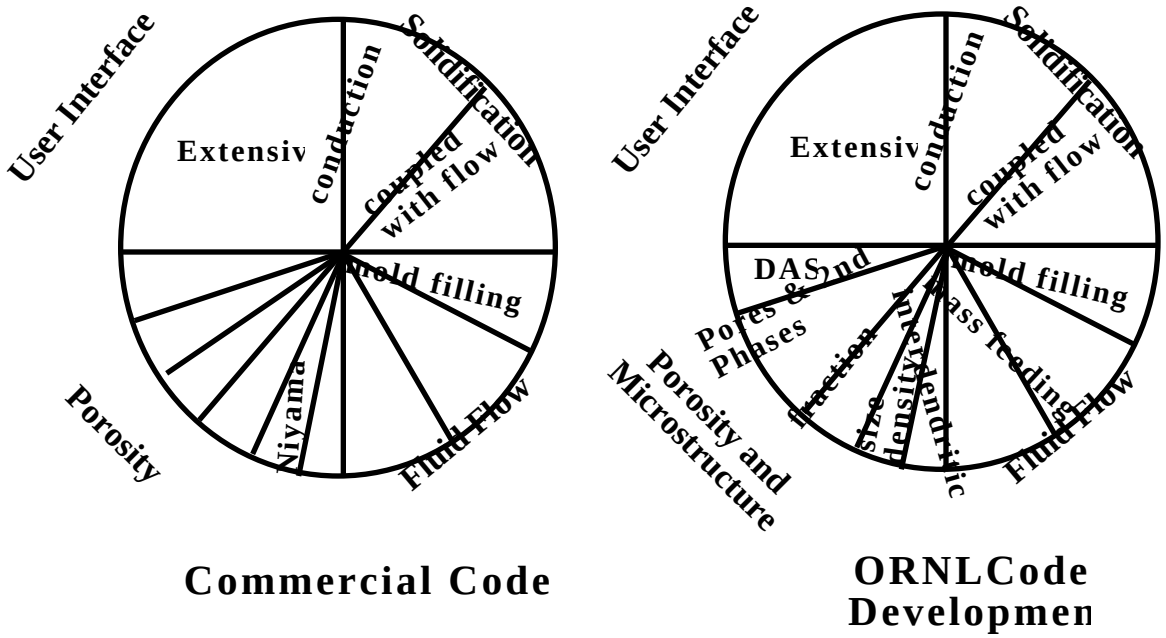

Fig. 4.2.7. Comparisons of features of commercial codes at the start of the program and the scope of development for applicability to the design of structural and safety critical castings.

4.3 MEASUREMENT OF LIQUID PERMEABILITY IN THE MUSHY ZONE

The permeability of interdendritic liquids flowing through dendritic structures is an important parameter needed to predict the level of porosity in castings. The permeability is a component of Darcy's Law, used to estimate the pressure drop due to the resistance to the flow of interdendritic fluid to feed shrinkage. Therefore, much research has focused on measuring the permeability of alloys in the mushy zone (Piwonka and Flemings, 1966; Apelian, Flemings, and Mehrabian, 1974; Murakami and Okamoto, 1984; Streat and Weinberg, 1976; Nasser-Rafi, Deshmukh, and Poirier, 1985; Poirier and Ganesan, 1992; Poirier and Ocansey, 1993; Ocansey, Bhat, Poirier, and Finn, 1994; Paradies, Arnberg, Thevik, and Mo, 1995; Poirier, 1987). The Kozeny-Carman equation for liquid permeability in the mushy zones of alloys may be written as

$$K_s = \frac{g_L^3}{k_C S_V^2} \quad , \tag{4.3.1}$$

where g_L is the volume fraction liquid, S_V, is the specific solid surface area (i.e., surface area of solid in unit volume of sample), and k_C is the Kozeny-Carman constant, which takes on various values depending of the characteristics of the porous medium (Carman, 1937).

The first systematic measurement of liquid permeability in the mushy zones of alloys was made by (Piwonka and Flemings, 1966) who used molten lead to measure the permeability of liquid metal in Al-4.5% Cu alloy. Later, (Apelian et al., 1974) measured the permeability of water in partially solidified dendritic networks of aluminum-silicon alloys, and (Murakami and Okamoto, 1984) used a transparent borneol-paraffin system to study permeability in equiaxed structures. These studies showed that permeability was proportional to the volume fraction liquid raised to a power "n", g_L^n, where n = 2 to 3.3.

While the above measurements yield valuable estimates of permeability, the primary disadvantage to these approaches is that the liquid used for the experiment was not the eutectic liquid, and thus the result may not be representative of actual castings (Nasser-Rafi, Deshmukh, and Poirier, 1985). To overcome this problem, many studies used eutectic liquid to measure the permeability in both equiaxed (Streat and Weinberg, 1976; Nasser-Rafi, Deshmukh, and Poirier, 1985; Poirier and Ganesan, 1992; Poirier and Ocansey, 1993; Ocansey, Bhat, Poirier, and Finn, 1994; Paradies, Arnberg, Thevik, and Mo, 1995) and columnar (Poirier, 1987) dendritic structures. Poirier and Ganesan (1992) made measurements on equiaxed structures using eutectic liquid in aluminum-copper alloys and correlated permeability to the alloy microstructure by the Kozeny-Carman relation. The results of this study, together with a more recent study, (Ocansey, Bhat, Poirier, and Finn, 1995) are compiled Fig. 4.3.1. Surprisingly, the scatter on this data spans approximately one and a half orders of magnitude. This is most likely due to the fact that microstructures undergo coarsening during the test and that the permeability increases with time, since in these and other measurements, the permeability was treated as a constant over time. In this paper, a modified approach for calculating permeability from experimental data is presented in which permeability can be determined as a function of time, using the same experimental technique for measuring permeability employed by previous researchers. Permeabilities were determined for aluminum-copper alloys and were also correlated with the microstructural

parameters g_L and S_V by the Kozeny-Carman equation. A marked decrease in experimental scatter was achieved for the analysis used in this study.

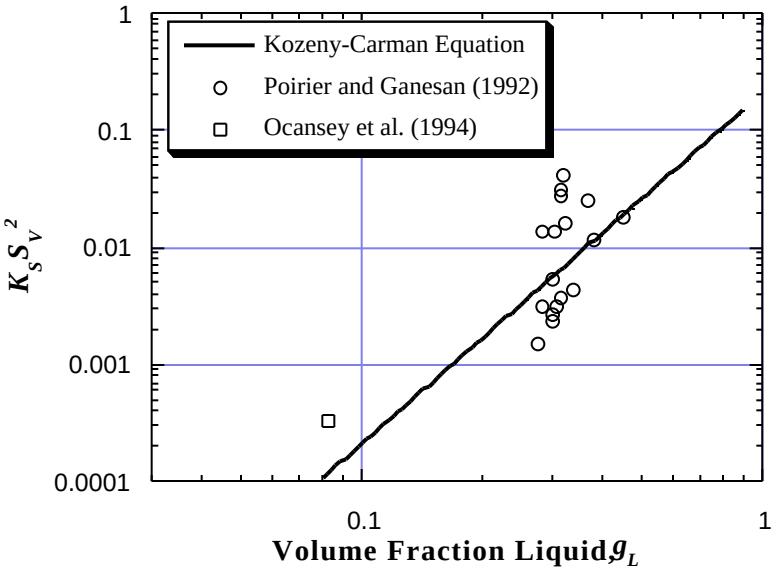

Fig. 4.3.1. Data for aluminum-copper alloy from the literature (Poirier and Ganesan, 1992; Ocansey, Bhat, Poirier, and Finn, 1994), indicating poor correlation with the Kozeny-Carman equation.

4.3.1 Experimental Procedure

A permeameter cell was constructed from 316 stainless steel alloy pipefittings. Threaded tubes, nominally 15.9 mm (0.625 in.) diam and 152 mm (5.98 in.) long (0.5 in. diam nominal, Schedule 40 standard 6-in. threaded nipples), were screwed together using 316 stainless steel alloy elbows (one threaded 90˚ elbow with both ends female, and one threaded 90˚ service or street elbow with one end female and the other end male) to form a U-shaped permeameter cell. This resulted in a permeameter in which the inlet and outlet legs were approximately 165 mm (6.5 in.) long and
70 mm (2.76.in) apart (center to center). The cross-sectional areas in the inlet and the outlet legs were kept equal to simplify the calculation. The interior surface of the permeameter cell was coated with boron nitride to prevent reaction with flux and aluminum alloy. Samples of Al-15.42% Cu and Al-8.68% Cu alloys were cast separately in the form of 20-mm-diam rods (0.79 in.) in a graphite mold preheated to 343˚C. The rods were machined down to 16 mm (0.63 in.) diam, and threads (0.625 in.-18) were machined into them. The internal diameter of one of the elbows (male end of street elbow) was drilled and tapped to accept the threaded rod sample. Samples, 20 mm (0.79 in.) in length, were cut and screwed into the coated permeameter. Ceramic cement was used on the internal threads of the elbow containing the sample to prevent leaks from occurring around the sample. In order to ensure an isothermal environment, the permeameter was mounted in a holder and suspended in a liquid tin bath without allowing the exterior of the permeameter to come in contact with the sides or bottom of the crucible. The graphite crucible containing the liquid tin was 100 mm (3.94 in.) diam and 280 mm (11 in.) tall. It was placed and heated in an well-insulated calm-shell resistance furnace controlled by a

Honeywell model 3000 controller and a Control Concepts, Inc. model 1020 SCR unit. Temperature measurements in the liquid tin bath indicated that the temperature remained constant during the experiment to within 2˚C (3.6°F). A schematic illustration of the experimental setup used for permeability measurements is given in Fig. 4.3.2.

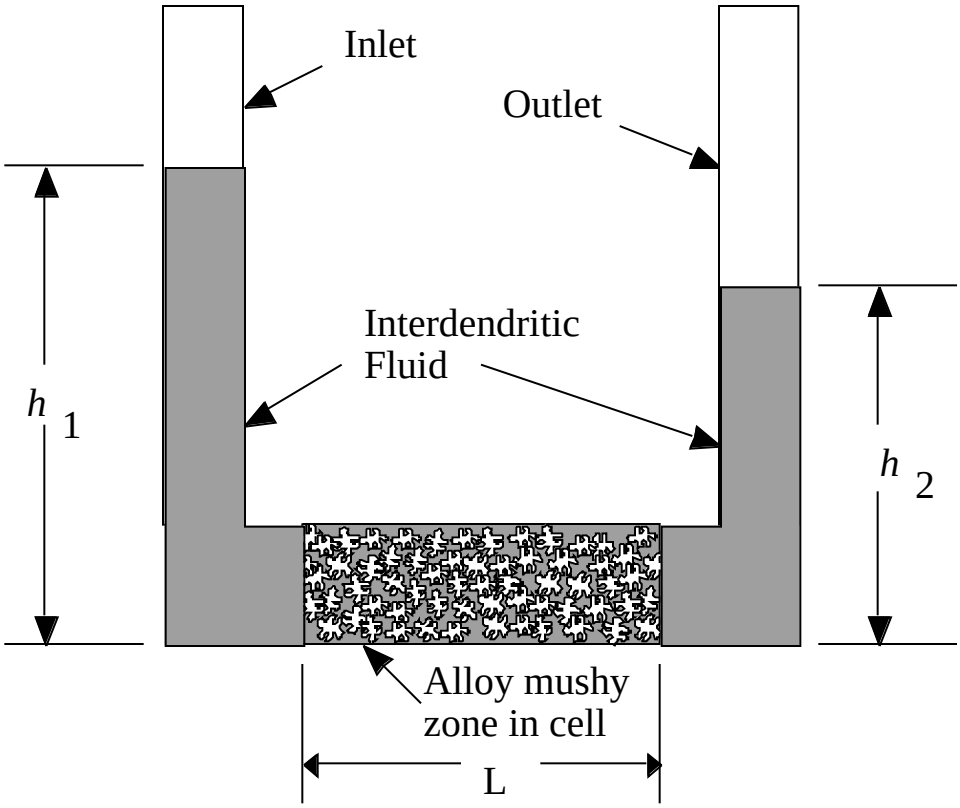

Fig. 4.3.2. Schematic illustration of the experimental setup used for measurements of liquid permeability in the mushy zones of alloys. The permeameter was suspended in a liquid tin bath to maintain an isothermal environment.

Both the permeameter containing the sample and the holder were preheated to 500˚C (932°F) for 20 min and inserted into the liquid tin bath, which was maintained at a temperature of 555˚C (1022°F). The temperature inside the permeameter was monitored, and when it reached the eutectic temperature [548˚C (1018.4°F)], eutectic liquid was added to both legs of the permeameter. Graphite floats with SiC fibers attached to them were placed in the inlet and outlet to monitor h_1 and h_2 as a function of time. Since more eutectic liquid was poured in the inlet leg than in the outlet, it flowed through the semi-solid sample to the outlet leg, where the liquid height could be accurately measured using the float.

4.3.2 Analysis of Permeability from Flow Measurements

According to the differential form of Darcy's Law, the superficial velocity, υ, at which a fluid flows through a porous medium is related to a pressure gradient, *dp/dx*, by

$$\upsilon = -\frac{K_S}{\mu}\frac{dp}{dx} \quad , \tag{4.3.2}$$

where K_S is the specific permeability of the sample and μ is the viscosity of the liquid. Using the analysis of (Poirier and Ganesan, 1992) but neglecting the weight of the float in the outlet leg and making the amount of flux the same in both the inlet and outlet legs, the pressure drop is given by

$$\frac{dp}{dx} = \frac{\rho g(h_2 - h_1)}{L} \quad , \tag{4.3.3}$$

where ρ is the density of the eutectic liquid, g is the acceleration due to gravity, L is the length of the mushy alloy sample, and h_1 and h_2 are the heights of liquid in the inlet and outlet legs, respectively.

The conservation of mass gives

$$a_3\upsilon = a\frac{dh_2}{dt} \quad , \tag{4.3.4}$$

and

$$a\frac{dh_2}{dt} = -a\frac{dh_1}{dt} \quad , \tag{4.3.5}$$

where a_3 is the cross-sectional area of the sample and a the cross-sectional area of the inlet and outlet legs.

Integration of Eq. 4.3.5 gives

$$h_2 + h_1 = h_{20} + h_{10} = H \quad , \tag{4.3.6}$$

where H is a constant and h_{20} and h_{10} are the initial heights of the eutectic liquid in the outlet and inlet legs.

Substituting Eqs. 4.3.3, 4.3.4, and 4.3.6 into Eq. 4.3.2 yields

$$\frac{dh_2}{dt} = \rho g\frac{K_S}{\mu L}\frac{a_3}{a}(H - 2h_2) \quad . \tag{4.3.7}$$

Equation 4.3.7 is essentially identical to the form derived by (Poirier and Ganesan, 1992).

In Eq. 4.3.7, the velocity dh_2/dt may be obtained by the derivative to a polynomial fit of the h_2 versus t data. Since both dh_2/dt and h_2 are known as a function of time, the permeability can be calculated as a function of time using Eq. 4.3.7.

4.3.3 Permeability Measurements

Figure 4.3.3 shows the height (h_2) versus time recorded for a typical run. As is evident, the outlet height increased slowly at first, then increased more rapidly with time and leveled off toward the end of the experiment. Figure 4.3.4 shows a graphic representation of Eq. 4.3.7 and plots the flow rate as represented by the change in outlet height dh_2/dt as a function of the height $H-2h_2$ for the data in Fig. 4.3.3. If K_S were constant, the relationship between dh_2/dt and $H-2h_2$ in Fig. 4.3.4 would be linear, according to Eq. 4.3.7. Any variation in K_S during the experiment causes the data to deviate from linearity. As is evident, K_S is not constant over time. In Fig. 4.3.4, K_S is given by the slope of a line passing through a data point and intersecting the origin. Figure 4.3.4 also suggests that at the beginning of the test, coarsening is rapid and the flow rate (and permeability) increases even though the pressure head is decreasing. After some time, the flow rate begins to decrease as the liquid levels in the inlet and outlet legs get closer. The apparent decrease in the permeability at the end of the test is an indication of the blockage of the inlet surface of the sample by flux, oxide films, inclusions, or precipitates from the liquid. Clearly, the data are no longer usable for determining permeability after blockage occurs.

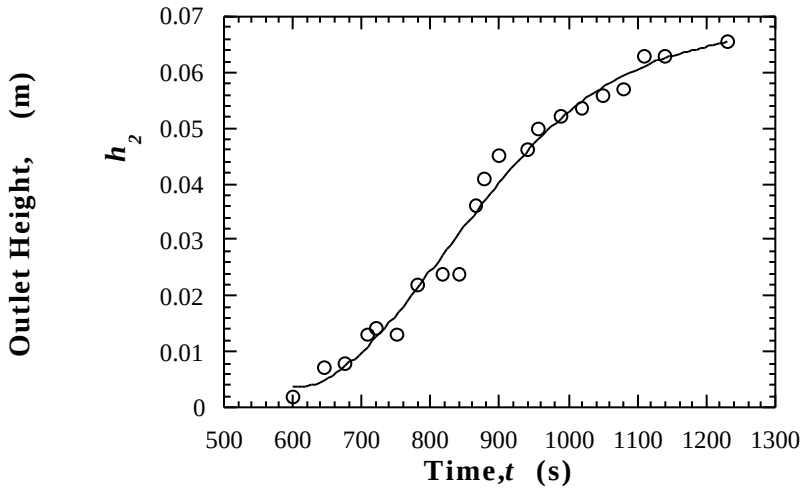

Fig. 4.3.3. Outlet height (h_2) measured versus time during a permeability test on an Al-15.42% Cu alloy sample.

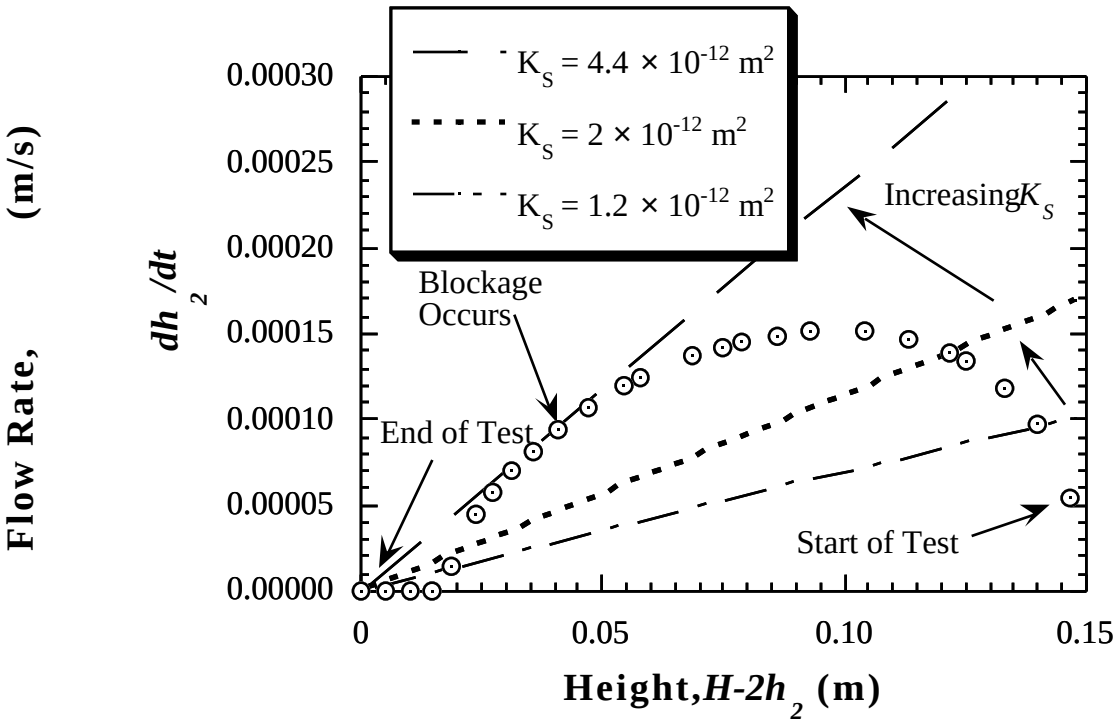

Fig. 4.3.4. Flow rate as represented by the change in outlet height (dh_2/dt) versus height ($H-2h_2$) for Al-15.42% Cu alloy for the data in Fig. 4.3.3. K_S is given by the slope of a line passing through a data point and intersecting the origin according to the relationship in Eq. 4.3.7.

Using Eq. 4.3.7, the permeability can be calculated as a function of time at any point during the test, using appropriate values of ρ and μ. In this study, the density of the eutectic liquid was assumed to be 3200 kg/m^3 (Ganesan and Poirier, 1987) and its viscosity was assumed to be 2.09×10^{-3} Ns/m^2. (Ganesan, Speiser, and Poirier, 1987). Figure 4.3.5 shows a plot of permeability as calculated from Eq. 4.3.7 for the experimental data shown in Fig. 4.3.3. It indicates that the permeability varies from 8×10^{-13} to 4.4×10^{-12} m^2 during the test. The increase in K_S is most likely due to a decrease in S_V from coarsening. Figure 4.3.6 shows typical microstructures for Al-15.4% Cu alloy at the beginning and end of the test. Increased flow can also occur due to the formation of preferential flow channels during the experiment, and care must be taken to avoid channel formation during an experiment. Figure 4.3.7 shows an optical micrograph of a permeability sample in which a channel has formed.

4.3.4 Correlation of Permeability with Microstructure

In order to correlate permeability with microstructural parameters g_L and S_V via the Kozeny-Carman equation, isothermal coarsening experiments were conducted on Al-8.68% Cu and Al-15.42% Cu alloy samples. The results of these experiments were compared to the microstructures of the permeability specimens. This comparison was useful in estimating microstructural parameters at time intervals during the permeability test.

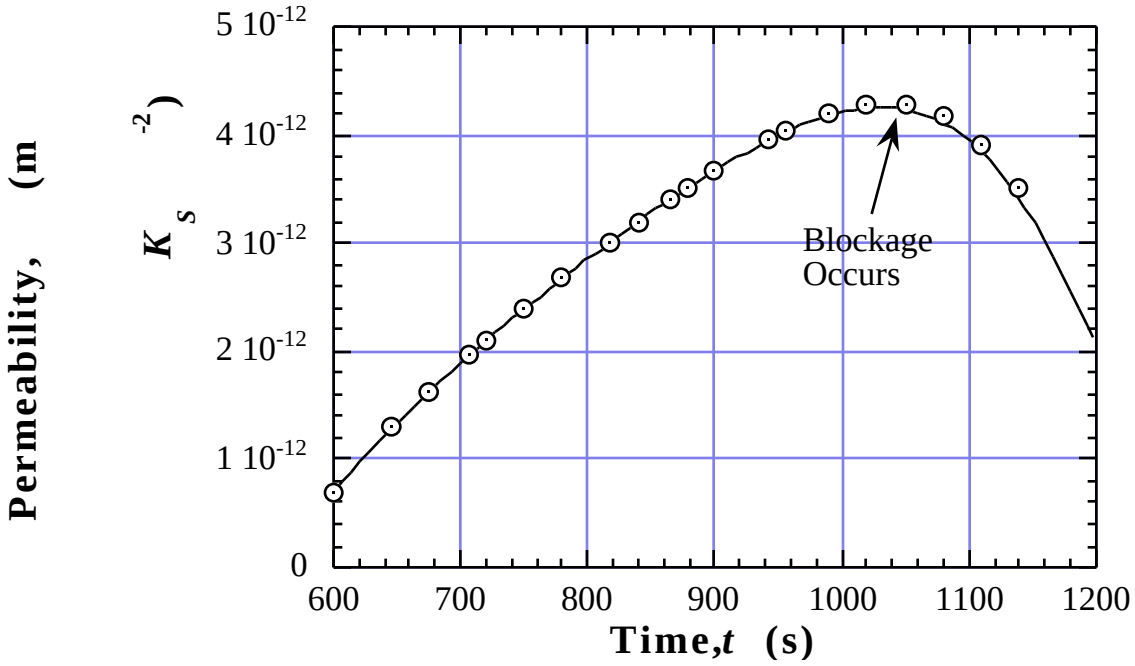

Fig. 4.3.5. Calculated values of permeability for Al-15.42% Cu alloy for the data shown in Fig. 4.3.3, showing that K_S increases as a function of time until some blockage occurs.

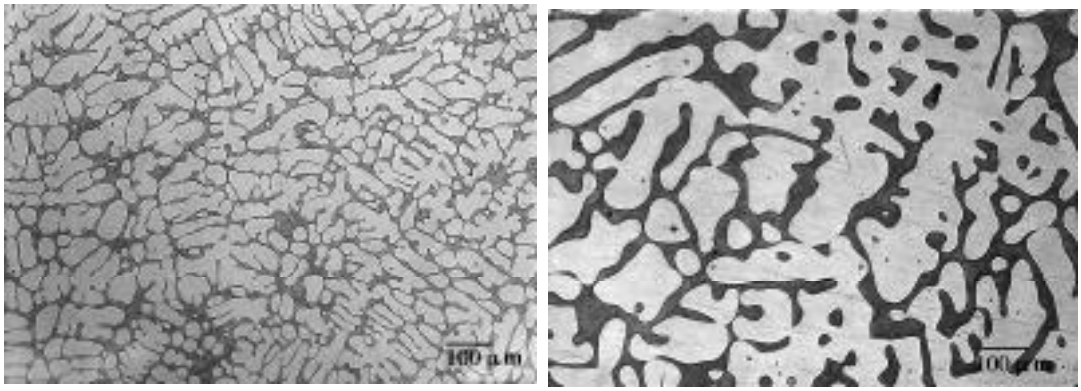

(*a*) (*b*)

Fig. 4.3.6. Typical microstructures for Al-15.42% Cu alloy at *(a)* the start and *(b)* the end of a permeability test.

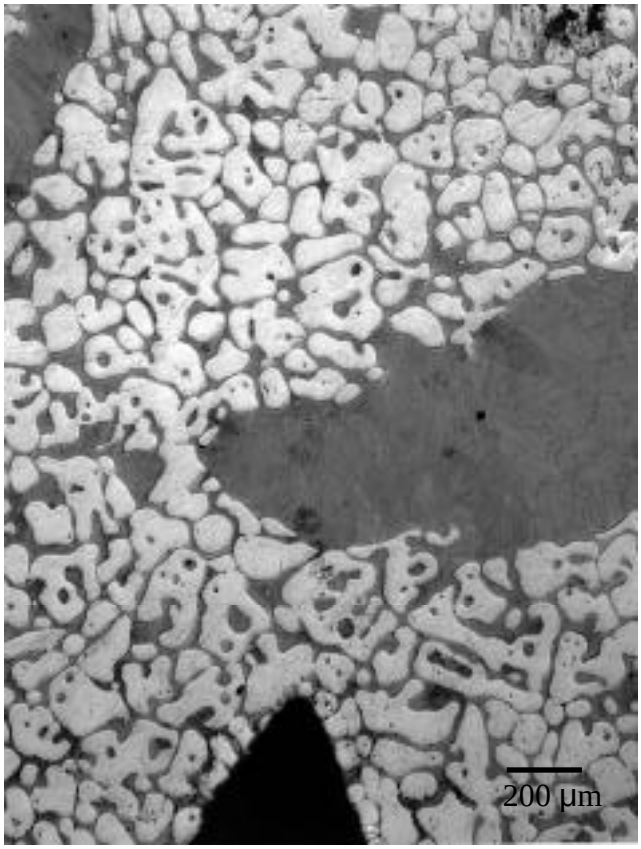

Fig. 4.3.7 Optical micrograph of permeability sample exhibiting a preferential flow channel that formed during the test.

4.3.4.1 Measurement of S_V

Small samples were loaded in the permeameter and held in the bath of molten tin at a temperature 5˚C (9°F) higher than the eutectic temperature. The samples were quenched in water at specific times. Measurements of microstructural parameters (i.e., S_V and g_L) were made on a Bueler Omnimet™ Quantitative Image Analyzer on metallographic specimens of sample cross sections. S_V was determined by the linear intercept method (Metals Handbook Desk Edition, 1985).

Figure 4.3.8 shows the results of S_V measurements from Al-15.42% Cu and Al-8.68% Cu alloy samples subjected to isothermal coarsening at 555˚C (1022°F) and from samples used for permeability tests. The results show that the microstructures of isothermal coarsening samples coarsen at a rate consistent with Oswald ripening (i.e., $S_V = K_{OR}t^{-1/3}$). Isothermal coarsening rate constants, K_{OR}, for Al-15.42% Cu and Al-8.68% Cu alloy samples were measured to be 633000 $s^{1/3}$/m and 316000 $s^{1/3}$/m, respectively. However, S_V values measured from permeability specimens were significantly smaller for comparable times at the test temperature, indicating the likelihood of enhanced coarsening rates in the presence of fluid flow during a permeability test.

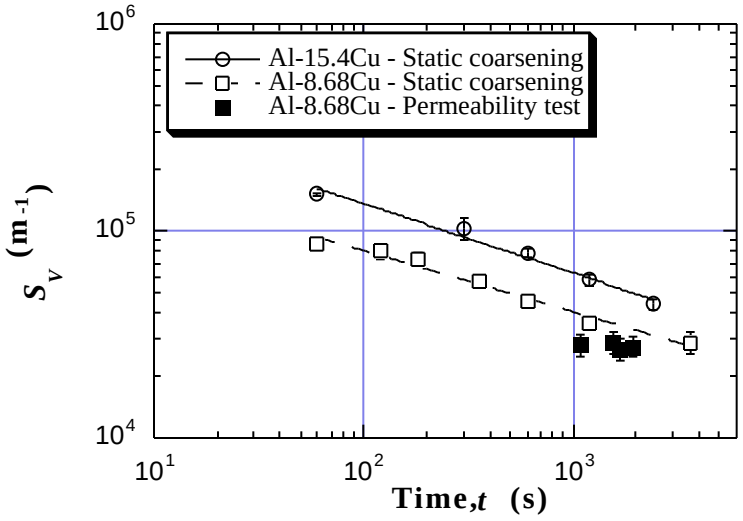

Fig. 4.3.8. Specific solid surface area, S_V, measured on Al-15.42% Cu and Al-8.68% Cu alloy samples after isothermal coarsening experiments at 555˚C (1022˚F). S_V measured on permeability samples of Al-8.68% Cu alloy is also shown.

Figure 4.3.9(*a* and *b*) show optical micrographs of an isothermal coarsening specimen and a permeability specimen after the test that were quenched after approximately 1300 s at the test temperature. It can be seen from these micrographs that a difference exists between the microstructures in the absence of fluid flow and with fluid flow. Measurements of S_V for these two samples yielded values of 52300 and 38700 m^{-1}. The increased coarsening rates in the presence of fluid flow are likely to be exhibited in most solidification processes, and needs to be taken into account in the analyses of microstructural evolution in these processes. Further investigation of this phenomenon is warranted.

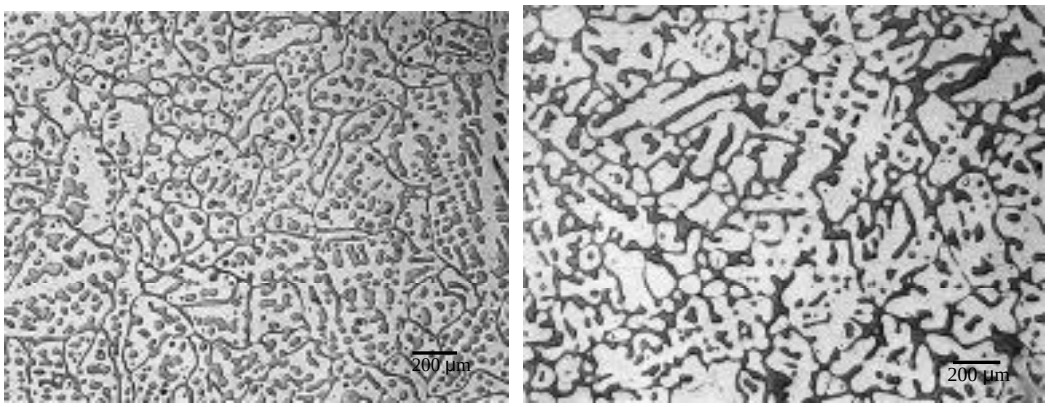

(*a*) (*b*)

Fig. 4.3.9. Optical micrographs of *(a)* an isothermally coarsened specimen, S_V = 52300 m^{-1} and *(b)* a permeability specimen, S_V = 38700 m^{-1}, of Al-15.42% Cu alloy held at 555˚C (1022˚F) for approximately 1300 s.

4.3.4.2 Measurement of g_L

Volume fraction liquid was estimated from a measurement of area fraction using the image analyzer used for S_V measurements. Figure 4.3.10 shows g_L measured as a function of time from isothermal coarsening samples and from samples used for permeability tests. The results indicate that the fraction liquid reduces to a value close to the equilibrium value relatively quickly when the sample is held isothermally at the eutectic temperature, indicating that back diffusion
(i.e., diffusion in the solid) is quite rapid at this temperature. The measured values of g_L for permeability tests and isothermal coarsening tests do not appear to vary significantly. However, this reduction of g_L with time must be taken into account in the analyses of permeability measurements.

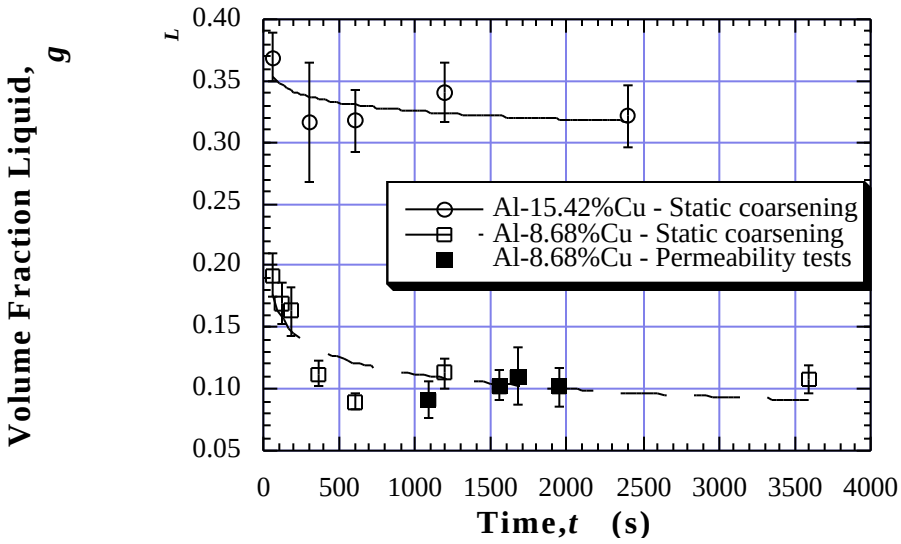

Fig. 4.3.10. Volume fraction liquid, g_L, measured on Al-15.42% Cu and Al-8.68% Cu alloy samples after isothermal coarsening experiments at 555˚C (1022°F). g_L measured on permeability samples of Al-8.68% Cu alloy is also shown.

4.3.4.3 Kozeny-Carman Correlation

Figure 4.3.11 plots $K_S S_V^2$ versus g_L for the data on Al-8.68 and Al-15.42% Cu alloys measured in this study in relation to the Kozeny-Carman equation plotted for $k_C = 5$. The spread of the data obtained in this study is much smaller than for data from previous studies. Although the reduced data scatter may be the result of more careful permeability measurements, it is believed primarily to result from a sounder methodology for calculating permeability from the flow versus time data and the use of accurate values for S_V and g_L during the test. Importantly, the results of this study confirm that the Kozeny-Carman equation allows an accurate representation of liquid permeability in the mushy zones of alloys, allowing greater confidence in the use of Darcy's law for calculating pressure distributions during solidification.

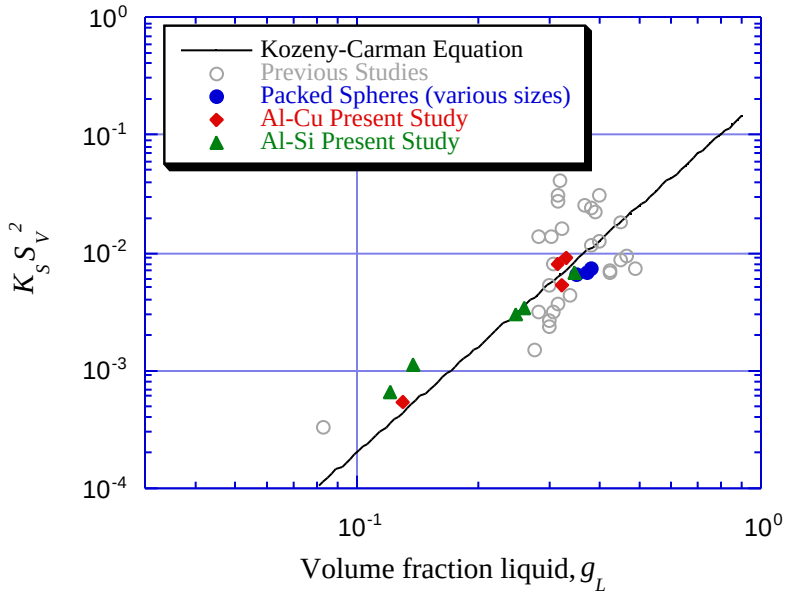

Fig. 4.3.11. Values of permeability K_S, specific surface area, S_V, and volume fraction liquid, g_L, measured in this study plotted in relation to the Kozeny-Carman equation plotted for k_C = 5 and compared to data from literature. (Poirier and Ganesan, 1992; Ocansey, Bhat, Poirier, and Finn, 1994).

4.3.5 Summary

A modified technique was developed for calculating liquid permeability in the mushy zones of alloys as a function of time during a permeability test. This method yields more accurate values than previous methods that average permeabilities over time during a test.

Permeability increases as a function of time due to microstructural coarsening in the sample during the test. Calculations carried out as a function of time show that permeability could vary one-half an order of magnitude over the course of the test.

Coarsening rates during the permeability test in the presence of fluid flow appear to be larger than coarsening rates measured in static coarsening tests without fluid flow The increased coarsening rates in the presence of fluid flow are likely to be exhibited in most solidification processes, and needs to be taken into account in the analyses of microstructural evolution in these processes.

Volume fractions of liquid decrease during isothermal coarsening experiments and during the permeability test due to significant back diffusion in the solid at the test temperature. This leads to a decrease in the measured permeability of the sample.

When the effect of coarsening and back-diffusion during a permeability test are taken into account, the agreement between experimental data and the Kozeny-Carman equation is excellent, and results in a large decrease in scatter when compared to data from previous studies.

The results of this study confirm that the Kozeny-Carman equation allows an accurate representation of liquid permeability in the mushy zones of alloys, allowing greater confidence in the use of Darcy's law for calculating pressure distributions during solidification. For the data obtained in this study, the best fit with the Kozeny-Carman equation was obtained for a value of $k_C = 5$.

4.4 MODELING OF MICROPOROSITY IN A356 ALLOY CASTINGS

The use of aluminum alloy castings for structural components offers significant opportunities for reducing the weight of automobiles, since aluminum alloy components are typically about half the weight of the steel, cast iron, or ductile iron component that they replace. However, the performance requirements of structural components, particularly chassis or suspension components, places greater requirements on the mechanical properties of the components. An important factor that leads to a decrease in the mechanical properties of castings is the presence of microporosity. This report outlines recent results on the development of a comprehensive model for predicting porosity distributions in complex shaped aluminum alloy castings. This report provides an overview of the physics involved in porosity formation, hydrogen and shrinkage porosity. Constitutive model developments are also presented for the numerical simulation of fluid flow, heat transfer, and solidification during casting. Finally, the solution algorithms and details of the implementation methodology are provided. Information is also provided on permeability data and thermophysical properties needed for the numerical simulation of A356 aluminum alloy castings.

4.4.1 Porosity Formation in Aluminum Alloys

The occurrence of microporosity in aluminum alloys is due to the combined effects of solidification shrinkage and gas evolution. During solidification, hydrogen dissolved in the liquid aluminum can precipitate due to the higher solubility of hydrogen in the liquid as compared to that in the solid phase. Gas pores can form when the partial pressure of H_2 that corresponds to the hydrogen concentration within the liquid exceeds the local pressure in the mushy zone by an amount necessary to overcome the surface energy forces (Piwonka and Flemings, 1966; Kubo and Pehlke, 1985). The local pressure in the mushy zone, P_m results from (1) the ambient pressure, (2) metallostatic head, and (3) resistance to the flow of fluid to feed solidification shrinkage.

In alloy castings, two types of porosity are identified. Shrinkage porosity occurs when solidification shrinkage cannot be compensated (Piwonka and Flemings, 1966). Gas porosity occurs when the gas concentration in the liquid is higher than its solubility (Whittenberger and Rhines, 1952). In most situations, both types of porosity formation mechanisms (i.e., inadequate feeding and hydrogen evolution) play important roles in forming porosity. Inadequate feeding causes a local pressure drop so that the gas becomes more supersaturated, resulting in earlier formation of the gas porosity. During the solidification of local isolated liquid pools, shrinkage generates pores filled with gas. It is the interplay of these mechanisms that gives rise to porosity in castings.

During the phase change from the liquid to solid, aluminum alloys undergo a volumetric shrinkage of several percent depending on the their composition. If this shrinkage is not fed, pores occur. These volumetric changes, which are associated with solidification, are compensated by the interdendritic liquid feeding. Campbell (1969) described different feeding mechanisms in a solidifying casting. Inadequate feeding normally occurs in the interdendritic feeding region where the dendritic network exhibits a large resistance to fluid flow. Ultimately,

if the liquid fraction is so small that the solid separates the remaining liquid, the solidification shrinkage of this liquid will inevitably produce pores since feeding becomes impossible.

Shrinkage porosity takes place either as centerline porosity or dispersed pores depending on the mode of solidification. Alloys with a short freezing range and lower thermal conductivity like steel exhibit a large solid fraction gradient from surface to center. In such alloys, feeding toward the end of solidification occurs through a single central channel. Accordingly, porosity is also confined to this channel, is mainly macroscopic, and is termed centerline porosity. Alloys with a long freezing range and high thermal conductivity like aluminum alloys solidify in a mushy manner. Feeding in such alloys is interdendritic and porosity is usually microscopic and dispersed.

4.4.2 Pore Nucleation

In castings, nucleation of pores can be expected to occur primarily at heterogeneous nucleation sites. Heterogeneous sites are inherent in most castings, such as the solid-liquid interface and inclusions. The calculation of pressure or supersaturation required for nucleation on planar interfaces is very high (Wilcox and Kou, 1973; Wilt 1986).

Chalmers (1964), Kubo and Pehlke (1986), and Shivkumar et al. (1990) indicate that the cellular or dendritic interface is a much more favorable nucleation site because the interface is concave and soluble gases are concentrated in the interdendritic region.

Inclusions are probably the most important sites for heterogeneous nucleation. It has been shown that the presence of inclusions greatly enhances the porosity formation in aluminum alloys (Tiwari and Beech, 1978; Fang and Granger, 1989; Fredriksson, 1976; Ghosh and Ray, 1988; Iwahori et al., 1990; Shahani, 1985).

The easiest sites for bubble to nucleate are the preexisting gas bubbles entrapped in the cavities of the inclusions (Tiwari and Beech, 1978; Cole 1974) no nucleation event is required, only growth. Cole illustrated that one such site can act as a multiple nucleation site if the bubbles detach, leaving a small bubble behind in the cavity.

4.4.3 Pore Growth

Describing the growth of a pore is limited by a lack of good understanding of pore nucleation. For 356 alloys, (Fang and Granger, 1989) suggest that the growth of a pore can be divided into three stages. In the first stage, growth of a pore takes place in the liquid at temperatures between the liquidus and the eutectic. In the second stage, the pores grow isothermally in the eutectic liquid. In the third stage it is assumed that the liquid pools are isolated so that the solidification shrinkage of the liquid pool will add to the volume of the pores.

For directional solidification, (Lee, 1994) used an X-ray temperature gradient stage in order to track in-situ pore growth in aluminum alloys. The pore size was measured. It was suggested that the pore growth is limited by the diffusion of hydrogen and the solid phase microstructure. A coupled continuum-stochastic model was proposed for pore growth. In this study, porosity is

considered to form due to both hydrogen and shrinkage according to (Piwonka and Flemings, 1966; Kubo and Pehlke, 1985; and Shivkumar et al., 1990).

4.4.4 Microporosity Prediction Models

Attempts to predict the level of porosity in castings have included both parametric (Bishop and Pellini, 1950; Niyama et al., 1981; Lee et al., 1990; and Viswanathan et al., 1992) and "first-principles" models (Walther et al., 1956; Piwonka and Flemings, 1966; Kubo and Pehlke, 1985; Poirier et al., 1987; Zou and Doherty, 1993; Combeau et al., 1995; Barkhudarov et al., 1993; Suri and Paul, 1993). A number of other studies have also attempted to understand the phenomena of porosity formation and pore growth (Fang and Granger, 1989; Shivkumar et al., 1990; Sigworth and Wang, 1993) and pore morphology (Huang et al., 1998).

Kubo and Pehlke (1985) presented a methodology for the prediction of microporosity distribution in shaped castings. In their study, the effects of both the hydrogen precipitation during solidification and the pressure drop due to feeding resistance of the mushy zone on porosity formation are considered. The pressure drop during solidification is calculated only in the interdendritic feeding regime by using Darcy's law. The liquid feeding and mass feeding regimes are neglected. The local pressure and porosity are computed in an uncoupled manner (i.e., in which either the pressure or porosity is computed first by using the other variable at previous time step). The primary variable, either pressure or porosity, is selected based on a "flux of interdendritic liquid" criterion. If the flux of liquid is positive, then the pressure is first computed by using the porosity of previous time step. If the flux of liquid is negative, then the porosity is first computed by using the pressure at previous time step. The methodology proposed by (Kubo and Pehlke, 1985) has been used with little change in numerous studies, such as those of (Poirier et al., 1987; Combeau et al., 1993; Rousset et al., 1994).

The accuracy of pressure computation is very important for microporosity prediction. The pressure distribution in castings is affected by the liquid feeding, mass feeding, and by macroshrinkage defects such as the profile of the air-liquid metal interface in the riser, which cannot be considered by using Darcy's law as the momentum equation. More accurate fluid flow models than that used by (Kubo and Pehlke, 1985) are presented by (Zou and Doherty, 1993 and Combeau et al., 1995). The former study considers porosity only for two-dimensional cases. Without considering microporosity, the latter study includes interdendritic flow for three-dimensional simulations of mold filling. Barkhudarov, et al. (1993) suggested that the complexity of the Kubo-Pehlke method could limit its applicability to the simulation of fully three-dimensional castings. Suri and Paul (1993) extended the Kubo-Pehlke methodology to three dimensions without providing details on the coupling between microporosity and pressure.

The governing equations for fluid flow and hydrogen evolution indicate that the porosity formation and fluid flow are strongly coupled. However, in most studies on microporosity (Poirier et al., 1987; Shivkumar et al., 1990); Sigworth and Wang, 1993), it is considered that the porosity formation does not influence the fluid flow in the mushy zone. Kuznetsov and Vafai (1995) showed that neglecting the effect of porosity formation on the pressure in the mushy zone yields lower pressure drops and an under-prediction of final porosity. They also have shown that the influence of porosity formation on the pressure is larger at lower pressures in the mushy

zone. To date, no methodology has been proposed to quantify the extent of shrinkage porosity, which occurs when solidification shrinkage cannot be compensated by interdendritic fluid flow.

In this chapter, we propose a methodology to determine the extent of shrinkage porosity based on experimental evidence and thermodynamical considerations that can be integrated into a general methodology for predicting casting defects. The methodology presented is suitable for easy implementation in commonly used algorithms for fluid dynamics (SOLA and SIMPLE) in commercial and research software for the simulation of casting processes. In order to accurately model the flow field for any casting condition, the model presented for fluid dynamics includes the liquid feeding and mass feeding regimes. The methodology presented in this study for microporosity prediction allows the numerical simulation of "hydrogen" and "shrinkage" porosity by considering all the factors that contribute to microporosity formation. The methodology presented has been validated on test castings designed to capture a variety of porosity formation conditions and porosity distributions.

4.4.5 Factors that must be Considered in Microporosity Prediction Models

In order to predict microporosity defects in casting processes, all factors that contribute to microporosity formation must be considered. The following physical processes must modeled:

B. Heat transfer and alloy solidification.
C. Microstructure evolution during alloy solidification.
D. Hydrogen redistribution during solidification.
E. Interdendritic fluid flow which feeds the solidification shrinkage.
F. Microporosity growth due to the local pressure drop in the mushy zone.
G. Pore expansion in casting regions where liquid feeding alone cannot compensate for the solidification shrinkage.

The following process variables must be considered:

4 Alloy composition.
5 Hydrogen content.
6 Externally applied pressure.

4.4.6 Heat Transfer and Alloy Solidification

The energy equation that describes the heat transfer during alloy solidification appears as

$$\frac{\partial \overline{\rho h}}{\partial t} + \quad (\rho_l h_l g_l \mathbf{u}) = \quad \left(k_{eff} \quad T\right) \quad , \tag{4.4.1}$$

where

$\overline{\rho h} = g_l \rho_l h_l + g_S \rho_S h_S + g_{se}\left(\rho_{se} h_{se} - \rho_s h_s\right)$ = density weighted enthalpy,

$\mathbf{u}$	=	*intrinsic* fluid velocity,
T	=	temperature,
$k_{eff} = k_s g_s + k_l g_l$	=	effective thermal conductivity.

Subscripts *s* and *l* refers to the liquid and solid phases, respectively, while subscript *e* refers to the eutectic phases. h_s, h_L, h_g are the intrinsic enthalpies for the solid, liquid, and gas phases, respectively. By neglecting microsegregation in the solid the enthalpies are given by:

$$h_s = \int_{T_0}^{T} C_p^s dT \tag{4.4.2}$$

$$h_L = h_s + \int_{T_E}^{T} \left(C_p^L - C_p^s \right) dT + L = h_s + h_{SL} + L \tag{4.4.3}$$

where T_0 and T_E are the reference and eutectic temperature, respectively, $C_p^{\ s}$ and $C_p^{\ L}$ are the specific heat for the solid and liquid phase, respectively, and L is the latent heat for solidification.

Because we are mainly concerned with the numerical simulation of fluid dynamics of shrinkage induced flows, the convection term is neglected in the energy equation. The energy equation is solved by the use of an enthalpy formulation (Reddy et al., 1997).

4.4.7 Microstructural Parameters

In addition to the liquid and solid fractions, which are calculated from the energy equation, the dendrite cell spacing is needed to estimate pore curvature and permeability in the mushy zone. The dendrite cell spacing, d_c, can be correlated with the local solidification time, t_f, by the use of the following relationship:

$$d_c [\mu m] = A t_f^{\,b}, \tag{4.4.4}$$

where t_f is the local solidification time in seconds, and A and b are constants, which are obtained from experimental measurements of dendrite cell spacing as a function of local solidification time. For A356 aluminum alloy, the coarsening constants are determined from data published (Flemings, 1974) as

$$A = 10.2 \quad \text{and} \quad b = 1/3 \tag{4.4.5}$$

The pore radius or curvature, r, is taken to be proportional to the dendrite cell spacing through the following relationship:

$$r = g_\sigma d_c / 2 \tag{4.4.6}$$

where g_σ is a pore curvature factor and d_c is the dendritic cell spacing in the solidified equiaxed aluminum alloy. For A356 aluminum alloy, g_σ is taken to be equal to 1.

4.4.8 Permeability in the Mushy Zone

Darcy's Law relates the superficial velocity at which a fluid flows through a porous medium to the pressure gradient, by

$$\mathbf{U} = -\frac{K_S}{\mu g_L} \quad p \quad , \tag{4.4.7}$$

where K_S is the specific permeability of the sample and μ is the viscosity of the liquid.

The Kozeny-Carmen equation (Murakami and Okomoto, 1984; Poirier and Ganesan, 1992; Ocansey et al., 1994) is used to relate the alloy permeability to microstructural parameters:

$$K_s = \frac{g_l^3}{k_C S_V^2} \tag{4.4.8}$$

where g_L is the volumetric fraction of the liquid, k_C is the Kozeny-Carman constant, and S_V is the surface area of the solid per unit volume. In order to correlate permeability with g_L and S_V using the Kozeny-Carman equation, isothermal coarsening experiments were conducted on each alloy. These experimental results show that Kozeny-Carman equation with k_C=5 can be used with confidence to describe liquid permeability in the mushy zone for equiaxed solidification of aluminum alloys (see Chapter 4.3).

Additionally, we found deficiencies associated with the application of the Kozeny-Carman equation. Most solidification models assume a relationship for S_V similar to that for packed beds of spherical particles, that is

$$S_V = \frac{6(1-g_l)}{d_c} \quad . \tag{4.4.9}$$

However, S_V can be determined from stereological relationships as

$$S_V = \frac{4}{d_c} \tag{4.4.10}$$

As seen in Fig. 4.4.1 for the case when $S_V=4/d_C$, at liquid fractions larger than 0.6, permeability decreases as the liquid fraction increases. The decrease in permeability seen for liquid fractions above 0.6 is unrealistic. Therefore, the relationship $S_V=4/d_C$ is not valid at large liquid fractions (i.e., above the coherency point).

The permeability computed by the use of Eq. 4.4.9 exhibits also the same unrealistic behavior when the liquid fraction used in Eq. 4.4.9 is considered to be constant above a certain large value. In order to correct these deficiencies, S_V is calculated by taking into account the dendrite coherency point by the use of the following formula:

$$S_v = \frac{1-g_l}{1-g_l^c}\frac{4}{d_c} \quad . \tag{4.4.11}$$

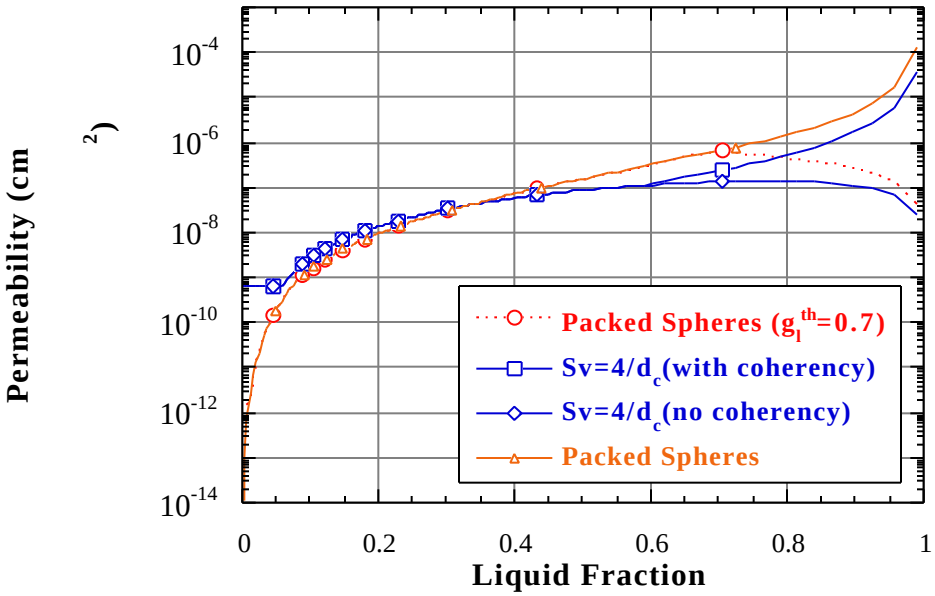

Fig. 4.4.1. Permeability function of liquid fraction.

For A356, the coherency point, g_l^c, is set to 0.6. By the use of this formula, the liquid permeability is found to increase beyond the coherency temperature. Another deficiency with the application of the Kozeny-Carman equation lies in the fact that the permeability decreases to zero as the liquid fraction decreases to zero. In order to limit the permeability to non-zero values, many studies consider that the permeability is limited by a certain threshold liquid fraction, g_l^{th}, 0.01 for example. This threshold of liquid fraction, which is used in permeability computations, is chosen arbitrarily because it is considered that the solidification microstructure evolves monotonically as shown in Fig. 4.4.2

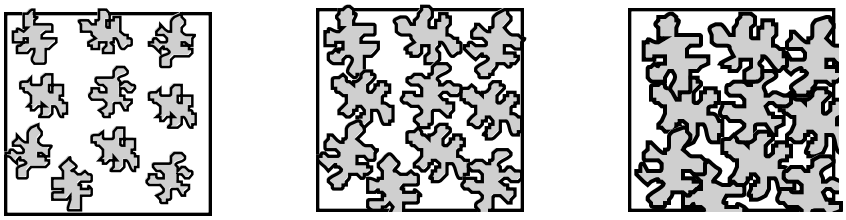

Fig. 4.4.2. Incorrect microstructure evolution model obtained when monotonic evolution of solid fraction is assumed.

However, for those alloys that exhibit eutectic reactions, the following microstructural considerations can be made. As seen from metallographic studies, the eutectic front moves as a sharp interface in the direction given by the eutectic isotherm (Fig. 4.4.3). If the back diffusion into the dendrites during the eutectic reaction is neglected, dendrites coarsen at constant volume as the eutectic front moves through them (Fig. 4.4.3). Therefore, the liquid fraction, which determines permeability for interdendritic flow that feeds the solidification shrinkage at the eutectic front, is constant during the eutectic reaction. For A356, the last eutectic reaction, which occurs during solidification, exhibits the same microstructural characteristics as that illustrated in Fig. 4.4.3. The last eutectic reaction starts at 0.05 liquid fraction. Therefore, the liquid fraction threshold for permeability computation is set at 0.05.

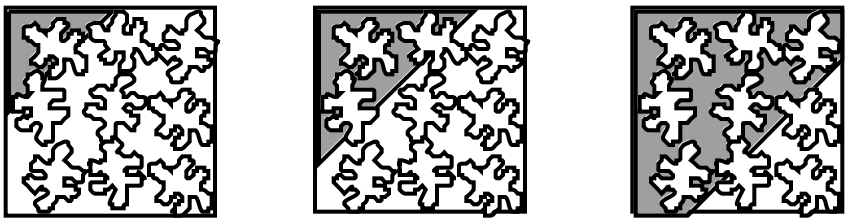

Fig. 4.4.3. Actual microstructure evolution in binary eutectic and many complex alloys considering eutectic solidification as an advancing front.

Thus, for A356 alloy the permeability is computed as follows:

$$S_v(g_l, d_c) = \begin{cases} \dfrac{4}{d_c}\dfrac{1-g_l}{1-0.6} & \text{if} \quad g_l > 0.6 \\ \dfrac{4}{d_c} & \text{if} \quad g_l \le 0.6 \end{cases}$$

$$K_s(g_l, d_c) = \begin{cases} \dfrac{g_l^3}{5S_v^2(g_l, d_c)} & \text{if} \quad g_l > 0.05 \\ \dfrac{0.05^3}{5S_v^2(0.05, d_c)} & \text{if} \quad g_l \le 0.05 \end{cases} \quad . \qquad (4.4.12)$$

In the formulas shown in Eq. 4.4.12 for the interfacial area and permeability, the coherency threshold for the liquid fraction is considered to be 0.6 while the eutectic threshold is considered to be 0.05.

Another implication of considering the microstructural evolution during the eutectic reaction for the computation of interdendritic flows involves the application of no-slip boundary conditions. Because the momentum equation holds only within the bulk liquid or mushy zone regions, boundary conditions must be prescribed for the pressure and velocity at solidified interfaces. Without explicitly tracking the solidified interfaces within computational cells, boundary conditions can simply be applied at cell faces shared between solidified cells and mushy zone cells. The no-slip boundary conditions which are applied at the face center of an interfacial face, f, appears as

$$\mathbf{u} = 0 \text{ and } \mathbf{n}_f \quad P = 0 \ , \qquad (4.4.13)$$

where $\mathbf{n}_f$ denotes the cell face normal. A cell is considered fully solidified when liquid fraction in that cell becomes less than a critical liquid fraction, g_l^f. From the physical point of view this threshold for the liquid fraction, g_l^f, represents the value of the liquid fraction, g_l^f, at which the interdendritic feeding ceases and momentum equation is no longer valid. Values for the feeding threshold, g_l^f, vary between 0.1 and 0.01 and its choice is rather arbitrary (Lee et al., 1990; Chiou and Tsai, 1990).

By considering the microstructure evolution the during eutectic solidification shown in Fig. 4.4.3, and the fact that the pressure should be computed only in regions located in the mushy zone, a value for the feeding threshold, g_l^f, can be derived from geometrical consideration. Specifically, we consider that the pressure is not computed when the eutectic front reaches the cell center, which is the location where the pressure variable is defined. As the dendrite volume fraction does not change (Fig. 4.4.3), the volumetric liquid fraction at which the region of bulk solid extends for more than half of the cell can be estimated to be half of the eutectic fraction, g_E, in that cell. For those cells in which $0<g_l<g_E/2$, the cell center becomes located inside the bulk solidified region. Because the pressure is not computed in regions of bulk solid, including those cells in which $0<g_l<g_E/2$, an estimate for g_l^f is given as

$$g_l^f = \frac{g_E}{2} \quad . \tag{4.4.14}$$

4.4.9 Hydrogen Porosity Evolution

It is commonly accepted that pores form in solidifying aluminum alloys when the equilibrium partial pressure of hydrogen corresponding to the hydrogen concentration within the liquid, exceeds the local pressure in the mushy zone by an amount necessary to overcome surface energy forces (Piwonka and Flemings,1966; Kubo and Pehlke, 1985). Thus, the condition for microporosity formation can be given in terms of a pressure condition:

$$\begin{aligned} P_g &> P_m + P_\sigma \\ P_\sigma &= \frac{2\sigma}{r}\sqrt{S_{hn}(\theta)} \quad , \end{aligned} \tag{4.4.15}$$

where P_g is the gas pressure corresponding to the gas concentration in the liquid, P_m is the local metallostatic pressure in the solidifying alloy, σ_I is the surface tension at the gas-liquid interface, and r is the pore radius. P_σ is the pressure in the pore due to the effects of surface tension. $S_{hn}(\theta)$ is a factor which takes into account the effect of heterogeneous nucleation of a bubble and depends on the contact angle, θ, of the gas-melt interface with the bubble nucleating substrate by the following relationship:

$$S_{hn}(\theta) = \left(2 + 3\cos(\theta) - \cos^3(\theta)\right)\Big/4 \ , \tag{4.4.16}$$

For most foundry practice, S_{hn} can be considered to be unity, since the molten metal has a high concentration of oxide films that serve as nucleating substrates for hydrogen bubble nucleation.

The hydrogen concentration in the liquid and the gas pressure are related through the Sievert's law:

$$C_H^l = SC_S^u\sqrt{P_g} \quad , \tag{4.4.17}$$

where S is the hydrogen solubility in the liquid in cc/100g, and C_S^u is a unit conversion factor, equal to 1 or 0.001 when P_g is computed in atm or cgs units, respectively.

Neglecting its diffusion, hydrogen evolution is described by the following mass balance:

$$f_g C_H^u = C_H^0 - C_H^l\left(f_s k_H + f_l\right) \ , \tag{4.4.18}$$

where C_H^0 is the initial gas concentration within the liquid, k_H =0.069 is the partition coefficient for hydrogen between solid and liquid, f_s and f_L are the mass fractions of solid and liquid,

respectively. It is convenient to use the initial hydrogen concentration and solubility in weight fractions rather than in their original units. The initial hydrogen concentration and solubility in weight fractions are given by the following relationships:

$$\begin{aligned} \overline{C}_H^0 &= \frac{C_H^0}{C_H^u} \\ \bar{S} &= S\frac{C_S^u}{C_H^u} \end{aligned} \quad . \tag{4.4.19}$$

The hydrogen evolution is described by the following mass balance equation:

$$f_g = \overline{C}_H^0 - \bar{S}\sqrt{P_m + P_\sigma}\left(f_s k_H + f_l\right) \quad . \tag{4.4.20}$$

The hydrogen evolution equation cannot be used directly in the above from because the shrinkage term in the continuity equation is written using volumetric fractions. By using the following density relationships between the average density within a computational element, $\bar{\rho}$, volumetric fractions and mass fractions:

$$\begin{aligned} \bar{\rho} &= g_l\rho_l + g_s\rho_s + g_{se}\left(\rho_{se} - \rho_s\right) + g_g\rho_g \\ f_g\bar{\rho} &= g_g\rho_g \\ f_l\bar{\rho} &= g_l\rho_l \\ f_s\bar{\rho} &= g_s\rho_s + g_{se}\left(\rho_{se} - \rho_s\right) \end{aligned} \quad . \tag{4.4.21}$$

Equation 4.4.22 can be derived for the hydrogen evolution in terms of volumetric fractions:

$$g_g\rho_g = \bar{\rho}\,\overline{C}_H^0 - \bar{S}\sqrt{P_m + P_\sigma}\left[\left(g_s\rho_s + g_{se}\left(\rho_{se} - \rho_s\right)\right)k_H + g_l\rho_l\right] \quad . \tag{4.4.22}$$

4.4.10 Fluid Flow

Because we are mainly concerned with the numerical simulation of fluid dynamics of shrinkage induced flows, the convection term is neglected in the energy. Although shrinkage flows are very slow, they are very important in the formation of casting defects such as macrosegregation (Krane and Incropera, 1995) and microporosity (Kubo and Pehlke, 1985). For example, the pressure drop due to shrinkage flows is one of the determining factors in microporosity formation in light alloy castings.

During solidification in alloy castings, regions of solid, mush, and bulk fluid coexist. At low solid fractions, solid nuclei are dispersed in the liquid and carried away by the liquid metal flow. This flow regime in which the alloy behaves like slurry is referred to as mass feeding. At larger solid fractions than a critical value, g_s^{cr}, referred to as the coherency limit, dendrites form a fixed network through which the liquid metal flows. g_s^{cr} are dependent on the type of alloy and dendrite morphology (Arnberg et al., 1996). This flow regime encountered above the coherency limit is called interdendritic feeding.

In order to model the mass and interdendritic feeding, the alloy volumetric fraction, g_c, and alloy density, ρ_c, which are convected by the liquid flow are tracked. The g_c and ρ_c variables are given by

$$g_c = \begin{cases} 1 \text{ if } g_s \le g_s^{cr} \text{ (mass feeding)} \\ g_l \text{ if } g_s > g_s^{cr} \text{ (interdendritic feeding)} \end{cases} \quad . \qquad (4.4.23)$$

$$\rho_c = \begin{cases} \bar{\rho} \text{ if } g_s \le g_s^{cr} \text{ (mass feeding)} \\ \rho_l \text{ if } g_s > g_s^{cr} \text{ (interdendritic feeding)} \end{cases}$$

The mass conservation equation for the *intrinsic* fluid velocity, **u**, is given by

$$\frac{\partial \bar{\rho}}{\partial t} + \nabla\cdot(\rho_c g_c \mathbf{u}) = 0 \quad , \qquad (4.4.24)$$

where $\bar{\rho} = \rho_l g_l + \rho_s g_s + g_{se}(\rho_{se} - \rho_s)$ is the averaged density of the alloy. g_s, g_L, and g_g are the volume fraction of solid, liquid, and gas, respectively. ρ_{se} and g_{se} are the density and volume fraction of the solid eutectic, respectively. The solid density, ρ_s, is usually taken to be constant while the liquid density varies with the solute concentration and temperature, $\rho_l=\rho_l(T,C_l)$. The gas density, ρ_g, varies according to the ideal gas law:

$$\rho_g = \frac{P_g}{R_{H_2} T} \quad , \qquad (4.4.25)$$

where R_{H_2} is the hydrogen gas constant.

We have to emphasize that constant liquid and solid densities are considered in most of the studies that aim at modeling shrinkage effects during solidification. It is only recently that accurate modeling of the shrinkage demand during solidification was considered by employing variable liquid and solid densities as a function of temperature and concentrations (Chang and Stefanescu, 1996; Reddy and Beckermann, 1997).

The momentum equation for the interdendritic flow can be written as

$$\rho_c \left[\frac{\partial \mathbf{u}}{\partial t} + (\mathbf{u}\cdot\nabla)\mathbf{u}\right] = -\nabla P + \mu \nabla^2 \mathbf{u} + \rho_c g - g_l C_D \mathbf{u} + \mathbf{u}\frac{\partial}{\partial t}\left((1-g_c)\rho_s\right) \quad . \qquad (4.4.26)$$

In general, the drag coefficient, C_D, which accounts for the momentum loss due to the flow around and through the dendrite structures, is a function of the velocity magnitude, $|\mathbf{u}|$, permeability,K_S, and liquid fraction, g_l. In this work, the drag coefficient, C_D, is given by the Darcy's and Forchheimer's terms, which are often referred to as the "viscous drag" and "form drag" terms (Beckermann and Viskanta, 1993):

$$C_D\left(|\mathbf{u}|, K_s, g_l\right) = \underbrace{\frac{\mu}{K_s}}_{\text{Darcy's}} + \underbrace{\frac{C_F \rho_c g_l}{\sqrt{K_s}}|\mathbf{u}|}_{\text{Forchheimer's}} \quad . \tag{4.4.27}$$

The Forchheimer's term needs to be considered when relatively high interdendritic fluid velocities are expected. We have to emphasize that most studies that consider liquid convection during solidification use the momentum equation in the form developed by (Bennon and Incropera, 1987). They simplified the momentum equation in order to avoid tracking the liquid-solid interface (Prescott et al., 1991). This simplified momentum equation can be discretized by using existing discretization techniques (Patankar, 1982) over the entire domain, irrespective of the bulk liquid, mushy, and solid regions. An analysis of their simplified momentum equation reveals that an underestimation of the convective terms is made. Indeed, by rewriting their momentum equation for the liquid velocity and comparing it with Eq. 4.4.26, it can be noticed that the convective terms in their equation are artificially weighted with the liquid fraction. For those studies in which the mass feeding is neglected, the underestimate of the convective terms is not important since they can be dropped altogether due to small shrinkage velocities. We expect that errors which are due to the underestimate of the convective term would be important in cases in which mass feeding is considered.

4.4.11 Solution Methodology

A brief outline of our methodology for the numerical simulation of microporosity defects is presented here. We consider that microporosity is composed of hydrogen porosity and contribution due to shrinkage that cannot be fed. Due to severe shrinkage effects, the computed liquid pressure in poor feeding regions can drop below the zero absolute pressure. We consider that liquid pressures lower than the cavitation pressure cannot be obtained during casting. If the pressure drops below the cavitation pressure, P_c, it is considered that liquid feeding ceases and that the solidification shrinkage in that computational cell is compensated only by pore growth. Thus, the onset of shrinkage porosity growth is given by the instant at which the pressure in the mushy zone drops below the cavitation pressure.

The flowchart of our algorithm for microporosity prediction is shown below in Fig. 4.4.4.

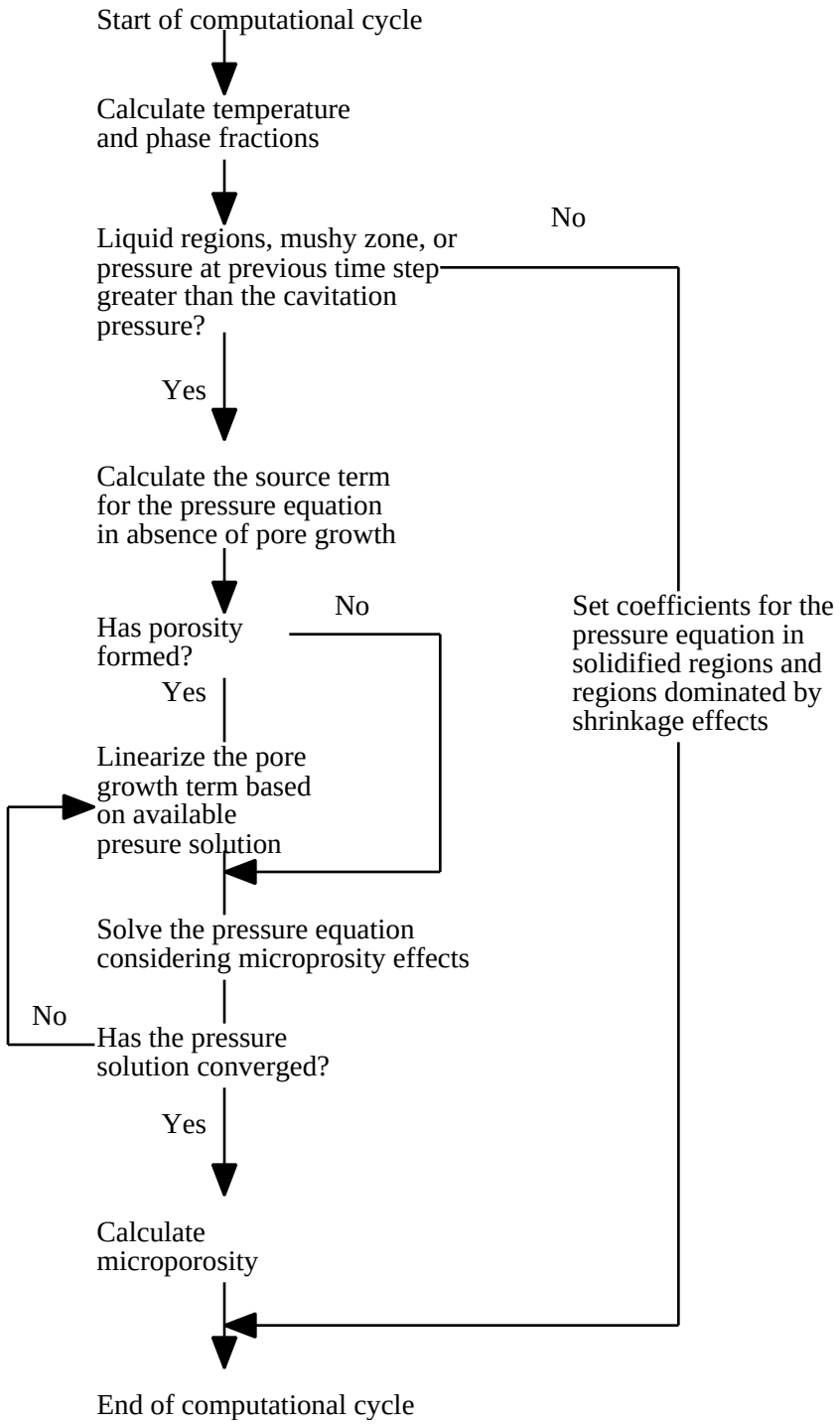

Fig. 4.4.4. Computational cycle for the microporosity algorithm.

4.4.12 Shrinkage Porosity

Due to severe shrinkage effects, the pressure computed in poor feeding regions can drop below the zero absolute pressure. We consider that liquid pressures lower than the cavitation pressure cannot be obtained during casting. If the pressure drops below the cavitation pressure, P_c, it is considered that liquid feeding ceases and that the solidification shrinkage in that computational cell is compensated only by pore growth. Indeed, if the liquid would feed the solidification shrinkage in these regions where the pressure is equal or less than the cavitation pressure, then the pressure would drop even more at lower values well below the cavitation pressure. Therefore, once the liquid pressure in a computational cell reaches the cavitation pressure, the pressure in that cell will be set to the cavitation pressure until the end of solidification.

Sievert's law cannot be used to calculate the pore fraction. Indeed, after the liquid reaches the cavitation pressure, then the gas pressure would be $P_g = P_c + P_\sigma$, and if the Sievert's law would used to compute the porosity, the porosity would grow only as P_σ reduces due to coarsening effects (Eq. 4.4.15). This pore growth due only to the effect of dendrite coarsening on P_σ does not compensate for the entire solidification shrinkage. Therefore, the Sievert's law and mass conservation equation cannot be both satisfied after the liquid reached the cavitation point. Thus, the instant at which the shrinkage porosity starts to grow is given by the instant at which the liquid pressure drops below the cavitation pressure.

In cavitated regions in the mushy zone (i.e., where the liquid pressure dropped below the cavitation pressure at previous iterations), the porosity is determined such that it compensates for the entire solidification shrinkage within the current time step:

$$g_g^{n+1} = g_g^n + \left(1 - g_g^n\right)\left(1 - \frac{\bar{\rho}^n}{\bar{\rho}^{*n+1}}\right) \quad , \tag{4.4.28}$$

Because no feeding is considered to take place in computational cells in which the pressure has reached the cavitation pressure, these cells are treated as solidified cells when the pressure is computed. Also, the pressure equation is subject to Neumann boundary conditions (Eq. 4.4.13) at interfaces between mushy zone and cavitated regions.

4.4.13 Solution Algorithm for Interdendritic Flow and Microporosity

In order to accurately predict microporosity, a solution algorithm for interdendritic flows in which the coupling between pore growth and liquid feeding is treated implicitly is used in this study. The solution algorithm for interdendritic flows is based on a variable projection method and is extended in this study to include the effect of microporosity on the interdendritic flow. In this methodology, the energy and microporosity equations are uncoupled. The energy equation is solved by using the hydrogen gas fraction at the previous time level, g_g^n, without considering the effect of pore growth within the current time step. $\bar{\rho}^{*n+1} = \rho_l^n g_l^{*n+1} + \rho_s g_s^{*n+1} + g_{se}^{*n+1}\left(\rho_{se} - \rho_s\right)$ is the density which is estimated based on volumetric fractions g_l^{*n+1} and g_s^{*n+1} computed from the energy equation.

An intermediate velocity, **u***, is computed from the momentum equation as:

$$\rho_C \left[\frac{\mathbf{u}^* - \mathbf{u}^n}{\Delta t} + \mathbf{u}\,\nabla\mathbf{u}\right] = \mu\,\nabla^2\mathbf{u}^n + \rho_C\mathbf{g} - \rho_s\frac{\partial g_C}{\partial t}\mathbf{u}^n - g_l C_D\left(|\mathbf{u}^n|, K_S, g_l\right)\mathbf{u}^* \quad . \tag{4.4.29}$$

When microporosity is present, the projection step is comprised of the following update of the pressure and velocity:

$$\left(\sigma_p^{*n+1} \quad P^{n+1}\right) = RHS_0 + \left(\frac{\bar{\rho}^{*n+1}}{\Delta t^2} - 3RHS_0\frac{g_g^n - g_g^{n+1}}{1 - g_g^n}\right) \quad , \tag{4.4.30}$$

$$g_c^n \rho_c^n \frac{\mathbf{u}^{n+1} - \mathbf{u}^*}{\Delta t} = -\nabla\sigma_p^{*n+1} \quad P^{n+1} \quad . \tag{4.4.31}$$

where the projection variable and the RHS_0 term are given by

$$\sigma_p^{*n+1} = \frac{g_C}{1 + g_l C_D \Delta t / \rho_C}, \text{ and } RHS_0 = \frac{1}{\Delta t}\left[\frac{\bar{\rho}^{*n+1} - \bar{\rho}^n}{\Delta t} + \nabla\left(\rho_c^n g_c^n \mathbf{u}^*\right)\right] . \tag{4.4.32}$$

In the above pressure relationships, the drag term and projection variable are computed using the liquid fraction g_l^{*n+1} which was computed from the energy equation.

Equation 4.4.22 is used to relate the last term in Eq. 4.4.30 with the pressure. In order to take microporosity effects on the interdendritic flow into account, the last term in Eq. 4.4.30 is linearized and the pressure equation is solved iteratively.

4.4.14 Microporosity Results for Plate Casting

In order to capture the wide range of solidification conditions encountered in sand and permanent mold castings, plate castings were made in a variety of mold configurations. Of those, two castings are of particular interest to this study. They include plates cast in a sand mold and in a sand mold with top, bottom, and end chills. The cast plate dimensions and chill plate configuration are shown in Fig. 4.4.5. The top and bottom chill dimensions are nominally 200, 150, and 25 mm (8.125, 6, and 1 in). The end chill dimensions are nominally 60, 60, and 150 mm (2.5, 2.5, and 6 in). All the plates were contained in a sand mold with nominal dimensions of 600, 210, and 200 mm (25, 8.5, and 8.125 in), respectively.

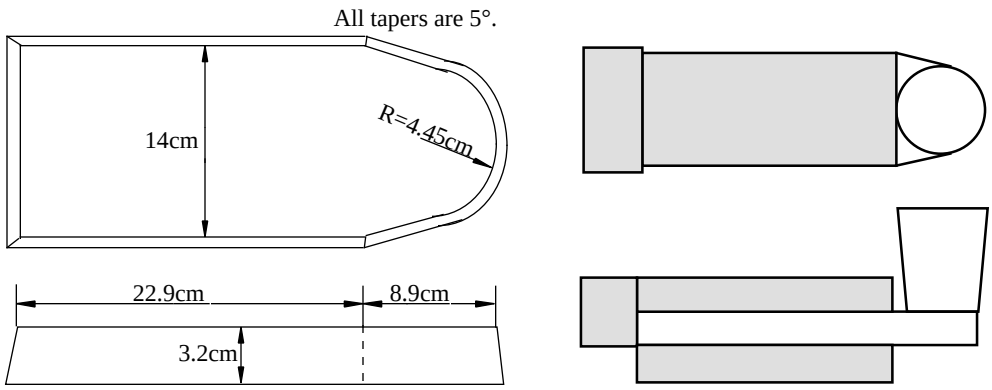

Fig. 4.4.5. Plate dimensions and chill plate configuration.

Due to the symmetry along the vertical section through the plate center, the problem was solved only on half of the plate.

Numerical simulation results are presented for A356 alloy sand and chill plate castings. The alloy was poured at 720˚C (1328 F). The mold-filling phase was neglected in computations, and the initial temperature of the alloy was considered to be uniform over the entire casting. Thermophysical property data were based on experimental measurements and/or data available in the literature.

Figure 4.4.6 shows the liquid volume fraction distribution for the sand plate and the chill plate, 700 s and 30 s from the onset of solidification. In both plates, solidification progresses from the end of the plate toward the riser without forming any hot spots. In the sand plate, the liquid volume fraction varies from 0 at the end of the plate to 0.7 in the riser [Fig. 4.4.6(*a*)]. Although the entire casting is mushy, feeding channels are relatively open as the liquid fraction adjacent to the end of the plate is around 0.5. In the chill plate, solidification occurs in the form of a channel that exists over the entire length of the plate [Fig. 4.4.6(*b*)].

Figure 4.4.7 shows the experimentally determined porosity distribution in the sand and chill plates (Dighe et al., 1999). The porosity level in the sand plate is fairly uniform over the plate, and approximately 0.5%. The porosity level in the chill plate, on the other hand, exhibits a maximum at the center of the plate, and this maximum is three times the porosity level in the sand plate.

Figure 4.4.8 illustrates the pore morphology in two regions of the chill plate. In regions close to the end of the plate and close to the riser, the pores are small and rounded, and are approximately the same size as the local dendrite cell spacing [Fig. 4.4.8(*a*)]. In the middle of the plate corresponding to the maximum in porosity, the pores are large, irregular, and conform to the morphology of the interdendritic region [Fig. 4.4.8(*b*)]. The pore morphology in the entire sand plate was similar to that in Fig. 4.4.8(*a*). In foundry terminology, the pore in Fig. 4.4.8(*a*) is considered to be hydrogen porosity, while the pores in Fig. 4.4.8(*b*) are considered to be shrinkage porosity.

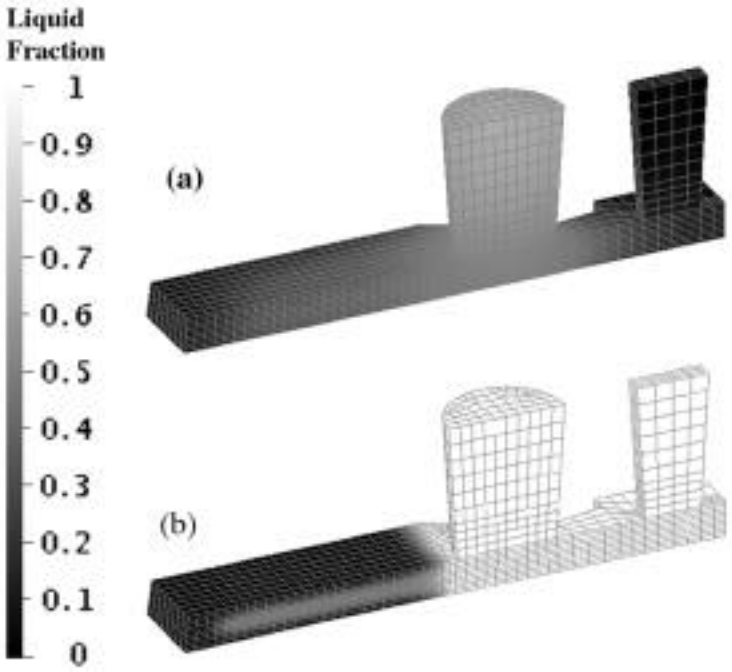

Fig. 4.4.6. Liquid fraction distribution for *(a)* sand plate at 700 s and *(b*) chill plate at 30 s from the onset of solidification.

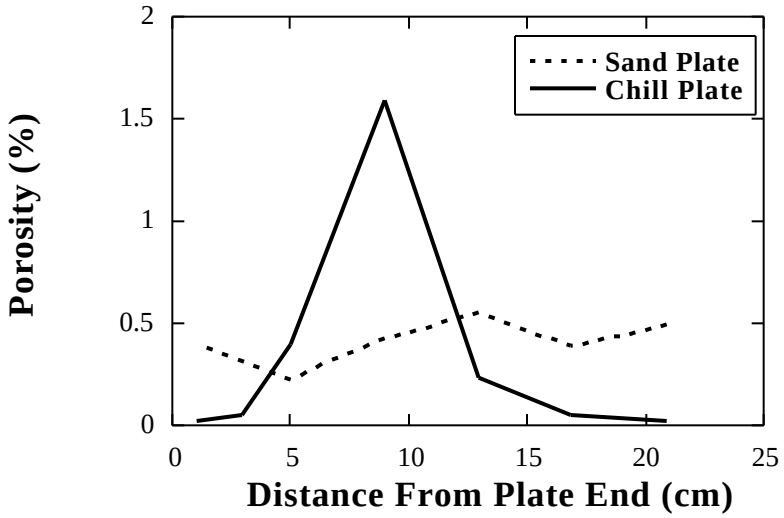

Fig. 4.4.7. Experimentally measured distributions of pore fraction in the sand and chill plates (Dighe et al., 1999).

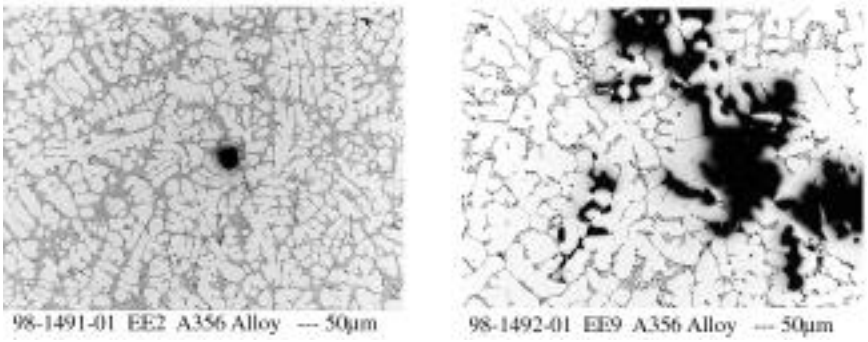

(*a*) (*b*)

Fig. 4.4.8. Pore morphologies along the centerline of the chill plate casting at locations near the (*a*) plate end (*b*) plate center.

In Fig. 4.4.9, the evolution of the local pressure in two computational cells is shown as a function of liquid fraction for the chill plate. The cells are located along the center of the plate near the end and the middle of the plate. For these two cells considered the porosity distributions correspond to those shown in Figs. 4.4.8(*a* and *b*). In regions characterized by hydrogen porosity, the pressure drops to low levels toward the end of solidification, while in regions where shrinkage porosity is observed experimentally, a severe pressure drop occurs relatively early in the solidification (i.e., at a liquid fraction of 0.5).

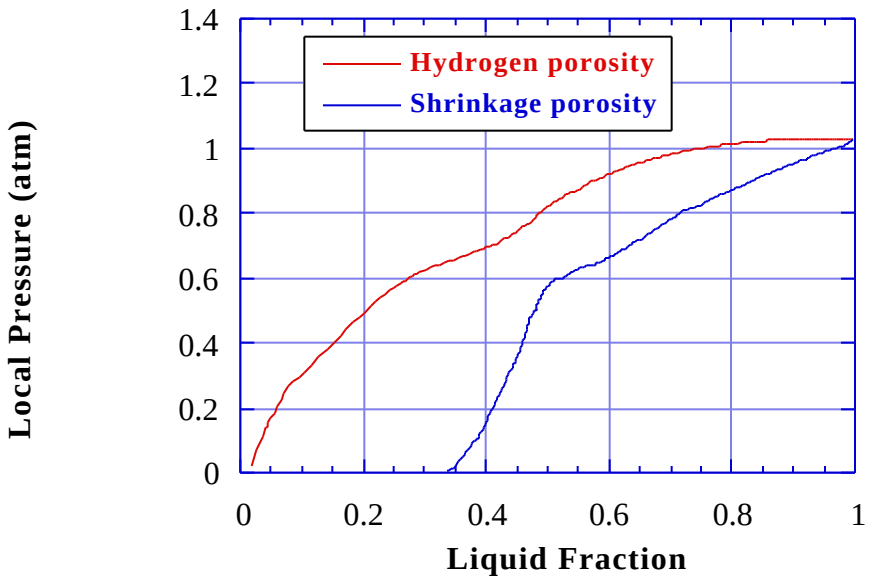

Fig. 4.4.9. The evolution pressure in two computational cells that exhibit hydrogen and shrinkage porosity.

The appearance of “hydrogen” and “shrinkage” porosity regions can be explained by considering the evolution of the interdendritic liquid pressure during solidification. As the partial pressure of hydrogen, which corresponds to the hydrogen concentration within the liquid, overcomes the local liquid pressure and surface energy forces, hydrogen porosity nucleates. Immediately

following their nucleation, hydrogen pores expand into spherical bubbles that occupy a region between dendrite cells (or between grains). Since this occurs toward the end of solidification, there is little further pore growth, and the final pore size upon solidification is proportional to the local dendrite cell spacing. In regions of inadequate feeding, a severe pressure drop occurs early in solidification, yielding hydrogen bubble nucleation earlier in solidification. As solidification proceeds, there is further demand for feed metal, but since the resistance to liquid flow is high, the amount of feeding liquid is insufficient to compensate for the entire shrinkage. In this instance, the spherical hydrogen pores expand into the irregular interdendritic region as solidification progresses, to compensate for solidification shrinkage. Thus, the categorization of pores based on their shapes as "hydrogen" and "shrinkage" as a result of interdendritic liquid feeding is actually quite accurate. In the chill plate, both types of porosity are present as the plate contains regions of both good and poor feeding. In the sand plate, the pore morphology at all locations along the plate corresponds to that of hydrogen porosity, as solidification is slow and progressive and no regions of excessive metal demand are encountered.

Figure 4.4.10 shows calculated microporosity distributions for the sand and chill plates. The experimentally measured values are also shown for comparison. The agreement for the sand plate is quite good. In the case of the chill plate, the model correctly predicts the maximum in porosity near the center of the plate. However, the predicted minimum porosity is higher, the predicted maximum porosity is lower, and the peak in the distribution is broader than in the experimental results. These differences between the computed results and experimental results are attributed to the following factors:

- Uncertainties in the density values used for the liquid phase, especially in the region of the final ternary eutectic.
- Using the solubility of hydrogen for the binary system instead of that for the actual commercial alloy A356.
- Using a simplifying expression for computing the pore radius.
- Neglecting the effects of pore migration during solidification (Han and Viswanathan, 1999).

4.4.15 Summary and Conclusions

A methodology to determine the extent of gas and shrinkage porosity based on thermodynamic considerations and experimental evidence is proposed. The solution algorithm presented includes a fully coupled, implicit treatment of local pressure and microporosity evolution in the mushy zone.

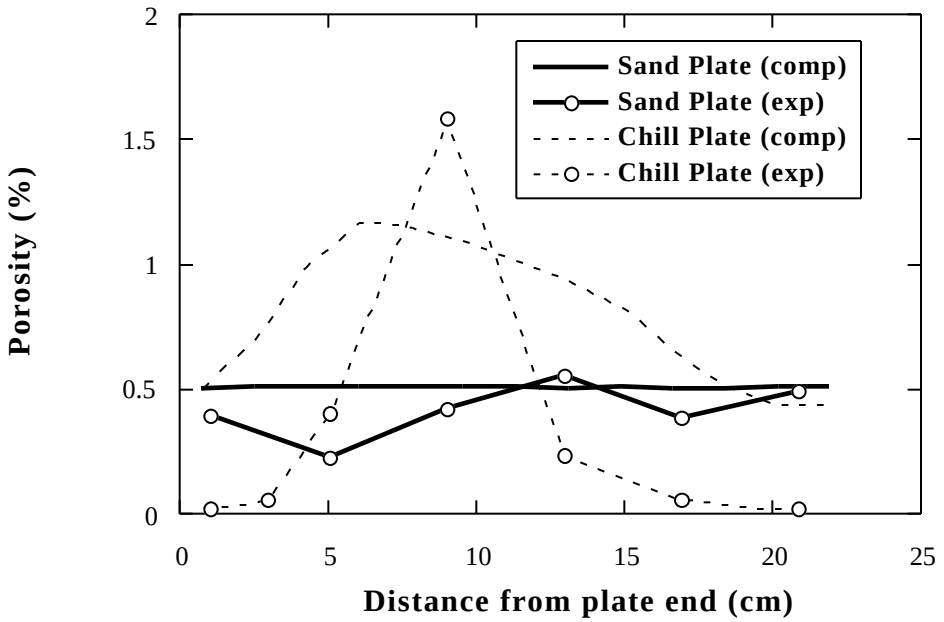

Fig. 4.4.10. Comparison of experimentally measured and computed porosity distributions along the center of the sand and chill plates.

The methodology presented takes into account alloy solidification, shrinkage-driven interdendritic fluid flow, hydrogen precipitation, and porosity evolution during solidification. Microporosity growth is due to the local pressure drop in the mushy zone and pore expansion in casting regions where liquid feeding alone cannot compensate for solidification shrinkage. The solution algorithm presented has been implemented in a computational framework consistent with those of commercial casting codes.

The methodology presented has been validated on test castings designed to exhibit both hydrogen and shrinkage porosity. The numerical results reproduce the characteristic microporosity profiles observed in the experimental results and also agree quantitatively with the experimentally measured porosity levels. The quantitative prediction of porosity levels in production shaped castings provides an enhanced capability for the design of structural safety critical castings.

4.5 MODELING OF MICROSTRUCTURE IN A356 ALLOY CASTINGS

The mechanical properties of cast aluminum alloys are largely dependent upon the solidification microstructure of the alloys. The service life of a cast component is determined by the microstructural distribution throughout the casting, especially in those regions that are critically stressed. In the drive toward lightweight vehicle production, the description and prediction of the microstructure in shape castings has become important. This is because the microstructure length scales are required in the mechanical property models used for design optimization. The use of predictive property models are critical due to the need to replace heavy ferrous parts with aluminum alloy castings and the limited experience base in the use and long term performance of aluminum alloy castings. This report focuses on the description and prediction of the solidification microstructure in A356 aluminum alloys used in structural automotive and aerospace components.

The development of the solidification microstructure in A356 aluminum alloys is well documented in the literature (Bäckerud, Chai, and Tamminen, 1990; Arnberg, Bäckerud, and Chai, 1996). On cooling, aluminum-rich dendrites first precipitate from the melt. A eutectic constituent, comprising of aluminum-rich and silicon phases, then grows between the aluminum-rich dendritic network. The morphology of the silicon phase is either rod-like or plate-like depending on whether the melt has been treated with modifiers such as sodium or strontium. On a two dimensional metallographic section, the silicon rods look like particles and the silicon plates look like rods.

The typical solidification microstructure of A356 alloy is illustrated in Fig. 4.5.1(*a*). An aluminum grain consists of six primary dendrite arms, of which four can be seen in grain *A* shown in Fig. 4.5.1(*a*) and the other two are perpendicular to the plane of the micrograph. A primary dendrite arm contains of a number of secondary dendrite arms that are almost perpendicular to the primary dendrite arm. The silicon phase is distributed randomly in the eutectic region as small particles shown in Fig. 4.5.1(*b*). As shown in Fig. 4.5.2, in order to describe the morphology of the primary aluminum-rich phase, we need the primary dendrite size (or spacing), d_1, secondary dendrite arm spacing, d_2, and dendrite cell spacing, d_C. The dendrite cell spacing is defined as the average length intersecting dendrites using random lines. d_C is a useful parameter as it can be conveniently measured by image analysis techniques. To describe the morphology of the silicon phase, we need parameters such as the silicon rod/particle diameter, *a*, silicon spacing,λ, and silicon rod length, *l*.

In the following sections of this report, models for the prediction of each of the microstrucural parameters, d_1, d_2, d_C,, l, λ and a, are described in detail. Analytical equations for each of these parameters are either derived or obtained from the literature. Predictions of the microstructural parameters and validation of the predictions in shape castings are given in Section 4.5.6.

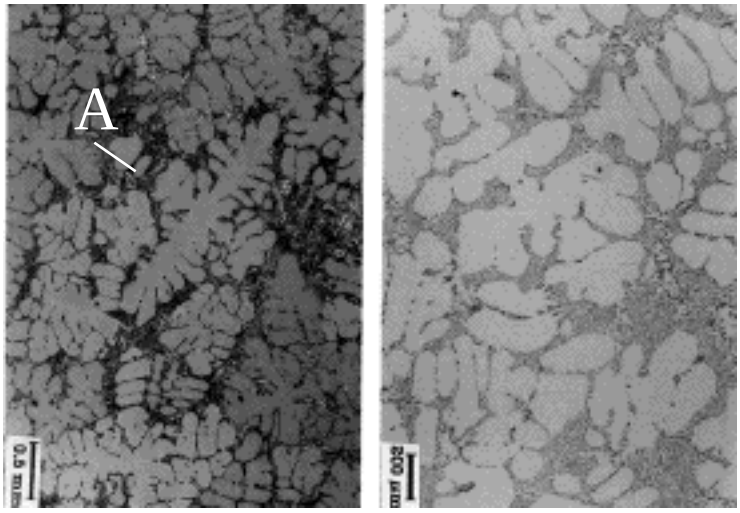

(*a*) (*b*)

Fig. 4.5.1. Typical microstructure in A356 alloy castings, consisting of equiaxed primary aluminum-rich dendrites (grain A) and an aluminum-silicon eutectic (Bäckerud, Chai and Tamminen, 1990).

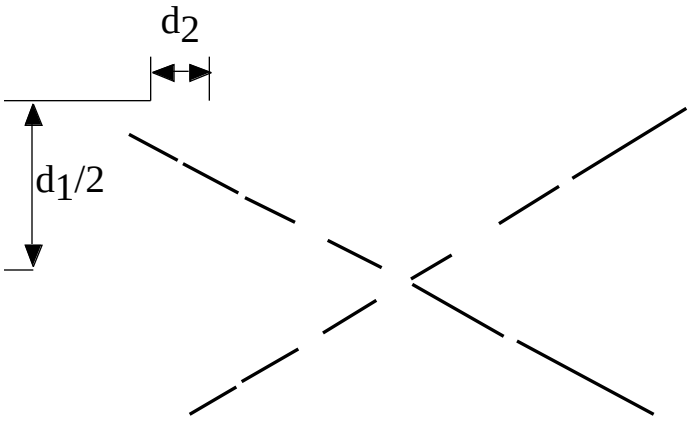

Fig. 4.5.2. Schematic diagram showing the length scales needed to describe the morphology of aluminum-rich dendrites.

4.5.1 Prediction of Primary Dendrite Spacing (Size)

The primary dendrite model for A356 alloy developed at ORNL is based on a recently successful model reported by Hunt and co-workers (Hunt, 1991; Lu and Hunt, 1992; Lu, Hunt, Gilgien and Kurz, 1994; Hunt and Lu, 1996) for dendrite array growth in binary alloys. Although the model describes the physics of dendritic array growth under directional solidification conditions, it is likely that the prediction can be extended to treat primary dendrite size during equiaxed grain growth. This is because in the case of equiaxed grains, the competitive growth of the dendrites at the liquidus isotherm is identical to that during directional solidification.

4.5.1.1 The Model

A three dimensional model has been developed for treating primary dendritic array growth in multi-component alloys by (Han and Hunt, 1997). In the model, solute transport is assumed to occur by diffusion in the liquid. The diffusion of the *i*th solute in the liquid

$$\frac{\partial C_i}{\partial t} = D_i \quad ^2 C_i \qquad i = 1, N \tag{4.5.1}$$

is solved with the usual far field conditions

$$C_i = C_{0i} \qquad at \qquad x = \infty \qquad i = 1, N \tag{4.5.2}$$

and the interface flux equations

$$V_n (k_i - 1) C_i = D_i \frac{\partial C_i}{\partial n} \qquad i = 1, N \quad . \tag{4.5.3}$$

Heat flow is included by imposing a moving linear temperature field that varies only in the axial direction,

$$T = T_I + G(x - Vt) \quad . \tag{4.5.4}$$

The composition and the temperature are coupled at the dendrite interface using the interface temperature equation given by

$$T_I = T_0 + \sum_{i=1}^{N} m_i (C_i - C_{0i}) - \Gamma(\zeta \frac{1}{R_1} + \frac{1}{R_2}) \quad , \tag{4.5.5}$$

where ζ =1-15E_4cos(4θ) is the term which allows for anisotropy. The diffusion equation is solved considering the accumulation of a solute in a control volume. The control volume box walls are orthogonal and are arranged such that the solid-liquid interface goes through the diagonal corners of an interface box (Hunt, 1991). The shape of the solid at a dendrite tip is calculated by perturbing every box corner on the solid-liquid interface to satisfy Eqs. 4.5.1 and 4.5.3 through 4.5.5. Thus, the shape of the solid-liquid interface is a result of calculation and is not assumed a priori.

4.5.1.2 Spacing Selection

The primary dendrite spacing/size in a dendrite array is defined by the interaction between neighboring dendrites. Experimentally, it has been observed that when the dendrite spacing is smaller than a minimum stable spacing, overgrowth takes place as shown in Fig. 4.5.3(*a*). This means that any dendrite having a spacing/size smaller than the stable spacing cannot survive. When the dendrite spacing is larger than the maximum spacing, a tertiary arm can grow into a primary dendrite [Fig. 4.5.3(*c*)]. As a result, the maximum stable spacing should be at least two times larger than the minimum stable spacing (Lu and Hunt, 1992), as otherwise the small

tertiary arm cannot grow into a primary dendrite arm. The average spacing lies between the minimum spacing and the maximum spacing.

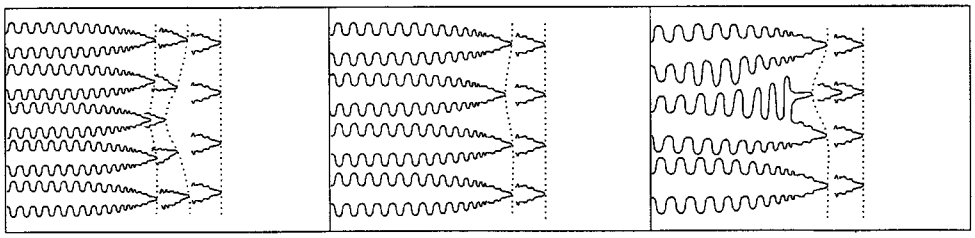

(a) Overgrowth (b) Stable (c) Growth of tertiary arm

Fig. 4.5.3. Schematic illustration of spacing adjustment observed in experiments (Lu and Hunt, 1992).

The overgrowth condition has been considered by Hunt and co-workers (Lu and Hunt, 1992; Hunt and Lu, 1996; Han and Hunt, 1997) to determine the minimum stable spacing. The mechanism for the spacing selection considering the overgrowth condition is illustrated in Fig. 4.5.4(*a* and *b*). For very narrow dendrites, solute is transported from ahead of a slightly larger dendrite to a smaller adjacent dendrite [see Fig. 4.5.4(*a*)]. If the distribution coefficient is smaller than 1, the smaller dendrite drops back and thus gets narrower, making the growth of that dendrite more difficult. As a result, overgrowth eventually occurs. For a wide enough dendrite, solute diffusion is in the opposite direction [see Fig. 4.5.4(*b*)]. This means that the smaller dendrite moves forward and eventually grows wider so that the spacing again becomes uniform. The spacing at which overgrowth starts to occur is taken to be the minimum stable spacing.

For multicomponent alloys, some of the solute elements may be rejected and others may be trapped by the growing dendrites. Thus, the solute flux across the dendrite boundary for all the solute elements needs to be considered. In this case the liquidus temperature of the alloy is used for determining the overgrowth condition (Han and Hunt, 1997). If the diffusion of the elements results in a decrease in the liquidus temperature of the smaller dendrite, overgrowth takes place.

The spacing selection mechanism is included in the numerical code in the following way. After the shape of the solid-liquid interface is obtained by solving Eqs. 4.5.1 through 4.5.5, the spacing is either increased or decreased, searching for the condition that $\partial T_m/\partial d_1$ changes sign at the dendrite boundary. The corresponding spacing is taken as the minimum spacing.

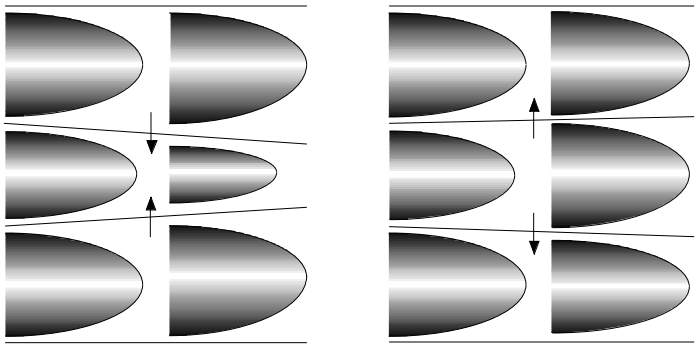

Fig. 4.5.4. Schematic illustration of the mechanism of spacing selection for the overgrowth condition.

4.5.1.3 Comparison with Data in the Literature

Comparison of the model's predictions with data from the literature for Al-Si-Mg alloys is shown in Fig. 4.5.5. The solid line in Fig. 4.5.5 is the minimum stable spacing, predicted by the model and the dashed line is the maximum spacing taken as three times the minimum spacing (Wan, Han, and Hunt, 1997). The open circles are the experimentally measured average spacing taken from the data in the literature (McCartney and Hunt, 1981). As expected, the measured average spacing falls into a band defined by the calculated minimum stable spacing and the maximum stable spacing for silicon varying from 0.3 to 7 at. % and for magnesium varying from 0.14 to 2.25 at. %.

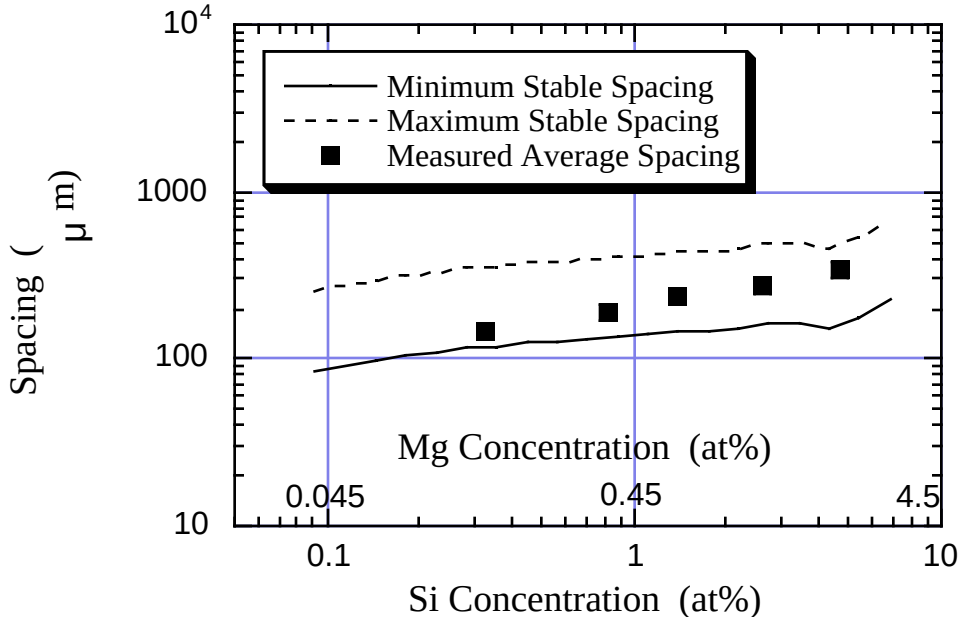

Fig. 4.5.5. A comparison of calculated and experimental results for primary dendrite spacing for Al-Si-Mg alloys (Han and Hunt, 1997).

Comparison of the model's prediction with experimental measurements on transparent materials (Huang, Geng, and Zhou, 1993) is shown in Fig. 4.5.6. Overgrowth was observed for conditions represented by the open circles. The resulting spacing is smaller than the calculated minimum stable spacing represented by the solid line. Tertiary arms were observed to grow into primary dendrites for conditions represented by the open triangles. The resulting spacing appears to be slightly larger than the maximum stable spacing. An interesting result is that the average spacing (represented by the filled circles and triangles in Fig. 4.5.6) appears to depend on the history of the specimen. If the growth velocity, *V*, is suddenly decreased during the experiment, the resulting average spacing is almost equal to the predicted minimum stable spacing. This observation indicates that, in a casting, the average primary dendrite spacing is likely to be the minimum stable spacing, since the growth velocity of the solid decreases from the surface to the center of a casting.

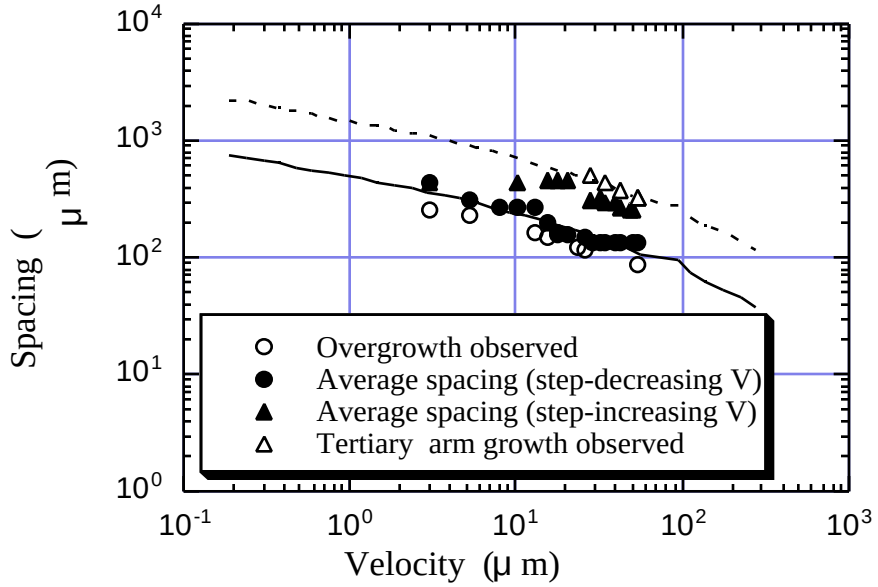

Fig. 4.5.6. A comparison of the predicted and the experimental primary spacing for succinonitrile ethanol alloys. The predicted minimum and maximum stable spacings are represented by the solid and the dashed line respectively (Hunt and Lu, 1996).

4.5.1.4 Analytical Expressions

Having validated the model's predictions, the model can be used to predict primary dendrite spacings under various casting conditions for A356 alloys. Data used in the calculation for A356 alloys are listed in the nomenclature. Figure 4.5.7 shows the calculated primary dendrite spacing at various temperature gradients and growth velocities covering a large range of casting conditions. Figure 4.5.7 represents a family of primary dendrite spacing versus growth velocity curves obtained by varying the temperature gradient at the dendrite tips. One characteristic of these curves is that one curve can be reproduced by another by simply translating the second curve. This suggests that all the curves can be compressed into one. Multiplying the d_1 value by $(G/G_0)^{0.63}$ and the V value by $(G/G_0)^{-0.67}$ for each point in each curve, where G_0 is taken as 10000 K/m, we obtain a single curve in Fig. 4.5.8 for all the data in Fig. 4.5.7. As indicated in

the literature, the minimum stable spacing is governed by the interaction of the neighboring dendrites at low growth rates and by the Peclect number at high growth rates (Hunt and Lu, 1996; Wan, Han, and Hunt, 1997). Consequently, it is better to fit the curve in Fig. 4.5.8 using two functions. For $V(G/G_0)^{-0.67}<10^{-3}$, the equation that best fits the data is

$$d_1 = 70.73V^{-0.42}G^{-0.35} \quad . \tag{4.5.6}$$

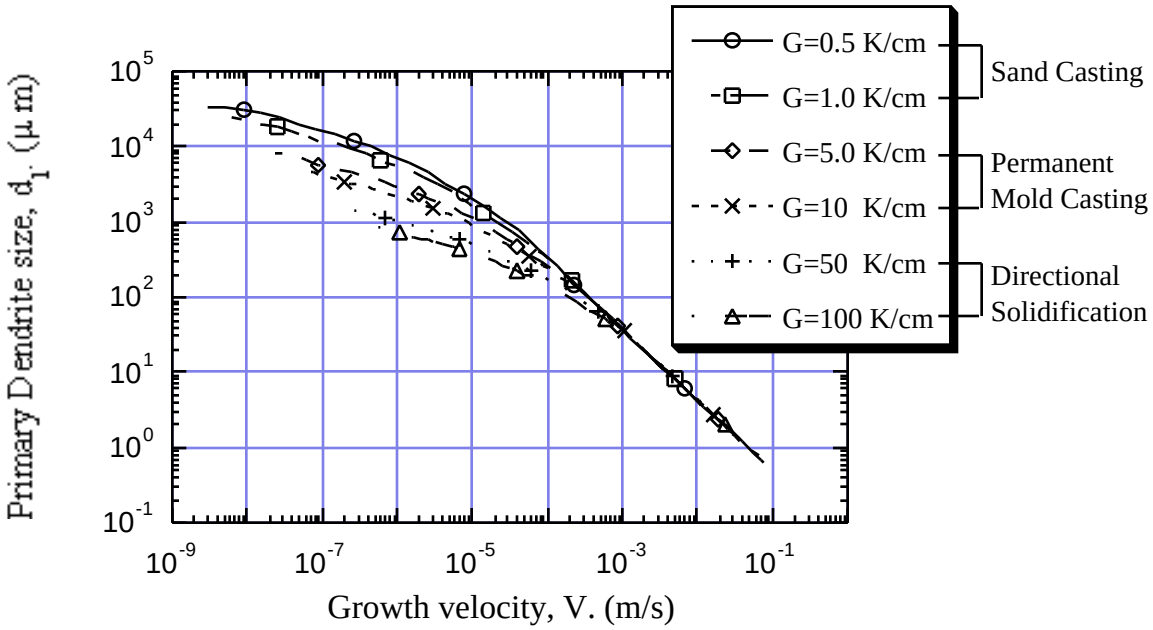

Fig. 4.5.7. Relationship between the primary dendrite arm spacing and growth velocity for a range of casting conditions.

While for $V(G/G_0)^{-0.67} >10^{-3}$, d_1 is only a function of V and is given by

$$d_1 = 0.0576V^{-0.94} \quad . \tag{4.5.7}$$

Equations 4.5.6 and 4.5.7 can be used to predict the primary dendrite size in A356 alloys for most casting conditions.

4.5.2 Secondary Dendrite Arm Spacing

During solidification, larger secondary dendrite arms grow and smaller secondary arms remelt, a process similar to Oswald ripening due to the minimization of surface energy in the system. Four geometric models (Kattamis, Coughlin, and Flemings, 1967; Reeves and Kattamis, 1971; Chen and Kattamis, 1970; Kurz and Fisher, 1989) proposed in the literature for the isothermal

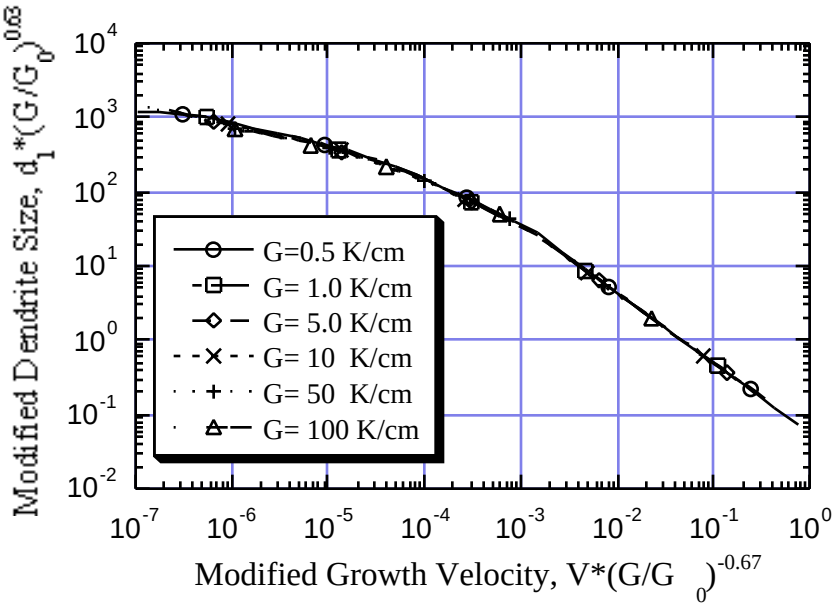

Fig. 4.5.8. A single curve generated for all the data in Fig. 4.5.7 by a mathematical transformation.

coarsening of secondary dendrite arms are shown in Fig. 4.5.9. Figure 4.5.9(*a*) illustrates Model I, a radial remelt model; Figure 4.5.9(*b*) illustrates Model II, a neck remelt model; Figure 4.5.9(*c*) illustrates Model III, an axial remelt model; and Figure 4.5.9(*d*) illustrates Model IV, a coalescence model.

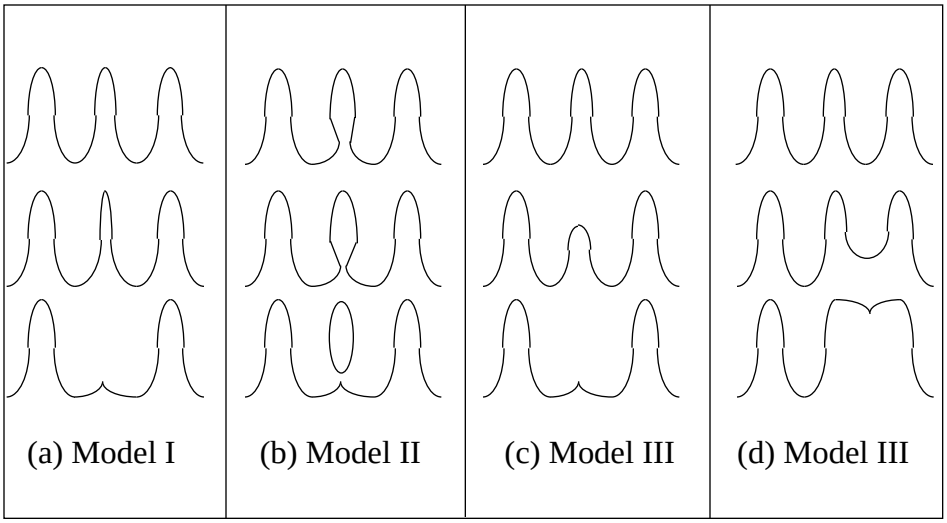

Fig. 4.5.9. Geometric models for dendrite coarsening: *(a)* radial remelt model, Model I, *(b)* neck remelt model, Model II, *(c)* axial model, Model III, and *(d)* coalescence model, Model IV.

The diffusional transport conditions that correspond to the geometric models in Fig. 4.5.9 are shown in Fig. 4.5.10(*a* and *b*). A large secondary arm has a high equilibrium liquidus

temperature and a small arm has a low equilibrium liquidus temperature due to the effect of capillarity. Given a local temperature T_1, the equilibrium solute concentration in the liquid near the large arm will be higher than that near the small one. Thus, solute will diffuse from the large arm to the small one, resulting in a reduction of the equilibrium liquidus temperature of the small arm and consequently, the melting of the small arm.

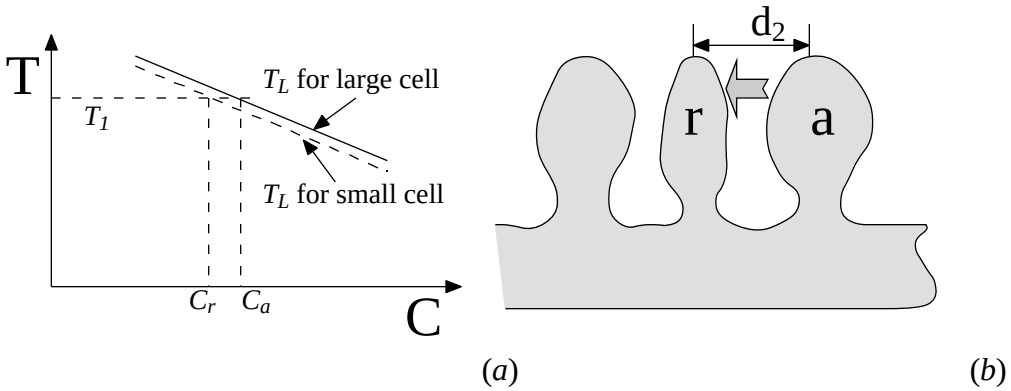

Fig. 4.5.10. Schematic diagram illustrating the mechanism of secondary dendrite arm coarsening where T_1 is the local temperature.

Based on the geometric models and the diffusional transport mechanisms for secondary dendrite arm coarsening discussed above, mathematical models have been developed for predicting the secondary dendrite arm spacing in binary alloys (Kattamis, Coughlin, and Flemings, 1967; Reeves and Kattamis, 1971; Chen and Kattamis, 1970). These models can be extended to treat multicomponent alloys (Han, Hu, and Zhong, 1997) such as A356 alloy. As shown in Fig. 4.5.10(*a*), the solute concentration difference between two dendrite arms of radii *a* and *r* is given by

$$[m]\cdot[C_a - C_r] = \frac{\sigma T_0}{L}\left(\frac{1}{a} - \frac{1}{r}\right) \quad , \tag{4.5.8}$$

where square brackets, [ ], denote a matrix and [C_a-C_r] is the composition difference matrix for multi-component alloys (Han, Hu, and Zhong, 1997). The right side of the equation contains the terms indicating the melting temperature difference of the two secondary dendrite arms due to the Gibbs-Thomson effect and [*m*] is the vector of liquidus slopes.

Solute diffuses from the larger arm to the small arm and the solute flux is given by

$$[D]\cdot[C_a - C_r]\frac{1}{d_2} = \frac{dr}{dt}[C_r(1-k)] \quad . \tag{4.5.9}$$

The right side of the equation is the flux required for the melting of the smaller arm as the result of the solute diffusion. Solving Eqs. 4.5.8 and 4.5.9 yields (Han, Hu, and Zhong, 1997)

$$t_C = -\frac{Ld_2^3}{\sigma T_0}[m][D]^{-1}[C_r(1-k)]\phi \quad , \tag{4.5.10}$$

where ϕ is a constant depending on the geometric model used (Kattamis, Coughlin, and Flemings, 1967; Reeves and Kattamis, 1971; Chen and Kattamis, 1970). For multicomponent alloys in which the interaction between the solute elements is small, $D_{ij(i\neq j)}\approx 0$ and Eq. 4.5.10 reduces to

$$t_C = \frac{Ld_2^3}{\sigma T_0}\phi \sum_{i=1}^{N} \frac{m_i C_{ri}(1-k_i)}{D_{ii}} \quad . \tag{4.5.11}$$

For binary alloys, N=1 and Eq. 4.5.11 reduces to the well known equations given in the literature (Kattamis, Coughlin, and Flemings, 1967; Reeves and Kattamis, 1971; Chen and Kattamis, 1970).

Comparison of the secondary dendrite arm spacing prediction using Eq. 4.5.11 and experimental measurements in the literature (Mori, Ogi, and Matsuda, 1976) is given in Fig. 4.5.11. All the four geometric models predict the right trend of the dependence of d_2 on composition. This suggests that the relationship between the secondary dendrite arm spacing and composition can be described using Eq. 4.5.11 for multicomponent alloys. Model II seems to fit the measurements better than Models I, III, and IV. Since Eq. 4.5.11 is derived considering diffusion only but experiments were carried out under conditions under which fluid flow in the liquid is inevitable, it is likely that Model II predominates in the presence of fluid flow. However, since all four models have been observed during experiment, one cannot claim that Model II represents the primary mechanism for secondary dendrite arm coarsening. For the purpose of this effort, however, the value of ϕ=0.00852 corresponding to Model II is suggested for the prediction of d_2 under casting conditions.

Using Eq. 4.5.11 for Al-Si-Mg ternary alloys corresponding to the composition of A356, we have

$$t_C = -d_2^3 \frac{L\phi}{\sigma T_m}\left(\frac{m_{Si}C_{Si}(1-k_{Si})(1-f_s)^{(k_{Si}-1)}}{D_{Si}} + \frac{m_{Mg}C_{Mg}(1-k_{Mg})(1-f_S)^{(k_{Mg}-1)}}{D_{Mg}}\right) . \tag{4.5.12}$$

Substituting the constants given in the nomenclature into the above equation, we obtain the following equation that can be used for Al-Si-Mg alloys having a composition of 6.94 wt % Si and 0.42 wt % Mg, respectively.

$$t_c = d_2^3(3.85C_{Si} + 1.90C_{Mg}) \times 10^{-6} \quad . \tag{4.5.13}$$

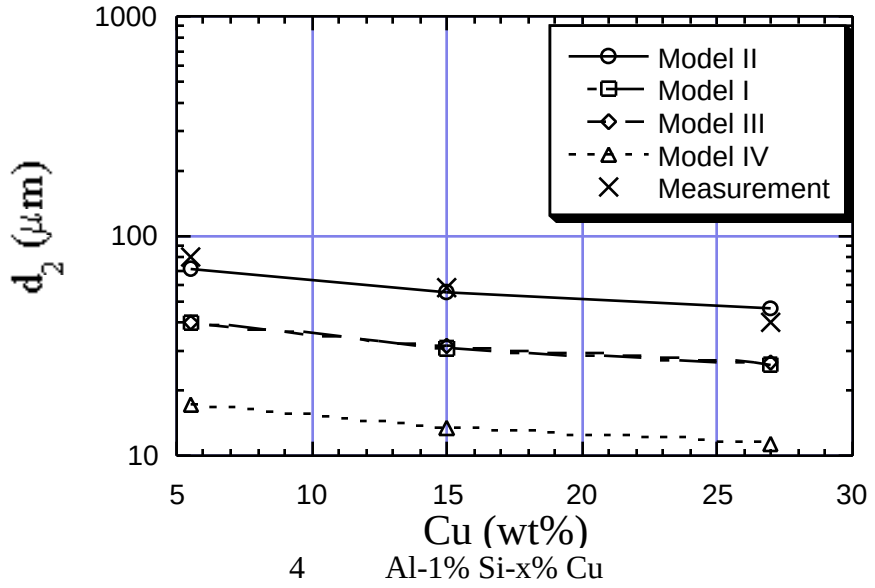

4 Al-1% Si-x% Cu

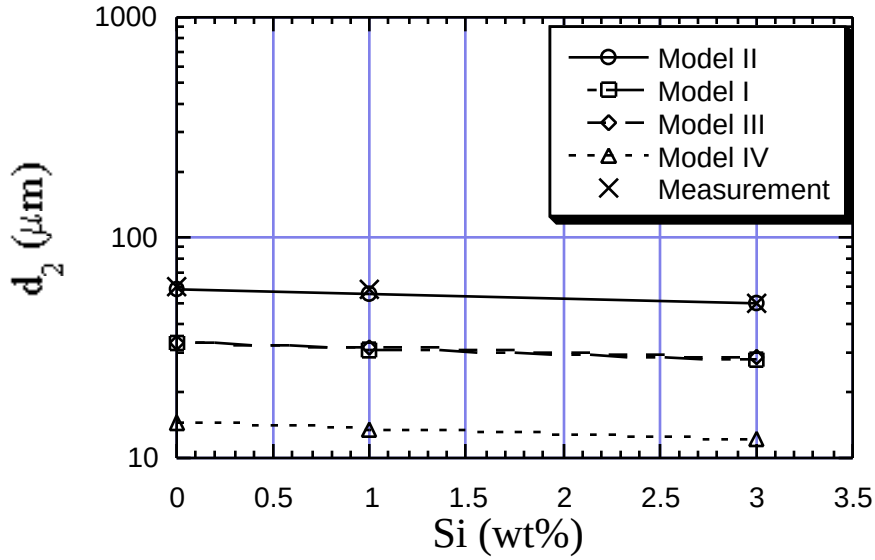

(*b*) Al-1.5% Cu-x% Si

Fig. 4.5.11. A comparison of theory with experiment for secondary dendrite arm spacings in Al-Cu-Si alloys.

That is

$$d_2^3 = \frac{10^6}{3.85C_{Si} + 1.90C_{Mg}} t_c \quad . \tag{4.5.14}$$

These equations can be used to calculate the secondary dendrite arm spacing as a function of the local solidification time and composition in A356 alloys. They can also be written in terms of the average cooling rate. Usually, the local solidification time can be related to the average cooling rate by $t_C=(T_L-T_S)/q$.

4.5.3 Dendrite Cell Spacing

The dendrite cell spacing, which is the average intercept of a random line intersecting dendrites, is a useful parameter for image analysis. This is because in many cases the primary dendrite size and the secondary dendrite arm spacing are not easily measured. As illustrated in Fig. 4.5.2, the basic microstructural feature for the aluminum-rich primary phase consists of randomly distributed secondary arms. The length of a secondary arm is approximately $d_1/2$ and the diameter is approximately d_2. Since an random line intersecting secondary arms is likely to produce an intercept length that falls between $d_1/2$ and d_C,, one should be able to estimate the dendrite cell spacing using

$$d_C = \frac{(d_1/2 + d_2)}{2} \quad . \tag{4.5.15}$$

4.5.4 Silicon Rod Length

Little information is available on the prediction of silicon rod length. Experimentally, it has been shown that the eutectic nucleates and grows on the primary aluminum phase (Bäckerud, Chai, and Tamminen, 1990). Figure 4.5.12 illustrates this growth morphology for an Al-11 wt % Si alloy. In the lower part of Fig. 4.5.12, we can see a primary aluminum dendrite surrounded by radiating silicon needles. A similar growth pattern may be expected for the eutectic silicon in A356 alloy, although it is less evident in a metallographic specimen due to the lower silicon content (7.0%) in the alloy. The reason the eutectic silicon nucleates on the primary aluminum phase is that silicon is rejected by the growing primary dendrites and is most enriched at the primary dendrite surface. Also, while the volume fraction of primary aluminum phase in an Al-11% Si alloy would be small, the volume fraction of primary dendrites in A356 alloy is about 52%, producing a coherent contiguous network. This allows us to construct a representative volume element around each primary aluminum dendrite that contains a distribution of phases that is representative of the overall microstructure. Such a representative volume construction is illustrated in Fig. 4.5.13. In Fig. 4.5.13, the black phase is the silicon phase, which branches by a twinning mechanism (Lu and Hellawell, 1987). The average length of silicon rods is defined by l. Knowing the volume fractions of the primary dendrite phase and the eutectic, the average length of the silicon rods can be related to the primary dendrite size based on simple geometric considerations.

In Fig. 4.5.13, the volume fraction of the primary aluminum phase is given by

$$1 - g_E = \frac{\pi(d_1/2 - l)^2}{\pi(d_1/2)^2} \quad . \tag{4.5.16}$$

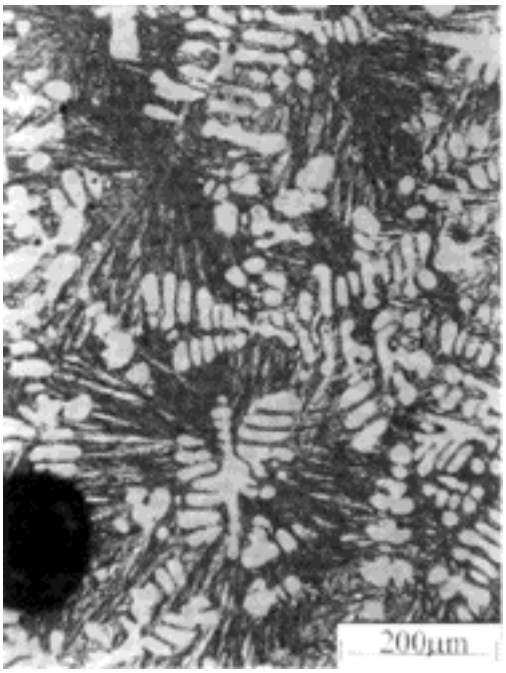

Fig. 4.5.12. Microstructure showing that the eutectic grows from a dendrite in an Al-11 wt % Si alloy (Bäckerud, Chai, and Tamminen, 1990).

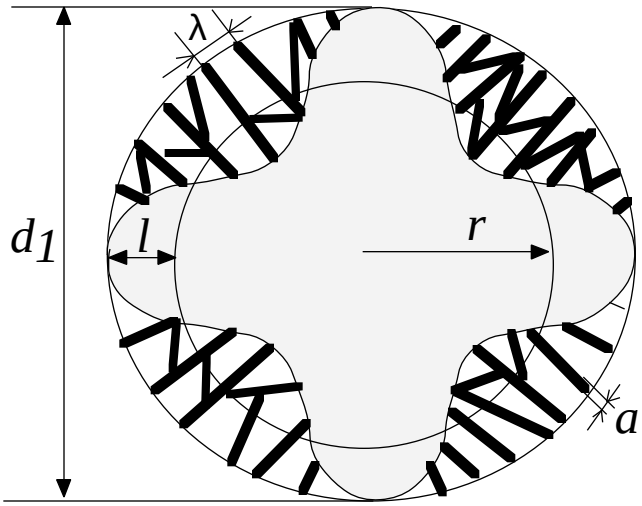

Fig. 4.5.13. Schematic diagram showing the relationship between the primary dendrite size and the average lenglth of the silicon phase.

Rearrangement of Eq. 4.5.16 yields

$$l = \frac{d_1}{2}(1 - \sqrt{1 - g_E}) \quad . \tag{4.5.17}$$

In Eq. 4.5.17, g_E can be calculated using thermodynamic software such as ThermoCalc^{TM} and d_1 is given by Eqs. 4.5.6 and 4.5.7. Thus, the average length of silicon rod is a function of g_E and d_1.

4.5.5 Silicon Rod/Particle Diameter

The microstructure observed in the transverse section perpendicular to the growth direction of the silicon phase is illustrated in Fig. 4.5.14, in which a is the silicon rod diameter and λ is the silicon rod spacing. Once again simple geometric considerations can be used to relate these two parameters resulting in the following equation:

$$g_{Si} = \frac{\pi a^2 / 4}{\pi \lambda^2 / 4} \quad , \tag{4.5.18}$$

where g_{Si} is the silicon volume fraction in the eutectic and can be calculated using ThermoCalc^{TM}. For A356, g_{Si} equals to 0.14. Rearrangement of Eq. 4.5.18 gives

$$a = \lambda \sqrt{g_{Si}} \quad . \tag{4.5.19}$$

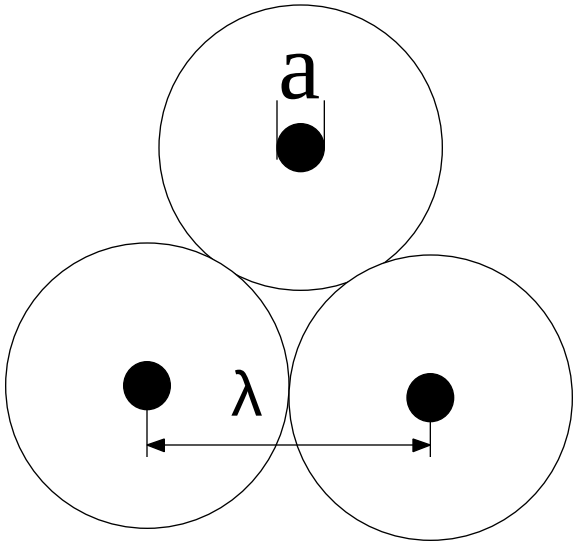

Fig. 4.5.14. Schematic diagram illustrating the relationship between the spacing and diameter of silicon.

Extensive studies have been carried out to determine the growth law for eutectics and to obtain the spacing, λ (Jackson and Hunt, 1966; Trivedi, Magnin, and Kurz, 1987; Kurz and Trivedi, 1991; Magnin and Trivedi, 1991; Sato and Sayama, 1974; Magnin and Kurz, 1987; Hogan and Song, 1987; Toloui and Hellawell, 1976). For a non-faceted interface, the most successful theory is that of (Jackson and Hunt, 1966) that proposes the following growth law correlating the eutectic spacing, λ, with the growth velocity of the solid, V_S:

$$\lambda^{b} V_S = c \quad , \tag{4.5.20}$$

where *b* and *c* are constants. Efforts have been made to extend the Jackson-Hunt model to treat non-faceted/faceted eutectic systems (Sato and Sayama, 1974; Magnin and Kurz, 1987) but several unrealistic assumptions have been made. Experimental approaches to validate the growth law for non-faceted systems have also been carried out and it has been found that the constants *b* and *c* vary with alloy and temperature gradient (Hogan and Song, 1987; Toloui and Hellawell; 1976). For modified Al-Si binary alloys, the growth law is in the form (Hogan and Song, 1987).

$$\lambda = 0.0311 V_S^{-0.446} \quad . \tag{4.5.21}$$

No tests of this growth law for A356 alloy are available in the literature. Based on experimental data generated (Gokhale, 1999) in connection with this program, the following form of the growth law is proposed for the silicon spacing:

$$\lambda = 0.16 V_S^{-0.446} \quad . \tag{4.5.22}$$

4.5.6 Validation of the Models in Plate Casting

The analytical equations given in Sections 4.5.2 through 4.5.5 were used in the post processing step of a commercial solidification package, ProCAST^{TM}, for the prediction of microstructural length scales in a plate casting. The predictions were then compared with independent experimental measurements (Gokhale, 1999) on plate castings of A356 alloy (7 wt % Si, 0.4 wt % Mg). The geometry of the plate casting is given in Fig. 4.5.15. Plate castings of dimensions 229 × 140 × 38 mm (9×5.5×1.5 in.) were cast in sand mold with cast iron chills on the top, bottom, and end of the plate. The sides of the plate were left unchilled. Measurements were taken along the vertical center plane of the casting. The length scales compared in this section are dendrite cell spacing, silicon length and silicon diameter.

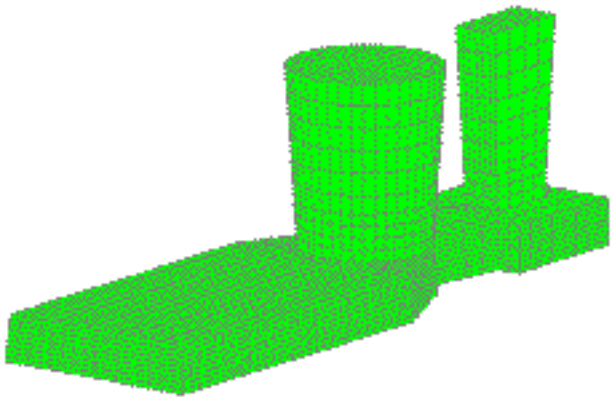

Fig. 4.5.15. The plate casting used for the validation of the microstructure models.

The comparison of predicted dendrite cell spacings with experimental measurements is shown in Fig. 4.5.16. The dendrite cell spacing was calculated using Eq. 4.5.15. Very good agreement between the prediction and the measurements is evident.

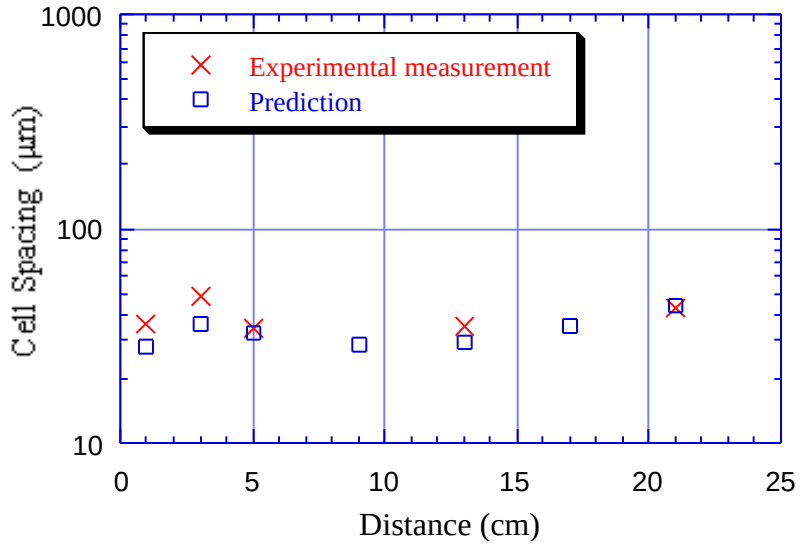

Fig. 4.5.16. Comparison of the model's predictions with experimental measurements of dendrite cell spacing for A356 alloy.

Figure 4.5.17 shows the comparison of the predicted silicon rod length and experimental measurements. Once again, the predictions fit well with experimental data. Considering that Eq. 4.5.17 is semi-quantitative in nature, the comparison shown Eq. 4.5.17 is better than expected.

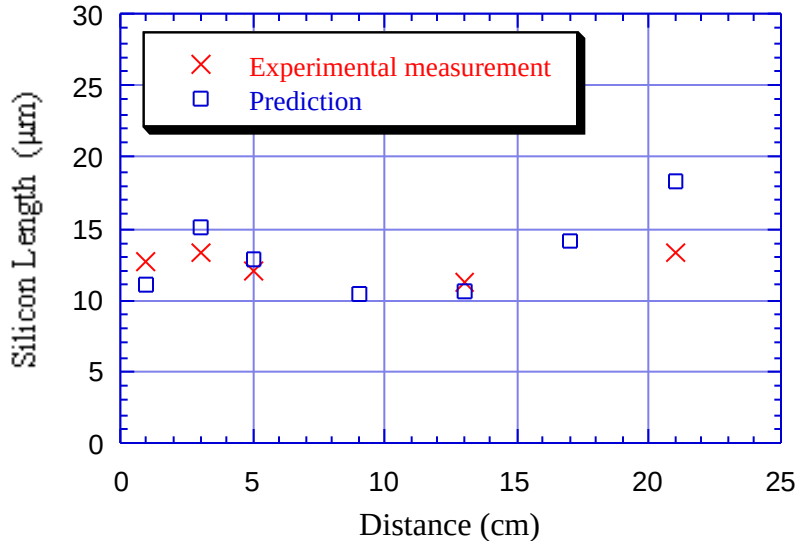

Fig. 4.5.17. Comparison of the model's predictions with experimental measurements of silicon rod length for A356 alloy.

Figure 4.5.18 shows a comparison of the predicted silicon rod diameter with data from experimental measurements. The use of the growth law in the form of Eq. 4.5.21 gives a silicon rod size a half an order of magnitude smaller than the measurements. A good fit with experimental data is obtained using the modified constant in Eq. 4.5.22. However, Eq. 4.5.22 must be considered to be strictly empirical. Clearly, fundamental research is needed to determine the growth law for eutectic formation with a faceted solid-liquid interface.

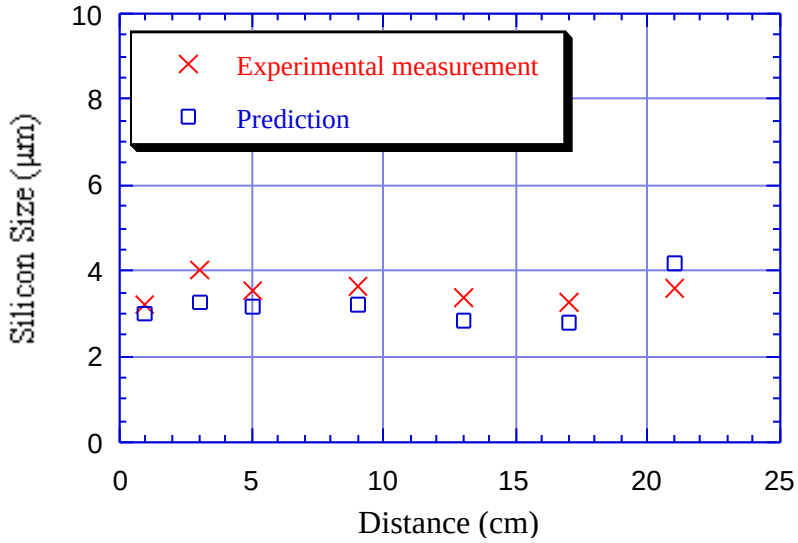

Fig. 4.5.18. Comparison of the predictions using a modified growth law constant with experi-mentally measured silicon rod diameter/size.

4.5.7 Conclusions

Models have been developed for the predictions of microstructural length scales in A356 aluminum alloys. These length scales are the primary dendrite spacing/size, secondary dendrite spacing, dendrite cell spacing and silicon rod length, size and spacing. Analytical equations have been derived that can be easily incorporated in the post processing step of commercial solidification codes. Comparison of predictions of microstructural length scales using these analytical equations with experimental measurements shows excellent agreement. Accordingly, the models developed in this program and documented in this report provide a convenient and viable approach for determining the microstructural length scales for A356 aluminum alloy casting needed in mechanical property and component life prediction models.

4.6 MODELING OF LOWER CONTROL ARM CASTING

The tilt-pour permanent mold rear lower control arm casting selected for demonstration of the tools developed in this program was modeled using commercial castings codes and the enhanced casting simulation capabilities developed in this project. The modeling of the lower control arm included mold filling, solidification, microporosity distribution, and microstructural length scale distribution. Two different configurations of the lower control arm casting were modeled, viz., the production component, and a modified version that was approximately 25% lighter. The mold filling simulations were accomplished using Flow-3D™. The microporosity and microstructure models developed in this program and implemented in the commercial casting code ProCAST™ were used to model microporosity and microstructural length scales. The finite element mesh used to model microporosity and microstructure was provided by EKK, Inc. Figure 4.6.1 shows the lower control arm casting.

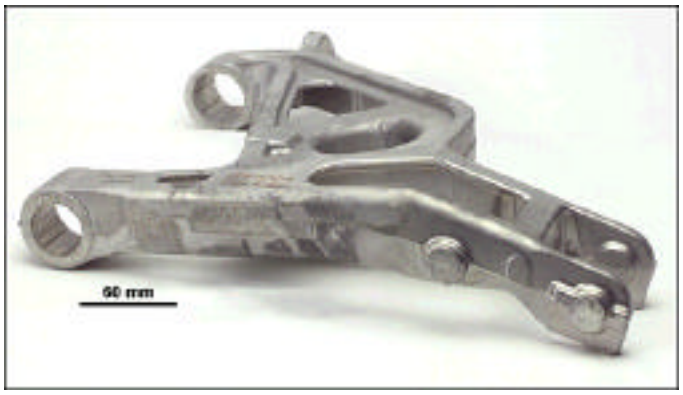

Fig. 4.6.1. Rear lower control arm casting used for demonstration of simulation capabilities developed in this program.

4.6.1 Process Parameters

Process parameters for the lower control arm castings were obtained from DaimlerChrysler, since the castings were poured at their casting laboratory. The casting procedure used by Chrysler followed the general guidelines used for permanent molds but was not identical to the parameters used in production runs. As per the information supplied by DaimlerChrysler, "the mold was coated with Stahl's DAG 632 coating with a second coat of graphite coating on the runners and pour cup. The mold was preheated using a propane burner to approximately 340˚C (650˚F). The air-cooling in the mold was turned off. Ten castings were poured using un-degassed metal to heat the mold. Then, the air-cooling lines were turned on and fifteen castings were poured using degassed metal. The metal temperature in the furnace was measured to be 754˚C (1390˚F). The metal temperature in the pour cup was measured to be 652˚C (1205˚F). The mold temperature during the first casting ranged from 400˚C (760˚F) to 440˚C (820˚F). The mold temperature during the last casting temp ranged from 450˚C (840˚F) to 470˚C (880˚F). A reduced pressure sample poured from the metal and was comparable to #1 on the Stahl chart. Actual hydrogen levels in either the melt or the casting were not measured. The ejection time was 4.5 min and the tilt time was 20 s. The total cycle time was 5 min."

4.6.2 Modeling of Mold Filling of Production Casting

The tilt-pour filling of the mold was accomplished using Flow-3D™. A regular grid comprising 470,400 elements was used for the simulation of the production component. The large grid resolution was needed in order to mesh the thin walls present in the casting. The die was not meshed since the size of the mesh for the casting alone approached the limits suggested by Flow3D for reasonable computing times and turn-around. Thus, while heat transfer during the filling was considered, a constant mold temperature was assumed. The alloy temperature in the pouring cup was assumed to be 750˚C, and the die temperature was held constant at 350˚C. The mold was tilted with a constant angular velocity of 0.05236 rad/s (or 3˚/s), corresponding to a total tilt time of 30 s. This tilt rate is somewhat slower than used by DaimlerChrysler, but corresponds to that used in production runs. The mold temperature used in the simulation represents a worst case condition, since it is equal to the mold preheat temperature at the start of the initial casting cycle, but is lower than that used for actual casting runs. It was decided to make the initial metal temperature in the pour cup equal to the metal temperature measured by DaimlerChrysler in the furnace rather than that in the pour cup, as heat would have been lost during the time taken for temperature measurement. The interface heat transfer coefficient between the casting and the die was assumed to be 0.02 cal/cm^2-˚C-s.

Figures 4.6.2 to 4.6.4 show filling patterns at 3, 5, and 8 s from the start of casting. As the mold tilts upward, the melt flows from the pouring cup down the gating system into the mold cavity. In Fig. 4.6.2, a snapshot of the filling pattern 3 s from the start of casting, the metal is just beginning to enter the mold cavity. Two important features are apparent in Fig. 4.6.2. First, while the metal enters the cavity at the bottom as intended, a small stream of metal enters toward the top of the cavity. Second, a break in the metal stream is apparent in the left runner. Both these features are undesirable, since both the secondary metal stream and the metal droplets in a broken metal stream are susceptible to premature freezing, or surface oxidation, or both. Even if frozen particles are later entrained in the primary metal stream, they may not remelt and may create internal interfaces that can serve as sites for crack nucleation when the component is loaded in service. Oxide films that are formed in the runner can be transported to other regions of the casting during filling. It is well known that oxide films can serve as sites for porosity and crack nucleation. Figures 4.6.3 and 4.6.4 also confirm the presence of a second stream that enters at the top of the cavity, as well as the break-up of the metal stream in the runner. In fact, Fig. 4.6.3 suggests that the metal streams break up in both the left and right runners.

The results of the filling simulation suggest that the gating system should be redesigned such that there is no breakup of the metal stream in the runner, and such that metal does not enter at the top of the cavity. Of the two undesirable features suggested by the filling profile, the breakup of the metal stream in the runner is likely to require more effort and careful optimization of the runner design and the tilt speed during casting. It is also more likely to reflect an actual drawback in the runner design. An examination of the tooling suggested that the secondary metal stream entering the top of the cavity may be an artifact in the simulation, due to the omission of a runner pad at the entrance to the gate at the top of the mold cavity. The runner pad would serve to block metal from entering the mold cavity from the top until late in the filling, when the cavity was almost full.

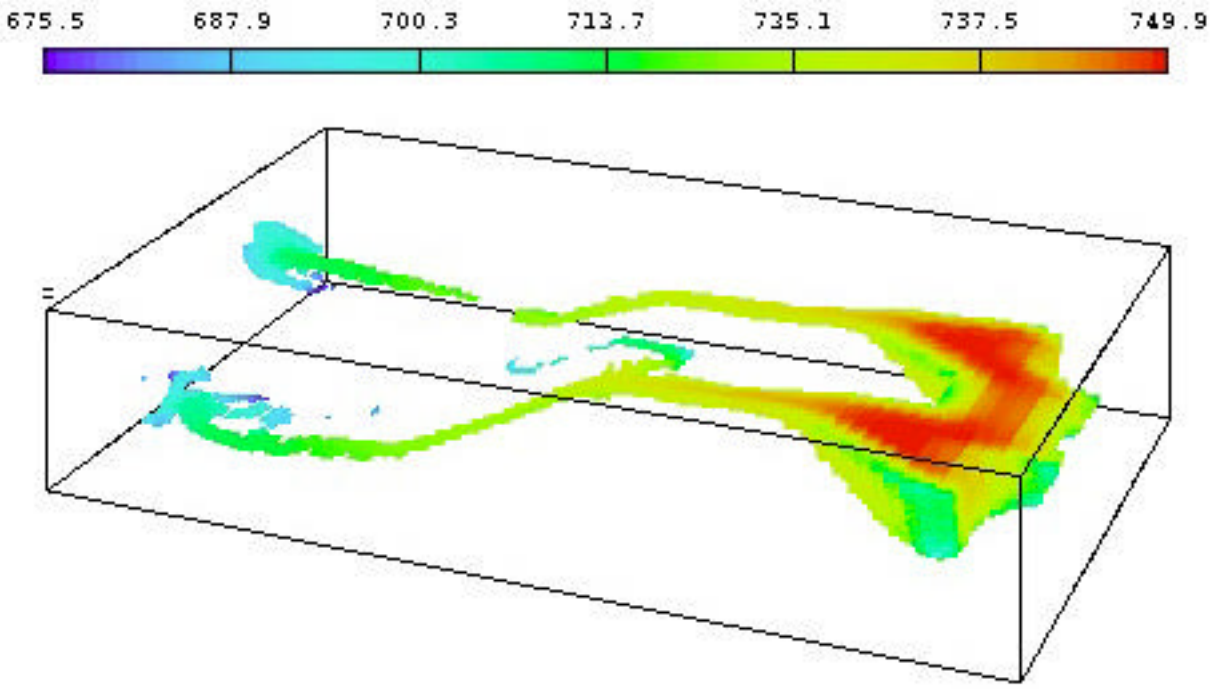

Fig. 4.6.2. Snapshot of mold filling simulation 3 seconds from the start of filling.

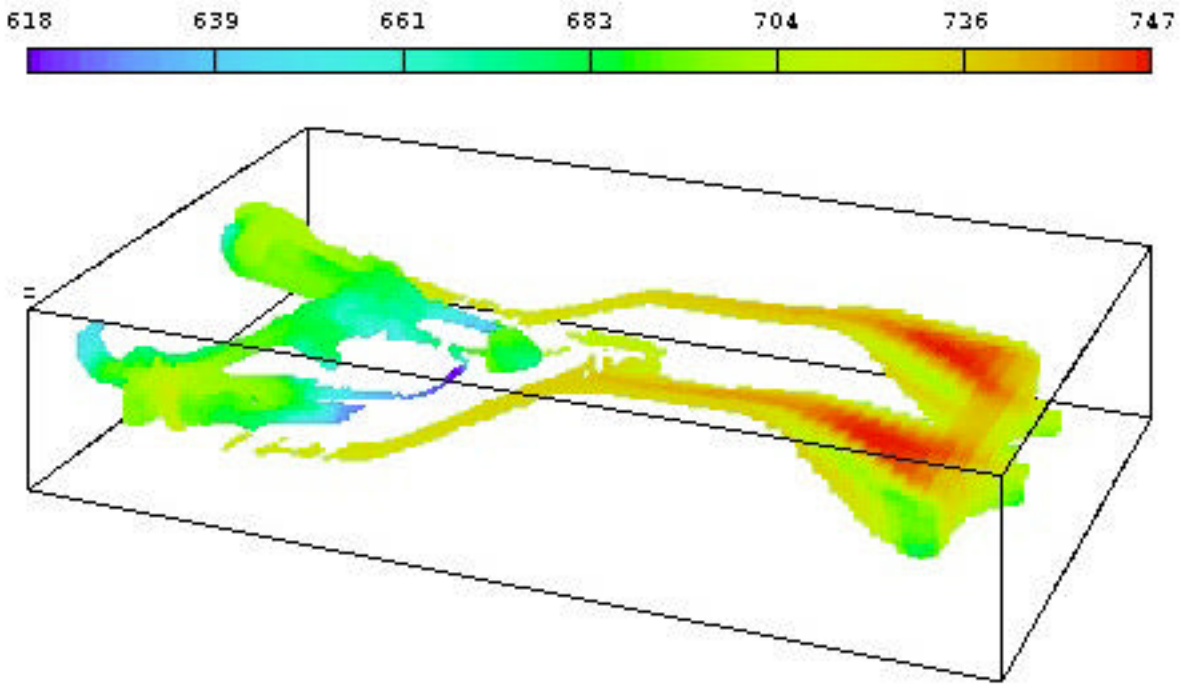

Fig. 4.6.3. Snapshot of mold filling simulation 5 seconds from the start of filling.

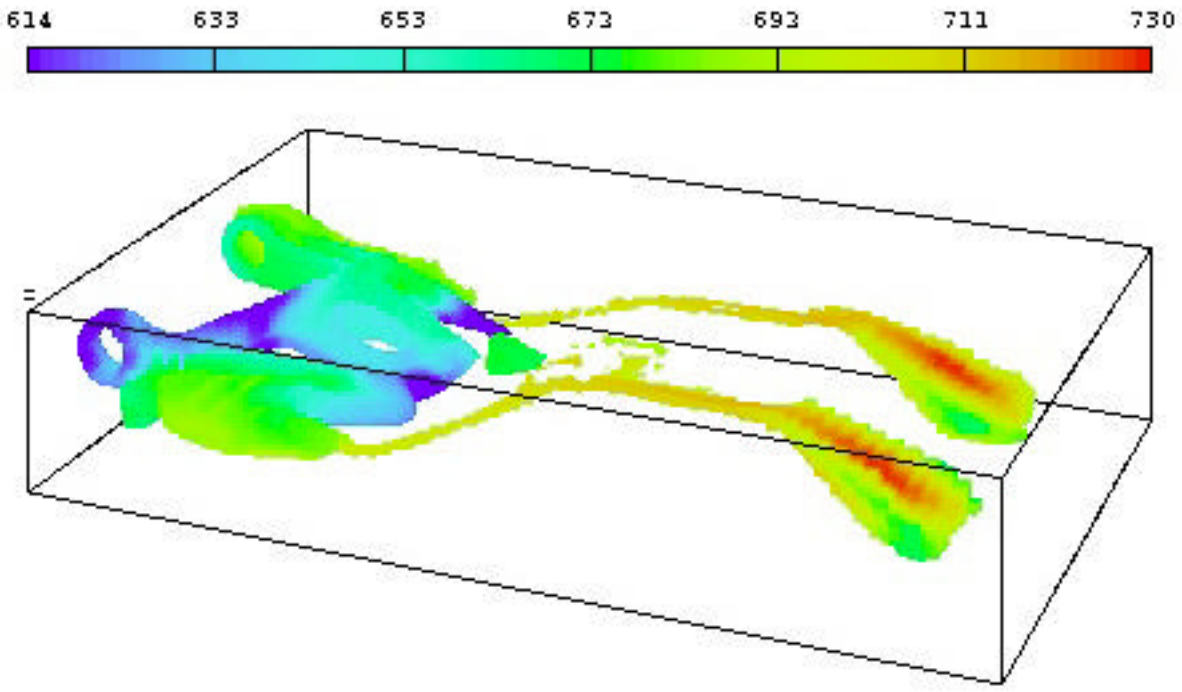

Fig. 4.6.4. Snapshot of mold filling simulation 7 seconds from the start of filling.

4.6.3 Modeling of Mold Filling of Modified Casting

Modeling of mold filling of the modified lower control arm casting was attempted using Flow3D™, but the effort was abandoned after several trials as the mesh size required for reasonable resolution of casting features approached two million elements. The thinner walls of the modified casting required a finer grid spacing for adequate resolution, and the size of the mesh was larger than that could be supported by the memory limitations of the workstation being used for this effort.

4.6.4 Porosity Model Implementation in ProCAST

The microporosity model was implemented in the commercial casting software ProCAST to allow the modeling of complex production castings, and to allow the model to be used by industry. As implemented in ProCAST, the ORNL porosity model is completely transparent to the user, and can be accessed in ProCAST version 3.2 by the specification of three parameters:
POROS= 3 -This activates the ORNL porosity model
PREF = 7 1.0 - This sets a reference pressure of 1 atm
CINIT = 0.112- This specifies the hydrogen level (in cc/100g)

The ProCAST implementation of the microporosity model was first validated on the same test plate castings used to validate the ORNL code. Next, the model was used to demonstrate the prediction of hot spots in castings. Figures 4.6.5 shows ProCAST results for a motor mount casting in which porosity was found at the center of the casting when no pressure was applied

during solidification. When the casting is squeezed during solidification, radiographic porosity is suppressed.

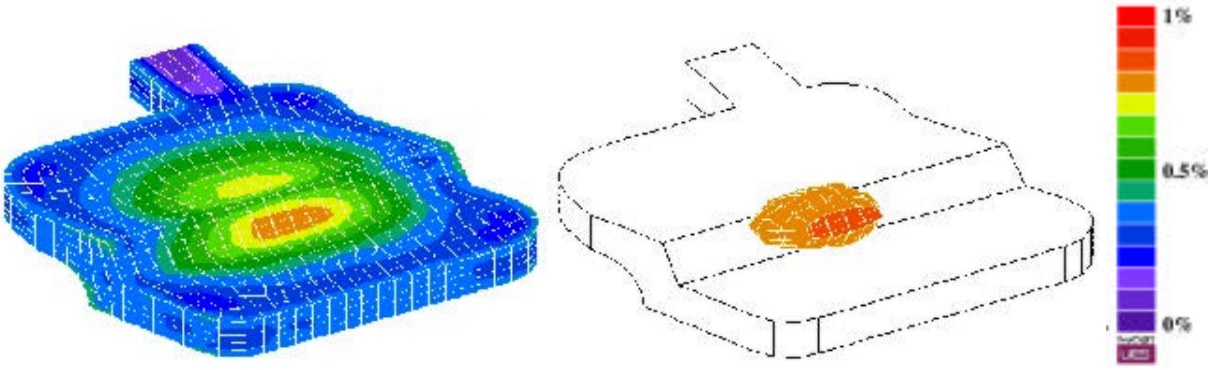

Fig. 4.6.5. Demonstration of hot spot prediction using the ProCAST implementation of the microporosity model

4.6.5 Modeling of Lower Control Arm Castings

The microporosity model developed in this program and implemented in the commercial casting code ProCAST™ was used to model microporosity distributions in the lower control arm casting. The finite element meshes of the lower control arm casting were provided by EKK, Inc.

The mesh for the production control arm consisted of 161,000 elements and 193,846 nodes, while the mesh for the modified control arm consisted of 203,949 elements and 210,471 nodes. Mostly hexahedral elements were used in the mesh, although some wedge elements were also used when necessary. Five material types were used to model the casting, runners and pouring cup, lower die, upper die, and the core. However, only two elements were used through the casting thickness to keep the mesh size to reasonable levels. The simulation of the tilt-pour process was accomplished in two steps. First, ten thermal-only simulations were run to establish the steady state temperature profile in the die. Comparisons of temperature maps of the die with results from die-face temperatures (provided by General Motors Corp.) made using an infra-red camera showed reasonable correlation. Next, a filling and solidification simulation was carried out to determine solidification conditions, microporosity levels, and microstructural length scales. The alloy temperature was assumed to be 750˚C, the initial die temperature was specified to be 200˚C, and the interface heat transfer coefficient between the alloy and the die was assumed to be 0.02 cal/cm^2-˚C-s. The mold was tilted with a constant angular velocity of 3˚/s, corresponding to a total tilt time of 30 s. The ejection time was 4.5 min and the total cycle time was 5 min. The hydrogen level in the alloy was assumed to be 0.112 cc/100 g (0.1 ppm).

Figure 4.6.6 illustrates the calculated porosity distribution in the production control arm, while Figure 4.6.7 illustrates the calculated porosity distribution in the modified (25% lighter) control arm. Figures 4.6.8 and 4.6.9 illustrate the calculated silicon particle length and silicon particle spacing in the production control arm. The results are in general agreement with the experimental measurements conducted at the Georgia Institute of Technology. However, more detailed comparisons will require a more rigorous attention to details such as the actual hydrogen

level in the alloy, the incorporation of air cooling in the mold in the simulation, and the use of at least three, and preferably five elements through the section thickness. This will more accurately capture the thermal conditions in the die and the interdendritic fluid flow in the mushy casting that is responsible for microporosity formation.

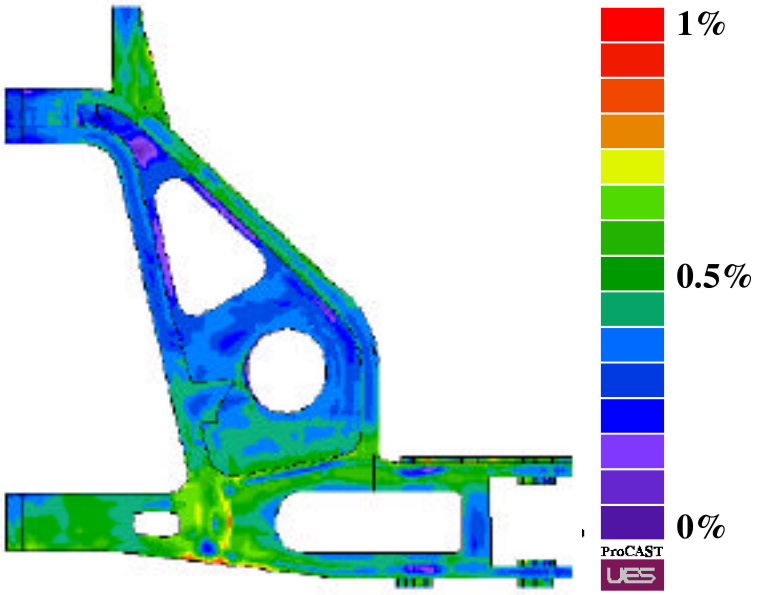

Fig. 4.6.6. Porosity distribution in the production control arm casting at the end of solidification calculated using the ProCAST implementation of the microporosity model.

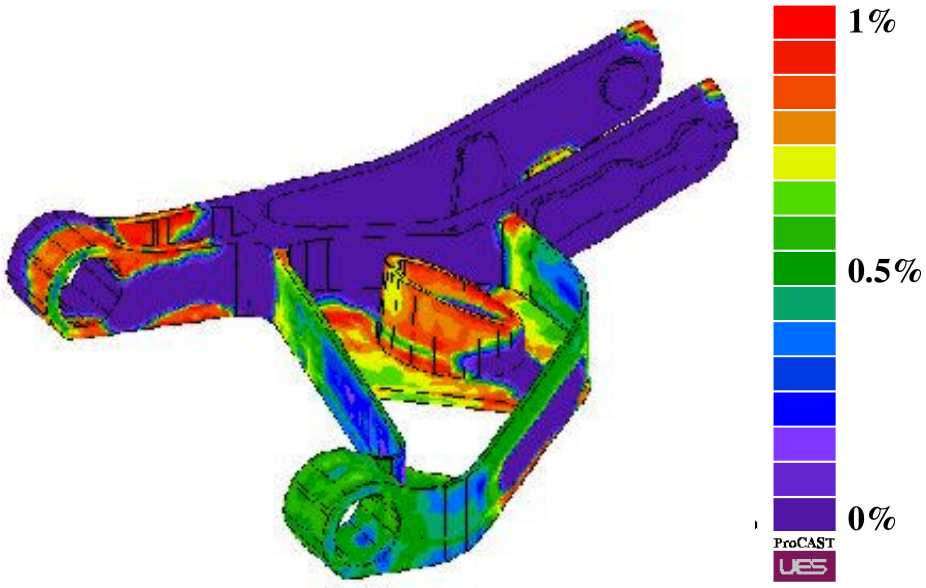

Fig. 4.6.7. Microporosity distribution in the modified control arm casting 75 seconds from the start of casting, calculated using the ProCAST implementation of the microporosity model.

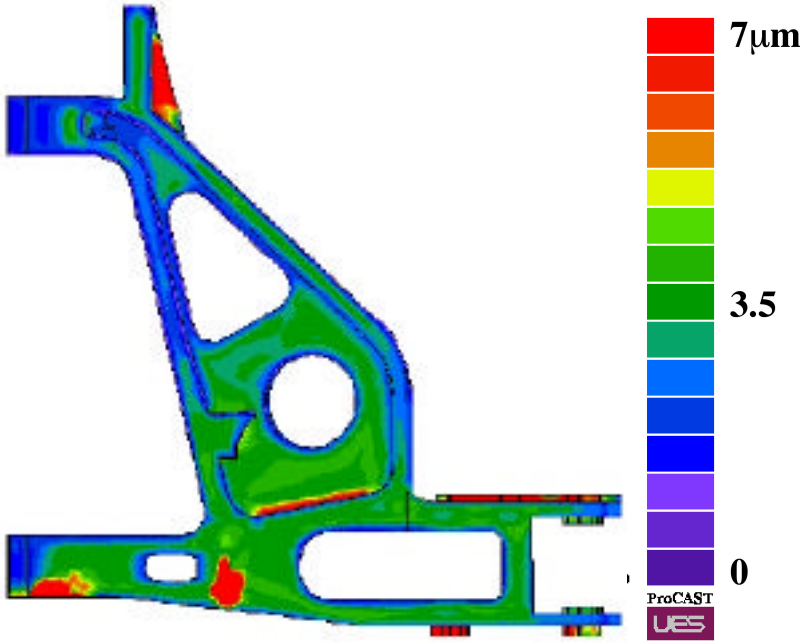

Fig. 4.6.8. Silicon particle length distribution in the production control arm calculated using ProCAST.

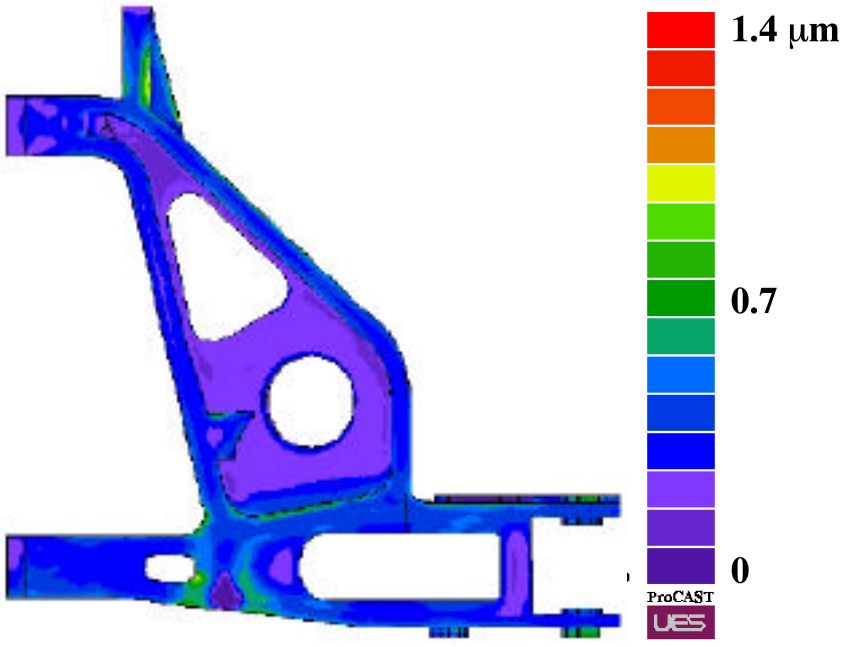

Fig. 4.6.9. Silicon particle spacing distribution in the production control arm calculated using ProCAST.

4.7 References

Anyalebechi, P. N., "Analysis of the Effects of Alloying Elements on Hydrogen Solubility in Liquid Aluminum Alloys," Scripta Metall. et Mater., vol. 33, pp 1209-1216 (1995)

Apelian, D., Flemings, M. C., and Mehrabian, R., "Specific Permeability of Partially Solidified Dendritic Networks of Al-Si Alloys," Metall. Trans. B, vol 5, pp 2533-2537 (1974)

Arnberg, L., Backerud, L., and Chai, G., "Solidification Characteristics of Aluminum Alloys," Dendrite Coherency, vol 3, AFS, 1996

Bäckerud, L., Chai, G., and Tamminen, J., Solidification Characteristics of Aluminum Alloys, Vol.2: Foundry Alloys, AFS/SKANALUMINUM (1990)

Barkhudarov, M., Hou, H., Ortega, J., Beech, J., Chin, S. B., and Kirkwood, D. H., "Experimental Validation and Development of FLOW-3D for Casting Problems," Modeling of Casting, Welding, and Advanced Solidification Processes VI, p 421, TMS-AIME, Warrendale, PA (1993)

Beckermann, C. and Viskanta, R., "Mathematical Modeling of Transport Phenomena during Alloy Solidification," Applied Mechanics Reviews, vol 46, pp 1-27 (1993)

Bennon, W. D. and Incropera, F. P., "A Continuum Model for Momentum, Heat and Species Transport in Binary Solid-Liquid Phase Change Systems,I. Model Formulation," Int. J. Heat Mass Transfer, vol 30, pp 2161-2170 (1987)

Bishop, H. F. and Pellini W. S., "The Contribution of Riser and Chill Edge Effects to Soundness of Cast Steel Plates,"Trans AFS, vol 58, pp 185-87 (1950)

Carman, P. C., "Fluid Flow Through Granular Beds," Trans. Inst. Chem. Eng. (London), vol 15, pp 150-56 (1937)

Chalmers, B., Principles of Solidification, p 186, John Wiley, London (1964)

Chang, S. and Stefanescu, D.M., "A Model for Inverse Segregation: the Case of Directionally Solidified Al-Cu Alloys," Acta Mater., vol 44(6), pp 2227-2235 (1996)

Chen, K. H. and Kattamis, T. Z., "Role of Dendrite Coarsening and Coalescence in the Establishment of Cast Microstructure," Z. Metallkd., vol. 61, pp. 475-79 (1970)

Chiou, I. J. and Tsai, H. L., "," AFS Trans., vol 98, pp 823-830 (1990)

Combeau, H., Bourg, A., Charbonnier, J., Langlois, S., Lesoult, G., Rigaut, C., and Sztur, C., "Modelling of Microporosity Formation in Aluminium Alloys Castings," Modeling of Casting, Welding, and Advanced Solidification Processes VII , p 67, TMS-AIME, Warrendale, PA, (1995)

Dighe, M. D., Jiang, X. G., Tewari, A., Rahardjo, A. S. B., and Gokhale, A. M., "Quantitative Microstructural Analysis of Micro-Porosity in Cast A356 Aluminum Alloy," presented at AFS Meeting, Atlanta, GA, 1997

Fang, Q. T. and Granger, D. A., "Porosity Formation in Modified and Unmodified A356 Alloy Castings," Trans AFS, vol 97, pp 989-1000 (1989)

Fredriksson, H. and Svensson, I., Met. Trans. vol 7B, pp 599-606 (1976)

Ganesan, S. and Poirier, D. R., "Densities of Aluminum-Rich Aluminum-Copper Alloys During Solidification," Metall. Trans. A, vol 18A, pp 721-723 (1987)

Ganesan, S., Speiser, R., and Poirier, D. R., "Viscosities of Aluminum-Rich Al-Cu Liquid Alloys," Metall. Trans. B, vol 18B, pp 421-424 (1987)

Ghosh, P. K. and Ray, S., "Influence of Process Parameters on the Porosity Content in Al(Mg)-Al2O3 Cast Particulate Composite Produced by Vortex Method," Trans. AFS, vol 96, pp 775-82 (1988)

Gokhale, A. M., unpublished report (1999).

Han, Q., Hu, H. and Zhong, X., "Models for The Isothermal Coarsening of Secondary Dendrite Arms in Multicomponent Alloys," Metall. Mater. Trans., vol. 28B, pp. 1185-87 (1997)

Han, Q. and Hunt, J. D., "Numerical Modelling of The Growth of a Cellular/Dendritic Array in Multi-Component Alloys," Mater. Sci. Eng., vol. A238, pp.192-95 (1997)

Han, Q. and Viswanathan, S., "Pore Migration," unpublished report, 1999

Hogan, L. M. and Song, H., "Interparticle Spacings and Undercoolings in Al-Si Eutectic Microstructures," Metall. Trans., vol. 18A, pp. 707-13 (1987)

Huang, W., Geng, X., and Zhou, Y., "Primary Spacing Selection of Constrained Dendritic Growth," J. Cryst. Growth, vol. 134, pp. 105-115 (1993)

Hunt, J. D., "A Numerical Analysis of Dendritic and Cellular Growth of A Pure Material Investigating the Transition from Array to Isolated Growth," Acta Metall., vol. 39, pp. 2117-33 (1991)

Hunt, J. D. and Lu, S. Z., "Numerical Modeling of Cellular Dendritic Array Growth: Spacing and Structure Predictions," Metall. Trans, vol. 27A, pp. 611-23 (1996)

Iwahori, H., Yonekura, K., Yamamoto, Y., and Nakamura, M., Trans. AFS., vol 98, pp 163-73 (1990)

Jackson, K. A. and Hunt, J. D., “Lamellar and Rod Eutectic Growth,” Trans. Am. Inst. Min. Engrs, vol. 236, pp. 1129-42 (1966)

Kattamis, T. Z., Coughlin, J. C., and Flemings, M. C., “Influence of Coarsening on Dendrite Arm Spacing of Aluminum-Copper Alloys,” Trans. AIME, vol. 239, pp. 1504-11 (1967)

Kaviany, M., Principles of Heat Transfer in Porous Media, Spinger-Verlag, New York, NY (1991)

Krane, M. J. M. and Incropera, F. P., “Analysis of the Effect of Shrinkage on Macrosegregation in Alloy Solidification,” Metall. and Mater. Trans., vol 26A, pp 2329-2339 (1995)

Kubo, K. and Pehlke, R. D., “Mathematical Modeling of Porosity Formation in Solidification,,” Metall. Trans. B, vol 16B, pp 359-66 (June 1985)

Kurz, W. and Fisher, D. J., Fundamentals of Solidification, 3rd ed.,, p. 294, Trans Tech Publications, Aedermannsdorf (1989)

Kurz, W. and Trivedi, R., “Eutectic Growth under Rapid Solidification Conditions,” Metall. Trans., vol. 22A, pp. 3051-3057 (1991)

Lee, D. P., D. Phil. Thesis, Dept of Materials, Univ. of Oxford, 1994

Lee Y. W., Chang E., and Chieu, C. F., “Modeling of Feeding Behavior of Solidifying Al-7Si-0.3Mg Alloy Plate Casting,” Metall. Trans. B, vol 21B, pp 715-22 (1990)

Lu, S. Z. and Hellawell, A., “The Mechanism of Silicon Modification in Aluminum-Silicon Alloys – Impurity Induced Twinning,” Metall. Trans., vol. 18A, pp. 1721-1733 (1987)

Lu, S. Z. and Hunt, J. D., “A Numerical Analysis of Dendritic and Cellular Array Growth - The Spacing Adjustment Mechanisms,” J. Cryst. Growth, vol. 123, pp. 17-34 (1992)

Lu, S. Z., Hunt, J. D., Gilgien, P., and Kurz, W., “Cellular and Dendritic Growth in Rapidly Solidified Al-Fe and Al-Cu Alloys,” Acta Metall. Mater., vol. 42, No. 5, pp. 1653-60 (1994)

Magnin, P. and Kurz, W., “An Analytical Model of Irregular Eutectic Growth and Its Application to Fe-C,” Acta. Metall., 35, pp. 1119-1128 (1987)

Magnin, P. and Trivedi, R., “Eutectic Growth - A Modification of the Jackson and Hunt Theory,” Acta. Metall. Mater., vol. 39, pp. 453-467 (1991)

McCartney, D. G. and Hunt, J. D., “Measurements of Cell and Primary Dendrite Arm Spacings in Directionally Solidified Aluminum Alloys,” Acta. Metall., vol. 29, pp. 1851-63 (1981)

Metals Handbook Desk Edition, Boyer, H. E. and Gall, T. L., eds., p 35·17, American Society for Metals, Metals Park, OH (1985)

Mori, N., Ogi, K., and Matsuda, K., “The Secondary Arm Spacing of Dendrite in Al-Cu Based Alloys,” J. Jpn Inst. Met., vol. 40, pp. 406-11 (1976)

Murakami, K. and Okamoto, T., “Fluid Flow in the Mushy Zone Composed of Granular Grains,” Acta Metall., vol 32 (10), pp 1741-1744 (1984)

Nasser-Rafi, R., Deshmukh, R., and Poirier, D. R., “Flow of Interdendritic Liquid and Permeability in Pb-20 wt. pct. Sn Alloys,” Metall. Trans. A, vol 16A, pp 2263-2271 (1985)

Niyama E., Uchida, T., Morikawa, M., and Saito, S., “Predicting Shrinkage in Large Steel Castings From Temperature Gradient Calculation,” AFS Int. Cast Metals J., vol 6, pp 16-22 (June 1981)

Ocansey, P., Bhat, M. S., Poirier, D. R., and Finn, T. L., “Permeability For Liquid Flow in the Mushy Zones of Equiaxed Castings,” Light Metals 1994, Mannweiler, U., ed., pp 807-812, The Minerals, Metals, and Materials Society, Warrendale, PA (1994)

Opie, WR, and Grant, NJ., “Hydrogen Solubility in Aluminum and Some Aluminum Alloys,” Trans. AIME, Vol. 188, pp. 1237-1241.

Paradies, C. J., Arnberg, L., Thevik, H. J., and Mo, A., “Permeabilities For Interdendritic Melt Flow Through Equiaxed Aluminum Castings,” Modeling of Casting, Welding and Advanced Solidification Processes VII, M. Cross and J. Campbell, eds., pp 609-616, The Minerals, Metals, and Materials Society, Warrendale, PA (1995)

Patankar, S. V., Numerical Heat Transfer and Fluid Flow, Hemisphere, New York, 1982

Piwonka, T. S. and Flemings, M. C., “Pore Formation in Solidification,” Trans. AIME, vol 236, pp 1157-1165 (1966)

Poirier, D. R., Yeum, K., and Maples, A. L., “A Thermodynamic Prediction for Microporosity Formation in Aluminum-Rich Al-Cu Alloys,” Metall. Trans. A, vol 18A, pp 1979-87 (1987)

Poirier, D. R., “Permeability For Flow of Interdendritic Liquid in Columnar-Dendritic Alloys,” Metall. Trans. B, vol 18B, pp 245-255 (1987)

Poirier, D. R. and Ganesan, S., “Permeability for Flow of Interdendritic Liquid in Equiaxial Structures,” Matls. Sci. Engr. A, vol A157, pp 113-123 (1992)

Poirier, D. R. and Ocansey, P., “Permeability for Flow of Liquid Through Equiaxial Mushy Zones,” Matls. Sci. Engr. A, vol 171A, pp 231-240 (1993)

Prescott, P. J., Incropera, F. P., and Bennon, W. D., “Modeling of Dendritic Solidification Systems: Reassessment of the Continuum Momentum Equation,” Int. J. Heat Mass Transfer, vol 34(9), pp 2351-2359 (1991)

Reddy, A.V. and Beckermann, C., "Modeling of Macrosegregation Due to Thermosolutal Convection and Contraction-Driven Flow in Direct Chill Continuous Casting of and Al-Cu Round Ingot," Metall. and Mater. Trans., vol 28, pp 479-489 (1997)

Reddy, A. V., Kothe, D. B., Beckermann, C., Ferrell, R. C., and Lam, K. L., Proc. Fourth Int. Conf. on Solidification Processing , The Univ. of Sheffield, U.K., (1997)

Reeves, J. J. and Kattamis, T. Z., "A Model for Isothrmal Dendritic Coarsening," Scripta Metall., vol. 5, pp.223-29 (1971)

Rousset, P., Rappaz, M., and Hannart, B., "Modeling of Inverse Segregation and Porosity Formation in Directionally Soliddified Aluminum Alloys," Metall. and Mater. Trans A, vol 26A, pp 2349-58 (Sep 1995)

Sato, T. and Sayama, Y., "Completely and Partially Cooperative Growth of Eutectics," J. Crystal Growth, vol. 22, pp. 259-71 (1974)

Shahani, H., Scand. J. Metall., vol 14(6), pp 306-12 (1985)

Shivkumar, S., Apelian, D., and Zou, J., "Modeling of Microstructure Evolution and Microporosity Formation in Cast Aluminum Alloys," Trans. AFS, vol 98, pp 897-904 (1990)

Sigworth, G. K. and Wang, C., Metall. Trans. B, vol 24B, pp 365-77 (1993)

Streat, N. and Weinberg, F., "Interdendritic Fluid Flow in a Lead-Tin Alloy," Metall. Trans. B, vol 7B, pp 417-423 (1976)

Suri, V. K. and Paul, A. J., "Modeling and Prediction of Micro/Macro-Scale Defects in Casting," Trans AFS, vol 101, pp 949-54 (1993)

Tiwari, S. N. and Beech, J., Met. Sci., pp 356-362 (Aug 1978)
Toloui, B. and Hellawell, A., "Phase Separation and Undercooling in Al-Si Eutectic Alloy - Influence of Freezing Rate and Temperature Gradient," Acta Metall., vol. 24, pp. 565-73 (1976)

Trivedi, R., Magnin, P., and Kurz, W., "Theory of Eutectic Growth under Rapid Solidification Conditions," Acta. Metall., vol. 35, pp. 971-980 (1987)

Viswanathan S., Sikka, V. K., and Brody, H. D., ","JOM, pp 37-40 (Sep. 1992)

Voller, V. R. and Prakash, C., "A Fixed Grid Numerical Modeling Methodology for Convection-Diffusion Mushy Region Phase-Change Problems," Int. J. Heat Mass Transfer, vol 30, pp 1709-19 (1987)

Walther W. D., Adams, C. M., and H. F. Taylor, Trans AFS, vol 64, pp 658-64 (1956)

Wan, X., Han, Q., and Hunt, J. D., “Different Growth Regimes During Directional Dendritic Growth,” Acta Mater., vol. 45, pp. 3975-79(1997)

Wilcox, W. R. and Kuo, V. H. S., “Gas Buble Nucleation during Crystallization”, J. Crystal Growth, vol 19, pp 221-228 (1973)

Wilt, P. M., J. Colloid and Interface Sci., vol 112(2), pp 530-538 (1986)

Zou, J. and Doherty, R., “Micro-Macroscopic Modeling of Solidification and Interdendritic Fluid Flow in DC Cast Al-4.5Cu-1.5Mg Ingots,” Modeling of Casting, Welding, and Advanced Solidification Processes VI, p 193, TMS-AIME, Warrendale, PA (1993).

5.0 Report of Inventions

No inventions were made or reported regarding this CRADA. However, the models developed in this program were shared with CRADA partners and implemented in the commercial casting software ProCAST.

6.0 Commercialization Possibilities

The technologies developed in this CRADA are well suited for application to commercial casting production, as evidence by the fact that the models were implemented in the commercial casting software ProCAST. It is expected that the models developed in this program will significantly enhance the design of structural safety-critical aluminum alloy castings.

7.0 Plans for Future Colloraborations

Based on the success of this CRADA, a similar CRADA on magnesium alloy castings is being developed with the same partners.

8.0 Conclusions

This CRADA was extremely successful and substantially met all of the objectives in the statement of work. Specific results and conclusions for various subtasks in the CRADA are outlined in Chapter 4.

Acknowledgments

This work was the result of the collaborative efforts of the following persons:

Ralph Dinwiddie - Thermophysical Properties
Andy Duncan - Permeability Measurements
Qingyou Han - Microstructure Models
Ed Hatfield – Melting and Casting
Wally Porter - Thermophysical Properties
Jackie Mayotte - Metallography
Adrian Sabau – Microporosity Model
Srinath Viswanathan – Principal Investigator

This work was supported through a Cooperative Research and Development Agreement with the United States Automotive Materials Partnership, and sponsored by the U.S. Department of Energy, Assistant Secretary for Energy Efficiency and Renewable Energy, Office of Transportation Technologies, Lightweight Vehicle Materials Program, under contract DE-AC05-

00OR22725 with Oak Ridge National Laboratory, managed by UT-Battelle, LLC. This research was supported in part by appointments to the Oak Ridge National Laboratory Postdoctoral Research Associates Program, administered jointly by the Oak Ridge Institute for Science and Education and Oak Ridge National Laboratory. The authors would like to thank the many participants in this project for their time and effort and stimulating and useful input. In particular, the authors would like to thank Dick Osborne and Don Penrod for their herculean efforts to keep the project on track. The authors would also like to thank Millie Atchley and Glenda Carter for their assistance in preparing the final report.

INTERNAL DISTRIBUTION

1. E. E. Bloom
2. R. B. Dinwiddie
3. Q. Han
4. W. D. Porter
5. T. M. Rosseel
6. A. S. Sabau
7. V. K. Sikka
8. P. S. Sklad
9-11. S. Viswanathan
12. P. J. Wenzel
13. K. M. Wilson
14. Office of Technical Information and Classification, 4500N, 6254

EXTERNAL DISTRIBUTION

15. DOE/ORO, 4500N, 6269
16. R. J. Osborne, General Motors Corporation, 30300 Mound Road, Warren, MI 38090-9040.
17. D. E. Penrod, Manufacturing Services and Development, Inc., 4665 Arlington Drive, Cape Haze, FL 33946.
18. R. Wrobleski, USAMP, 1000 Town Center, Suite 300, Southfield, MI 48075.
19. DOE/Work for Others, MS G209